# Advances in Pedestal Substrate Integrated Waveguide Filters

by

Leanne Johnson

*Dissertation presented in fulfilment of the requirements for the degree of Doctor of Philosophy in Engineering in Electronic Engineering in the Faculty of Engineering at Stellenbosch University and Université de Bretagne Occidentale*

| | |
|---|---|
| Supervisor: | Prof. P Meyer |
| Co-supervisor: | Prof. B Potelon, |
| | Dr. E Meyer |

April 2022

# Declaration

By submitting this dissertation electronically, I declare that the entirety of the work contained therein is my own, original work, that I am the sole author thereof (save to the extent explicitly otherwise stated), that reproduction and publication thereof by Stellenbosch University and Université de Bretagne Occidentale will not infringe any third party rights and that I have not previously in its entirety or in part submitted it for obtaining any qualification.

Date: . . . . . . . . . April 2022 . . . . . . . . . .

i

# Acknowledgements

I would like to dedicate this part of my thesis to thanking the long list of people who made it possible.

- This thesis would not have been made a reality if it was not for the inspiration and love of the subject brought upon me by Prof. P Meyer. I will forever be grateful for the influence Prof. P Meyer played in my career as well as my general being. Thank you from the bottom of my heart for all the support, advice and encouragement.

- Without the wonderful working environment in Brest, France created by Prof. B Potelon a huge portion of this thesis would not have been concluded. I thank you for the opportunity and life changing experience you made possible for me.

- Without the support and profound knowledge of Dr. E Meyer the success of this thesis would not have been possible. Thank you for your encouragement and support.

- The endurance on this long and often difficult journey was only made possible by the constant encouragement of my mother, Vanessa Johnson. Since the beginning of this journey you have supported me, believed in me and accompanied me all the way. You shared in all my laughter and my tears. I love you dearly.

- From behind the scenes, Henry Peter Johnson (Senior) my father was my rock. Nothing could compare to the opportunities you have always made possible for me. I thank you and love you so much.

- My dear brother, Henry Peter Johnson (Junior), was the calmness that often carried me through tough times. Thank you for all your advice. I love you too

- I would like to acknowledge and thank the hard work of Hassan Bouazzaoui in Brest, France for the technical support and manufacturing of the partially air filled pedestal resonator and filter.

- Wessel Croukamp and Wynand van Eeden for the manufacturing and construction of various prototypes and for the assistance with the creation of various dxf files.

- Anneke Bester and Bea Wessels for the help with the measurements.

- To all my family and friends, thank you for your support and encouragement. A special word of thanks to Theresa de Vries, my aunt for your companionship on this journey.

# Abstract

This dissertation presents a set of advances to the recently proposed Pedestal Substrate Integrated Waveguide (SIW) structure as a solution to various problem areas in the field of microwave filters. The structure consists of an evanescent-mode SIW cavity that is loaded with a square pedestal connected to the ground with a metal post. This structure is firstly investigated and compared to other common microwave resonators. It is then utilized in 3 different ways.

The work includes the design of a coupled resonator filter with both positive and negative cross-coupling. Electric coupling is obtained with an I-shaped line between pedestal tops, while positive coupling is obtained in the traditional manner with inductive irises. Both types of couplings offer large ranges of coupling values and are easily implemented in this structure. The proposed structure can also introduce mixed coupling. A proof-of-concept sixth order cross-coupled bandpass filter, with a 5 % bandwidth at 5 GHz, and both real and imaginary axis transmission zeros, is designed and measured.

Secondly, the dissertation presents a novel partially air filled pedestal resonator. The pedestal SIW topology is adapted to create partially air filled pedestal SIW resonators to reduce losses and increase Q factors while maintaining small sizes. A comparison of three different types of pedestal resonators is done between a totally filled pedestal SIW resonator, a partially air-filled pedestal resonator and an empty pedestal resonator, showing the increase in Q factor for the same size. Then the use of micro-machining to create these novel resonators is illustrated and explained. A resonator and second order filter prototypes are manufactured, using the manufacturing process explained, and tested. It was shown that the Q factor can be increased from 186 for a fully filled dielectric resonator to 285 for a partially air filled resonator. This shows a 34.7 % increase.

The last application of the pedestal resonator is in the use of tunable structures. The pedestal resonator is shown to be made easily tunable by the addition of PIN diodes to the pedestal post, seperated with an annular ring. Four separate stages of frequency are obtained in this manner. Two resonators and one third order filter are designed, manufactured and tested. Good frequency tunability is obtained in simulation and measurement, but high losses were observed in the measured prototypes.

# Uittreksel

Hierdie verhandeling bied 'n aantal uitbreidings ann tot die onlangse voorgestelde voet-stuk oppervlak geïntegreerde golfleier struktuur, as 'n oplossing vir verskeie probleemareas op die gebied van mikrogolffilters. Die struktuur bestaan uit 'n onder afsny holte wat ge-vul is met 'n vierkantige voetstuk, gekonnekteer aan die grond met metaal. Eerstens is die struktuur ondersoek en vergelyk met ander algemene mikrogolfresoneerders. Daarna is dit op 3 verskillende maniere toegepas.

Hierdie werk sluit die ontwerp van 'n gekoppelde resoneerder filter in met beide positiewe en negatiewe kruis-koppeling. Elektriese koppeling is bereik met 'n I-vormige lyn tussen die voetstuk toppe, terwyl positiewe koppeling op die tradisionele manier van induktiewe openinge bereik is. Beide tipe koppelings bied 'n wye reeks van koppelingwaardes en kan maklik geimplementeer word in hierdie struktuur. Die voorgestelde struktuur kan ook gemengde koppelings voorstel. Om die konsep te bewys is 'n sesde orde kruiskoppeling banddeurlaat filter met 'n 5% bandwydte teen 5 GHz is ontwerp en gemeet.

Die verhandeling bied die nuwe gedeeltelike luggevulde voetstuk resoneerder aan. Die voetstuk oppervlak geïntegreerde golfleier topologie is aangepas om 'n gedeeltelike lugge-vulde voetstuk oppervlak geïntegreerde golfleier resoneerder te maak om die verliese en toegevoegde Q faktore te verminder terwyl die kleiner vorm behou is. 'n Vergelyking van drie verskillende tipe pedestal resoneerders is gedoen. 'n Geheelgevulde pedestal SIW resoneerder, 'n gedeeltelik luggevulde voetstuk resoneerders en 'n leë voetstuk resoneerder is met mekaar vergelyk om die toenname in Q faktor aan te dui vir dieselfde grootte. Daarna word die gebruik van mikro-masjinerie geillustreer om hierdie nuwe resoneerder te vervaardig en te bespreek. Prototipes van 'n resoneerder en 'n tweede orde filter is vervaardig deur gebruik te maak van die bespreekte proses en daarna getoets. Dit het aangedui dat die Q faktor van 186 vir 'n ten volle di-elektriese resoneerder toe kan neem tot 285 vir 'n gedeeltelike luggevulde resoneerder. Hierdie is 'n toenname van 34,7%.

Die laaste toepassing van die voetstuk resoneerder is met die gebruik van verstelbare strukture. Die voetstuk resoneerder blyk maklik verstelbaar te wees met die toevoeging van PIN diodes aan die voetstuk, wat met 'n annular ring geskei word. Vier verskillende frekwensie stadia word op hierdie manier bereik. 'n Resoneerder 'n derde orde filter is ontwerp, vervaardig en getoets. Goeie verstelbare frekwensie is bereik in simulasie en metings, maar groot verliese is gesien tydens metings.

# Résumé

Cette thèse concerne l'étude de structures de type guide d'ondes intégrés aux substrats (Substrate Integrated Waveguide - SIW) et plus particulièrement les structures appelées Pedestal Substrate Integrated Waveguide. Celle-ci est constituée d'une cavité SIW fonctionnant sur des modes évanescents, chargée par une capacité, laquelle est physiquement constituée d'une plaque métallique située sur un plan intermédiaire et reliée au plan métallique inférieur par un trou métallisé. Ce type de structures, récemment apparue dans la littérature scientifique, apparait comme l'une des solutions pertinentes aux problèmes rencontrés dans le domaine de la conception et l'intégration de filtres micro-ondes. Cette topologie Pedestal SIW est présentée et son fonctionnement est détaillé, puis elle est comparée à d'autres résonateurs micro-ondes classiquement utilisés.

Trois axes de travail autour de cette structure sont ensuite présentés. Le premier concerne la conception de filtres s'appuyant sur ce type de résonateur et présentant des couplages croisés électriques et magnétiques. Le couplage électrique est obtenu grâce à l'introduction d'une ligne en forme de I située au niveau des plaques métalliques chargeant les cavités SIW, tandis que le couplage magnétique est obtenu de façon plus traditionnelle via des iris de couplages. Ces deux types de couplages offrent de larges plages de valeurs de couplage et la configuration proposée peut également produire un couplage mixte. Afin de démontrer la pertinence et la facilité de mise en œuvre, une preuve de concept a été réalisée grâce à un filtre passe-bande d'ordre six à couplage croisé générant des zéros de transmission situés sur les axes réels et imaginaires (zéros de transmission visibles sur la réponse en amplitude et en phase), a été conçu, réalisé et mesuré. Ce filtre présente une bande passante relative de 5 % à 5 GHz.

Le deuxième axe investigué concerne l'utilisation de résonateurs de type Pedestal SIW au sein de structures accordables. Il est démontré que le résonateur est facilement rendu accordable par l'ajout de diodes PIN connectées sur la face supérieure du résonateur sur laquelle est gravée une bague annulaire. Deux résonateurs et un filtre d'ordre trois accordables sur quatre états ont été conçus, réalisés et testés.

Finalement, le troisième axe porte sur le développement de résonateurs Pedestal SIW partiellement vides. L'objectif de l'utilisation d'une telle configuration technologique est de réduire les pertes et d'augmenter les facteurs Q tout en conservant une bonne compacité. Après une étude théorique, les éléments de réalisation technologique sont présentés puis l'optimisation de différentes configurations est menée. Ensuite, La conception, la réalisation et la mesure d'un résonateur et d'un filtre de second ordre sont présentées. Les résultats démontrent une augmentation du facteur de de qualité de l'ordre de 35% par rapport à une structure entièrement emplie de diélectrique, permettant d'atteindre un facteur de qualité de 285.

# Contents

# List of Figures

# List of Tables

# Chapter 1

# Introduction

## 1.1 Background and problem statement

Microwave filters are a fundamental part of modern and future wireless communication systems. Filters are found in systems such as cordless telephones, GPS, Wi-Fi, satellite communication, 5G and wireless computer parts. Filters are typically used for harmonic suppression, inter-modulation product rejection, and radio frequency interference mitigation. Qualities that are important in such systems are low cost, good frequency selectivity, compact size, good roll-off, linear group delay and high quality (Q) factors.

Cavity and planar topologies are commonly used in designing microwave filters. Planar topologies include combline, staircase, interdigital, hairpin, Substrate Integrated Waveguide (SIW) and ring resonator topologies. Cavity filters have a number of benefits such as higher power handling capabilities and higher Q factors. The main drawbacks of these filters are that they are large in size and heavy in weight and expensive. A solution to this problem is planar filters, such as microstrip filters, which are cheaper, smaller and lighter. However, microstrip filters have more losses due to radiating fields, resulting in lower Q factors. A good compromise is SIW filters, which have higher power handling capabilities and higher Q factors than other planar filters [4]. SIW filters also have a smaller footprint than common cavity filters, and are also easy to fabricate and integrate. SIW filters offer a good compromise between size and Q factors.[5]

SIW technology was first introduced in 2001 in [6]. SIW structures are based on waveguide structures and consist of a substrate layer between two layers of metal with via holes along the sides to create the cavity. SIW technology provides a good compromise between standard planar technology and standard waveguide technology. SIW structures are easy to manufacture because the process is based on classical PCB technology which is well established and easily accessible. SIW structures are also easy to integrate into systems, are smaller and lighter in weight than waveguides, have higher power handling capabilities than other planar structures and offer shielding in comparison to planar structures such as microstrip lines. SIW structures have higher Q factors and lower losses in comparison to other planar technologies, however the Q factors are still lower than for standard waveguides because of the presence of substrate material.

The SIW originated from the concept to synthesize non-planar structures with dielectric substrate and create a planar form. SIW structures are formed with dielectric substrate

with metallized posts or via-holes connecting the upper metal plate and lower metal plate. SIW structures are easy to manufacture using through-hole techniques and have similar mode and guided wave characteristics to conventional cavity waveguides. New communication technologies have increased the need for high performance millimeter-wave systems. Conventional planar technology cannot be used at higher frequencies because of the high insertion and radiation losses at these frequencies. The cavity waveguide does not have these drawbacks, however these cavities are not easily compatible with other planar structures and are large and heavy. [7]

All of these technologies are used in coupled resonator (CR) filter designs. CR-filters are well suited for many applications. They offer low loss and narrow bandwidths. CR-filters have the ability to create cross-coupling between non-adjacent resonators, which introduces transmission zeros that can be utilized to increase selectivity, and/or equalization of group delay [8] [9] [10]. Inductive (magnetic, normally denoted as positive) and/or capacitive (electric, normally denoted as negative) cross-coupling can be used.

SIW technology offers a good solution to many of these design requirements. The main contributor to the losses in SIW structures is the presence of substrate material. To solve this, Air-filled SIW structures were proposed in 2006, which achieved reduced loss and increased Q-factors in comparison to standard SIW at the cost of an increase in structural size [11]. The losses associated with the structure are reduced because the main propagating medium is air. AFSIW structures provide a good compromise between standard SIW structures and waveguide structures. Components other than microwave filters have also been designed with AFSIW technology such as phase shifters [12], and a leaky-wave antenna [13]. Filters operating in the C and X frequency bands have obtained Q factors of around 350 [14]. While filters in the K band have obtained Q factors of around 750 [15].

Cavity and planar technologies are commonly used in tunable designs. Electronically tunable microwave filters are needed for their ability to provide flexible centre frequencies and/or bandwidths. Tunable filters are required to have wide tuning ranges, high tuning speeds, linearity, low loss and compact size. The topology chosen for design plays an integrated role in the capabilities of the filter.

The topology and structure of a filter determine the tunability of the filter. There are topologies that are more easily adapted to be tunable. Planar microstrip filters are simply made tunable by adding a tunable element on to the lines [16], [17]. Adding a tunable element in stripline filters is more challenging, since the lines are less accessible. In recent years a lot of work has been done in the field of tunable filters, however a number of areas for improvement still exist, such as improvements regarding loss, repeatability of manufacturing, structure size, tuning range and cost.

To reduce the size disadvantage of SIW versus microstrip, especially for lower frequency designs, the SIW cavity may be reduced by means of loading. One possibility is the use of a pedestal like loading-structure, proposed for a fixed-frequency solution in [18]. This topology offers a good compromise between Q factor and size. This structure also has the possibility to be made tunable with the introduction of lumped elements, such as pin diodes or varactor diodes, into the structure. It is furthermore inexpensive to manufacture in bulk.

Up till now, only a very basic, low order, fixed centre frequency pedestal SIW filter has been published [18]. In this dissertation, the pedestal SIW topology is developed further, by intoducing mixed coupling, partially air filled structures and tunability. A filter having both positive and negative cross-coupling is designed. The pedestal SIW topology is adapted to create partially air filled pedestal SIW resonators to reduce losses and increase Q factors while maintaining small sizes. A solution for frequency tuning is developed and a number of prototypes are designed and evaluated theoretically and experimentally. In this project tunability will be achieved by using switching channels with PIN diodes rather than a continuous frequency range with varactor diodes.

## 1.2 Contributions

The work contains the following main contributions:

- A novel sixth-order pedestal SIW filter utilizing both negative and positive cross-coupling. For this purpose, a sixth order, phase compensated filter at 5 GHz, with one pair of real frequency transmission zeros (using negative cross-coupling) and one pair of imaginary frequency transmisison zeros (using positive cross-coupling) is designed and tested.[19] (Chapter 3 Sec. 3.3 p. 42-50)

- A novel Air-Filled SIW pedestal resonator is developed. (Chapter 4 p. 52 - 62)

- A second order Air-Filled SIW pedestal filter is developed. (Chapter 4 p. 52 - 62)

- A tuning mechanism for centre frequency tuning for a class of pedestal SIW filters is implemented and tested, based on switched topology. (Chapter 5 Sec. 5.3 p. 61 -81)

In addition, a number of smaller contributions are envisaged. These are:

- A detailed parameter study on resonators at 5 GHz. (Chapter 2 Sec. 2.5 p. 16 - 29)

- A detailed comparison of the pedestal SIW topology with classical topologies. (Chapter 2 Sec. 2.6 p. 29 - 31)

## 1.3 Thesis overview

In chapter 2 a detailed parameter study on different types of resonators at 5 GHz are given. The basic resonator concepts are given in detail. Loss mechanisms such as current distribution, surface roughness and dielectric losses are discussed in detail. The CEM analysis of each resonator that is investigated is given in detail. The characteristics of basic planar microwave resonators are presented. The resonators investigated are: $\lambda/2$ open-circuited microstrip, $\lambda/2$ open-circuited stripline, $\lambda/2$ open-circuited coaxial line, microstrip ring and SIW. Finally these resonators are compared and discussed.

Chapter 3 presents the main resonators on which the rest of the thesis is based on, namely the pedestal resonator. A detailed study of the pedestal resonator is given. Different coupling mechanisms are investigated and discussed. A 6th order filter design form first

principles is given with simulated and measured results. Lastly the filter design and results are discussed.

In chapter 4 the novel partially air-filled pedestal resonator (PAPR) is introduced to increase the Q factor of relatively small sized cavities. A comparison of three different types of pedestal resonators is done between a totally filled pedestal SIW resonator, a partially air-filled pedestal resonator and an empty pedestal resonator, showing the increase in Q factor for the same size. Then the use of micro-machining to create these novel resonators is illustrated and explained. A resonator and second order filter prototypes are manufactured, using the manufacturing process explained, and tested.

In chapter 5 the pedestal resonator is made tunable with the introduction of PIN diodes to the base of the structure. The tunable topology is designed step by step and investigated and a small parameter study is done. Tunable resonators with strips and PIN diodes are designed, manufactured and tested. Finally a third order filter is designed, manufactured and tested.

In chapter 6 the conclusion of the research work with recommendations for future work is given.

# Chapter 2

# Microwave resonators

## 2.1   Introduction

Microwave resonators can be used in devices which generate signals of specific frequencies or filter specific frequencies from an incoming signal. Resonators are designed in a number of different shapes at microwave frequencies. The field distribution is affected by the shape of the resonators, therefore the stored electric and magnetic energy are also affected by the shape of the resonator. The following aspects are important when designing a microwave resonator: centre frequency, resonator size, power handling capabilities and the unloaded Q factor. [20]

Most microwave resonators can be classified as planar, co-axial or cavity type. Cavity resonators consist of air-filled cavities usually made up of highly conductive metal, resulting in high Q factors and high power handling abilities. However, cavity resonators are not appropriate for satellite communication applications because it is very costly to use cavity resonators due to size and weight.[21]. Planar resonators are typically etched on substrates and are much smaller, lighter, low in cost and more easily integrated in circuit designs [21]. However, because of loss factors such as metallization, dielectric substrate and radiation, planar resonators have more losses and much lower Q factors [1]. There are three main categories of planar resonators: (1) microstrip resonators, (2) stripline resonators and (3) SIW resonators.

Microwave resonators are the building blocks in a variety of RF components, including filters, oscillators and amplifiers [22], [23] and [24]. At higher Radio Freqyency (RF) and microwave frequencies resonators are seldom realized with discrete lumped element RLC components. This is primarily due to the fact that the small values of inductance and capacitance are physically unrealisable. Even if the values could be physically realized, the resulting Q factor values would be unacceptably low for most applications.

The Q factor of an element relates to the losses associated with the element [20]. This is also directly associated with the bandwidth of the resonator with respect to its centre frequency. This makes the Q factor a particularly important characteristic of any microwave resonator and the main focus of this chapter. A resonator with lower loss and/or narrower bandwidth has a higher Q factor.

Losses in resonators generally arise from three main sources: dielectric material, metal-

lization and leakage [1]. These losses are described as dielectric losses, conductor losses and leakage losses. Conductor losses occur due to the finite resistivity of metallization of walls or lines of resonators and surface roughness, dielectric losses occur due to ohmic losses in the substrate of the resonators and leakage losses occur due to a lack of shielding of the resonators and radiation. [1]

In this chapter, a range of resonators are investigated; microstrip, stripline, coaxial and SIW cavity resonators are considered and compared. Half wavelength straight line, ring, rectangular SIW cavity and coaxial resonators are considered. All the resonators are designed to resonate at 5 GHz, and where substrate is needed, Mercurywave 9350 is used (with $\epsilon_r = 3.5$ and $\tan \delta = 0.004$ ). To reduce the number of parameter studies that need to be done, this study only considers $\lambda/2$ resonators. All the simulations are done in CST using the frequency domain and eigenmode solver with adaptive tetra-hedral meshing. Although much of the information contained in this chapter is widely known, this chapter serves to give a detailed comparative parameter study on microwave resonators and to identify the technology best suited for compact high Q resonators at 5 GHz.

## 2.2   Basic resonator concepts

Microwaves are able to propagate on transmission lines in various forms depending on the construction of the transmission lines. Transmission lines consisting of two or more conductors are able to support transverse electromagnetic (TEM) waves. TEM waves only consist of transverse field components and no longitudinal field components. Waveguides, such as SIW waveguides, however only consist of one conductor. Therefore these types of transmission lines can only support transverse electric (TE) and/or transverse magnetic (TM) waves that consists of both transverse field components and longitudinal field components. [21]

A transmission line can be described in terms of its characteristic impedance, $Z_0$, propagation constant, $\beta$, and attenuation constant, $\alpha$. Different RLC equivalent circuits can be used to model transmission line configurations at different frequencies.

### 2.2.1   Short-circuited $\lambda/2$ line

At resonance a short-circuited $n\lambda/2$ line is equivalent to a series RLC resonator. Figure 2.1 shows a transmission line, of length $l$, terminated in a short circuit with the equivalent series RLC circuit. Resonance will occur at $l = \frac{n\lambda}{2}$ for n = 1,2,3...
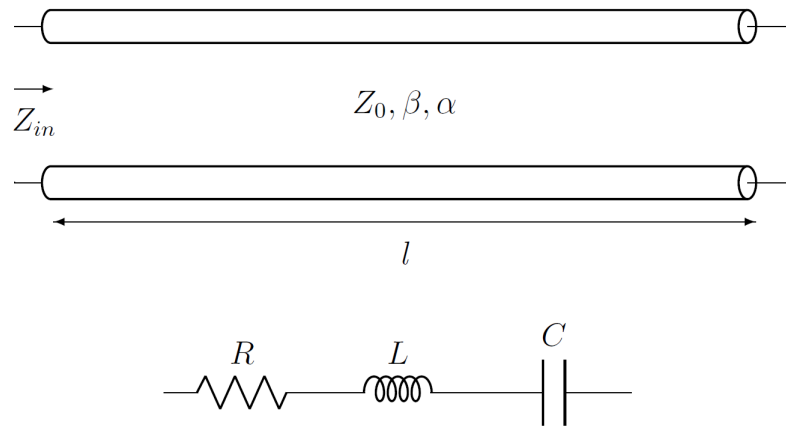
**Figure 2.1:** Short-circuited $\lambda/2$ transmission line and equivalent RLC circuit.

The input impedance of a short-circuited $\lambda/2$ lossy transmission line can be described as [21]

$$Z_{in} = Z_0 \frac{\tanh(\alpha l) + j \tan(\beta l)}{1 + j \tan(\beta l) \tanh(\alpha l)} \tag{2.1}$$

For a low-loss transmission line it is assumed that $\alpha l << 1$, and that $\tanh(\alpha l) \simeq \alpha l$. Let $\omega = \omega_0 + \Delta\omega$ ($\Delta\omega$ is small). Assuming a TEM line, the argument of the tangent function is

$$\beta l = \frac{\omega l}{v_p} = \frac{\omega_0 l}{v_p} + \frac{\Delta\omega l}{v_p} = \pi + \frac{\Delta\omega l}{v_p}$$

And therefore,

$$\tan(\beta l) = \tan\left(\pi + \frac{\Delta\omega l}{v_p}\right) = \tan\left(\frac{\Delta\omega\pi}{\omega_0}\right) \simeq \frac{\Delta\omega\pi}{\omega_0}$$

Substituting this back into the input impedance equation gives ($\Delta\alpha l/\omega_0 << 1$)

$$Z_{in} = Z_0 \frac{\alpha l + j(\Delta\omega\pi/\omega_0)}{1 + j(\Delta\omega\pi/\omega_0)\alpha l} \simeq Z_0\left(\alpha l + j\frac{\Delta\omega\pi}{\omega_0}\right) \tag{2.2}$$

Equation 2.2 is in the form

$$Z_{in} = R + 2jL\Delta\omega \tag{2.3}$$

which is the input impedance of a series RLC resonant circuit. Setting Eq. 2.3 to the RLC circuit input impedance yields

$$R = Z_0\alpha l \tag{2.4}$$

$$C = \frac{\pi}{4\omega_0 Z_0} \tag{2.5}$$

$$L = \frac{1}{\omega_0^2 C} \tag{2.6}$$

(At resonance $\beta l = \pi$) The unloaded Q can be calculated as

$$Q_0 = \omega_0 RC = \frac{\pi}{4\alpha l} = \frac{\beta}{2\alpha} \tag{2.7}$$

This shows that the unloaded Q factor decreases as the attenuation of the line increases.

## 2.2.2 Open-circuited $\lambda/2$ line

At resonance an open-circuited $\lambda/2$ line is equivalent to a parallel RLC resonator. Figure 2.2 shows a length of transmission line terminated in an open circuit with the equivalent parallel RLC circuit.
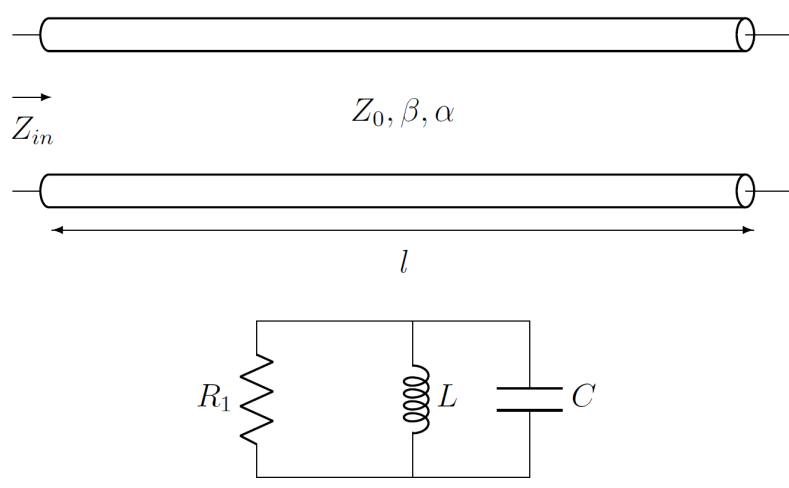


**Figure 2.2:** Open-circuited $\lambda/2$ transmission line and equivalent RLC circuit.

The input impedance of an open-circuited $\lambda/2$ lossy transmission line is described as [21]

$$Z_{in} = Z_0 \frac{1 + j\tan(\beta l)\tanh(\alpha l)}{\tanh(\alpha l) + j\tan(\beta l)} \tag{2.8}$$

For $l = \lambda/2$, $\omega = \omega_0$ and $\omega = \omega_0 + \Delta\omega$ , the tangent function argument becomes

$$\beta l = \pi + \frac{\pi \Delta\omega}{\omega_0}$$

allowing the tangent function to be replaced by

$$\tan(\beta l) \simeq \frac{\Delta\omega}{\omega_0}$$

By using the small-angle rule for tangential functions, $\tanh(\alpha l) \approx \alpha l$ , the resulting input impedance is

$$Z_{in} = \frac{Z_0}{\alpha l + j(\Delta\omega\pi/\omega_0)} \tag{2.9}$$

Equation 2.9 is of the same form as the input impedance of a parallel RLC circuit, as provided below.

$$Z_{in} = \frac{R}{1 + 2jQ_0\Delta\omega/\omega_0} \tag{2.10}$$

Similar to the shorted half-wavelength case, the resistance, capacitance and inductance of the transmission may be extracted by Eq. 2.9 and 2.10 to one another, which yields

$$R = \frac{Z_0}{\alpha l} \tag{2.11}$$

$$C = \frac{\pi}{2\omega_0 Z_0} \tag{2.12}$$

$$L = \frac{1}{\omega_0^2 C} \tag{2.13}$$

The unloaded Q at resonance $l = \pi/\beta$ is therefore,

$$Q_0 = \omega_0 RC = \frac{\pi}{2\alpha l} = \frac{\beta}{2\alpha} \tag{2.14}$$

As expected, it is shown that the unloaded Q factor decreases as the attenuation of the line increases.

Similar derivations may be done to prove that a short-circuited $\lambda/4$ transmission line is equivalent to a parallel RLC resonant circuit and an open-circuited $\lambda/4$ transmission line is equivalent to a series RLC resonant circuit at resonance.

Parallel resonant circuits are often used as one port resonators. Near the resonant frequency, the one port resonator behaves as a serie/parallel RLC network. One port resonators are coupled to one another to form filter networks.

## 2.3   Loss mechanisms

There are several mechanisms that contribute to the overall observed loss in microwave resonators, including the current distribution, skin effect, surface roughness and dielectric material.

## 2.3.1   Current distribution

Current density is defined as electric current (charge flow) per unit area of cross-section. The result is a vector field. When an electric field is applied to a material with a specific conductivity $\sigma$ , a conduction current density will exist

$$J = \sigma E$$

where, $\sigma$ = electric conductivity (S/m).

The current density changes as the current flow changes. When the current is alternating at a specific frequency, the current density tends to become larger near the surface of the conductor and decreases with greater depth in the conductor. This is called the skin effect. The higher the frequency, the greater this effect becomes. It is defined as the distance within a conductor where the current density drops 37% of the value at the surface. [21]

The skin depth can be defined as [21]

$$\delta = \frac{1}{\sqrt{\pi f \mu_0 \sigma}}$$

where,
$\delta$ = skin depth (m)
$\omega$ = angular frequency (1/s)
$f$ = frequency (Hz)
$\mu$ = the permeability of a medium (H/m)
$\sigma$ = conductivity (S/m)

From this equation it is clear that the skin depth is inversely proportional to the square root of the frequency and conductivity. Thus, the skin depth will decrease as the frequency increases, and will also decrease as the conductivity increases. The skin depth does not depend on the shape of the conductor. Normal metals have relatively high conductivities, therefore the skin depth becomes very small at high frequencies.

By changing the effective cross-sectional area of the conductor the effective resistance of the conductor is changed as a function of frequency. Because of this effect the effective cross-section of a conductor decreases from the total cross section to a fraction of the total cross-section. This increases conductor resistance and thus also conductor losses. The skin effect is one of the two primary causes of losses in lossy planar transmission lines (the other is dielectric losses). At a certain frequency the skin effect will start to limit the effective cross-sectional area of the conductor, this is called the crossover frequency.[25]

The power loss into a cross-section of a conductor can be calculated as [21]

$$P_l = \frac{R_s}{2} \int_s |\bar{J}_s|^2 \, ds \quad \text{W/m}^2 \tag{2.15}$$

$$\tag{2.16}$$

From this equation it is clear that the shape of the current distribution has an effect on the total loss due to the current on the conductor. For example, a microstrip conductor consists of a line conductors with sharp edges, which causes peaks in the current distribution, as shown in Fig. 2.4. The microstrip line therefore has a larger power loss as opposed to a smoother conductor such as a coaxial line.

Figure 2.3 shows the cross-section of a microstrip conductor. A typical current distribution on the conductor can be seen in Fig. 2.4.
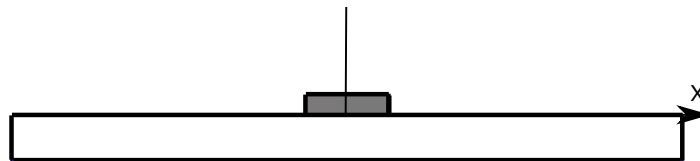
**Figure 2.3:** Cross-section of microstrip conductor.
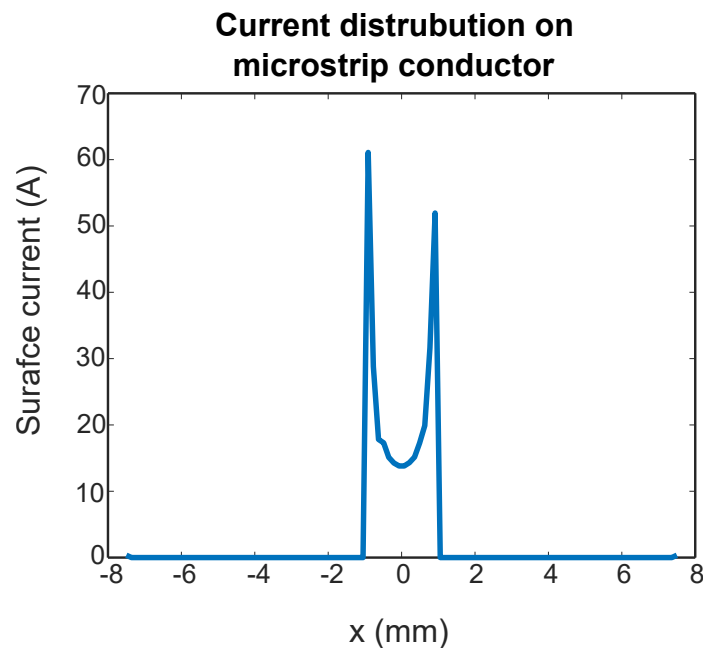
**Figure 2.4:** Current distinction on microstrip conductor.

It is clear that the skin effect and shape of the conductor effects the power loss associated with the conductor.

## 2.3.2 Surface roughness

Materials are not ideally smooth, but have a microscopically rough surface. Surface roughness occurs during metalization and the result is an inhomogeneous current in the conductor. The current is concentrated around the surface of the conductor because of the skin effect explained in section 2.3.1. The disruption of the current flow results in an effective increase of surface resistivity, thus also an increase in conductor losses. The effective surface roughness is given as

$$\sigma_{eff} = \sqrt{\frac{1}{X_p} \int_0^{X_p} \sigma^2(x)dx} \qquad (2.17)$$

The surface roughness is assumed to be periodic with $X_p$ as the period and $\sigma(x)$ as the surface profile.



(a) Surface profile of conductor.

(b) Microstrip conductor with triangular surface roughness.
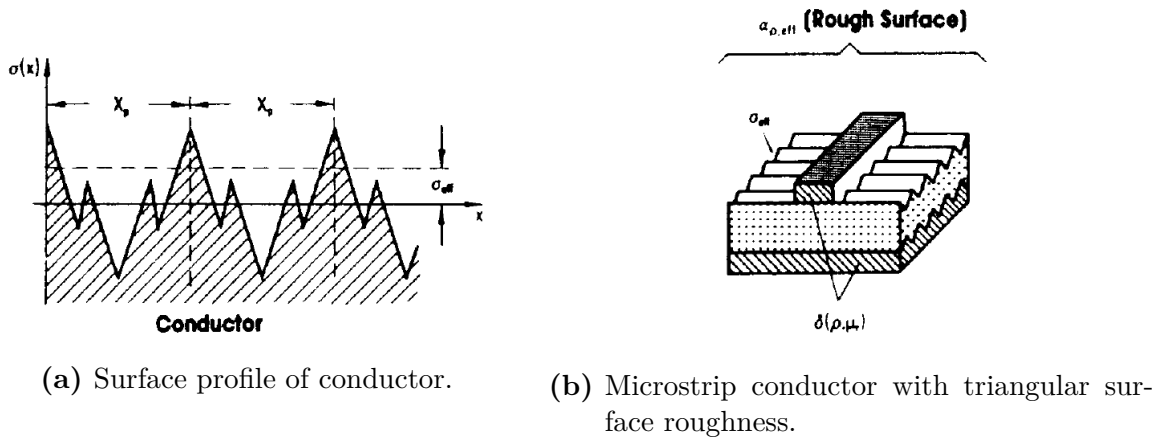
**Figure 2.5:** Surface profile of conductor and microstrip conductor with triangular surface roughness [1].

The conductor loss for a flat surface $\alpha_c$ can be used to calculate the conductor loss for a rough surface $\alpha_{c,eff}$. From [1] $\alpha_c \approx R_s$, where $R_s$ is the specific surface resistance, resulting in the following relationship for the same material

$$\frac{\alpha_{c,eff}}{\alpha_c} = \frac{R_{s,eff}}{R_s} \qquad (2.18)$$

The perturbation method can be used to calculate the attenuation constant for conductor loss. The conductor loss depends on the field distribution on the line or in the guide and thus has to be calculated separately for each transmission line or waveguide. As an example the attenuation constant for a microstrip line is given in Eq. 2.43. The effective attenuation constant can be approximated by [1]

$$\frac{\alpha_{c,eff}}{\alpha_c} = \frac{R_{s,eff}}{s_F} = 1 + (2/\pi) \arctan 1.4(\sigma_{eff}/\delta)^2 \qquad (2.19)$$

In CST the surface roughness can be specified. The surface profile is modeled as a random process with a normal distribution. When using this parameter, a gradient of the conductivity (perpendicular to the surface) and an effective frequency dependent impedance is computed which accounts for the increased total loss and increased inner inductance effects. The surface roughness and thus surface resistance can be decreased by plating or chemical polishing, however this is more costly.

### 2.3.3 Dielectric loss

Ohmic losses in the substrate of a resonator results in dielectric losses in the resonator. Dielectric losses can be described by a dielectric loss tangent $\tan \delta$ that is frequency independent. Calculation for attenuation caused by dielectric loss can be divided into two groups. The case for inhomogenuous structure and the case for homogeneous structure.

For the case of a microstrip line where we have an inhomogenous structure, Eq. 2.44 can be used. For the case where the line or guide is completely filled with lossy dielectric material the attenuation constant can be calculated from the propagation constant. When a lossy dielectric material is used $\epsilon$ becomes complex $\epsilon = \epsilon_0 \epsilon_r (1 - j \tan \delta)$. [21]
The complex propagation constant is written as

$$\gamma = \alpha_d + j\beta \tag{2.20}$$

$$= \sqrt{k_c^2 - \omega^2 \mu_0 \epsilon_0 \epsilon_r (1 - j \tan \delta)} \tag{2.21}$$

Because $\tan \delta \ll 1$, the expression above can be simplified using the Taylor expansion. Then Eq. 2.21 reduces to

$$\gamma = \sqrt{k_c^2 - k^2 + jk^2 \tan \delta)} \tag{2.22}$$

$$\simeq \sqrt{k_c^2 - k^2} + \frac{jk^2 \tan \delta}{2\sqrt{k_c^2 - k^2}} \tag{2.23}$$

$$= \frac{k^2 \tan \delta}{2\beta} + j\beta \tag{2.24}$$

since $\sqrt{k_c^2 - k^2} = j\beta$ and $k = \omega\sqrt{\mu_0 \epsilon_0 \epsilon_r}$ (where k is the real wave number). From Eq. 2.24 it is clear that the attenuation constant due to dielectric loss is given by

$$\alpha_d = \frac{k^2 \tan \delta}{2\beta} \quad \text{Np/m} \quad \text{(TE or TM waves)} \tag{2.25}$$

This result applies to any TE or TM wave with a homogeneous structure. It can also be used for TEM lines, where kc = 0, by letting $\beta = $ k

$$\alpha_d = \frac{k \tan \delta}{2} \quad \text{Np/m} \quad \text{(TEM waves)} \tag{2.26}$$

For the simulations, realistic values were used.

## 2.4   CEM analysis of resonators

In this section the solver setup, mesh settings and material settings are given for all the simulations presented in this chapter. An overview on how CST operates and the equations CST uses is given and discussed.

### 2.4.1   Solver setup

Each simulation is done with the eigenmode solver. The method setting is set to default with the number of modes to be calculated set to 4. The option for losses to be considered in post processing only is selected. The solver order is set to be 2nd with good accuracy. The solver accuracy is set to 1e-6. The option for static modes and thermal losses to be considered is selected. The thermal losses howere do not have an effect on the results. The option for lossy dielectric to be simulated as loss free is not selected, as well as the option for lossy metal and surface impedance to be simulated as PEC is also not selected. The option for the thin wire model to be applied to solid wires is not selected. The use of sensitivity analysis is not selected.

The frequency range is set from 0 GHz to 10 GHz as the resonators to be considered are designed at 5 GHz. The background is selected to be PEC with electric boundaries on all sides. There are no symmetry planes. No ports are used as the eigenmode solver is used.

### 2.4.2   Mesh settings

In the following section the mesh properties and set up is given. Tetrahedral meshing is to be used for each simulation. Refined tetrahedral mesh is selected with the maximum frequency variation set to 0.01 and minimum number of passes set to 2, the maximum number of passes is set to 6 and the number of modes to check is 10. The maximum cell is set to be automatic. Cells per maximum model box edge for the model is set to be 10 and for the backgroun is set to be 1. The minimum cell is set to be absolute (0). The meshing method to be used is set to surface based, which is the default.

The special mesh properties are as follows: the smooth mesh with equilibrate is set to 1.5. Mesh optimization is selected. The option to consider material properties for refinement is selected. The automatic edge refinement step width is set to 0. The option for the mesh to be moved on parameter change is not selected.

The curvature approximation settings are as follows: a normal tolerance is used (22.5 degrees). Anisotropic curvature refinement is selected. The curvature element is set to be automatic.

### 2.4.3   Material settings

For each simulation the dielectric material to be used is Mercury wave 9350, this material was chosen because it is the standard substrate material that is used at the local manufacturing company that is used for these designs. A new material is created of type normal with $\epsilon_r = 3.5$, $\mu = 1$ and $\tan \delta = 0.004$ at 10 GHz with the specification set to constant. fit tan delta, the user order is not selected. The magnetic conductivity is set to 0 1/Sm. The frequency range is set from 0 to 10 GHz. $\rho = 0$ kg/m^3. The thermal settings are as

follows: the type is set to normal with thermal conductivity set to 0 W/K/m and specific heat also set to 0 J/K/kg. All bioheat settings are 0.

The metal part of each resonator is set to Copper (pure) with type as lossy metal. (Electric conductivity= 5.96e+07 S/m and $\mu = 1$). The surface roughness is set to be 0 mm. The thermal settings are as follows: the type is set to normal with thermal conductivity set to 401.0 W/K/m and specific heat set to 390 J/K/kg. The material density ($\rho$) is default 8930 kg/mˆ3 and thermal diffusivity is 0.000115141 mˆ2/s. All bioheat settings are 0. It is important to note that the electric conductivity used in the post processing step is also set to 5.96e+07 S/m. The mechanics settings are left unchanged as follows: the type is normal with Young's modulus 120 GPa, Poisson's ratio 0.33 and the thermal expansion coefficient 17 1e-6/K.

In the instances where a air box is used such as the case for the $\lambda/2$ open-circuited microstrip line and microstrip ring resonator, the box is filled with vacuum.

### 2.4.4 CST results

Various methods for Q-factor measurement and calculation exist, for most cases the Q factor can most accurately be expressed as the total energy stored over the total losses. In CST the following equations are used to calculate the total loss and Q values. The total loss power is defined as the sum of the dielectric loss power and surface loss power

$$P_T = P_d + P_c \tag{2.27}$$

The dielectric and surface loss powers are defined respectively as follows

$$P_d = \pi f \tan(\delta)\epsilon_0\epsilon_r \int \left|\vec{E}\right|^2 dv \tag{2.28}$$

$$P_c = \frac{1}{2}\sqrt{\frac{\pi\mu f}{\sigma}} \int \left|\vec{H_{tan}}\right|^2 ds \tag{2.29}$$

The total energy stored in the structure is equal to the sum of the electric and magnetic energy

$$W_T = W_E + W_H \tag{2.30}$$

The stored electrical and magnetic energy is given as

$$W_E = \frac{1}{2}\epsilon_0\epsilon_r \int |E|^2 dv \tag{2.31}$$

$$W_M = \frac{1}{2}\mu_0\mu_r \int |H|^2 dv \tag{2.32}$$

The Q factor is then given by

$$Q = 2\pi\frac{W_T}{P_T} \tag{2.33}$$

It can be shown that Eq. 2.7 may hold for any general resonator.

With the eigenmode solver the Q factor is calculated at a specific mode. Unlike the frequency domain solver, where open boundaries may be used, in the eigenmode solver open boundaries are not possible, thus an air box has to be used when needed causing an increase in the calculated Q factor as energy is not allowed to dissipate.

It is important to note that CST calculates the loss and Q factor in a post-processing step, thus when the field distributions are calculated ideal conditions are assumed and all metal are assumed to be PEC. In the post-processing step the conductor conductivity is taken into account, for both the resonator and the enclosure.

The loss tangent of a material is usually specified at a certain frequency which is normally not the resonance frequency. Thus to obtain more accurate results it is important to specify at which frequency the material should be evaluated.

For all the simulations in this chapter, a line thickness of 0.068 mm is used with no surface roughness. To obtain more accurate results a surface roughness can to be specified. With thin lines it is important to refine the mesh in order to obtain accurate results for the field distribution and surface current distribution.

When using the frequency domain solver input and output coupling to the resonator is needed. For instance, with a microstrip ring resonator microstrip lines are usually used to couple to the ring resonator. The Q factor obtained with this design is strongly determined by the strength of the coupling to the ring resonator. When strongly coupled, a lower Q is obtained, while a higher Q is obtained when coupled weakly. When this approach is used the loaded Q factor is calculated.

## 2.5   Characteristics of basic microwave resonators

In this section each resonator is discussed in detail with focus on the characteristic impedance, Q factor and loss. Details on specific aspects of resonators are given and each resonator topology with corresponding field distributions are given. These specific resonators are chosen because they are used in designs around 5 GHz.

### 2.5.1   $\lambda/2$ open-circuited microstrip resonators

Microstrip resonators are conductor lines etched on a grounded dielectric substrate, as illustrated in Fig. 2.6. Microstrip resonators are one of the most common topologies used to design microwave resonators and filters, primarily because of small size, ease of manufacturing and low cost [1]. The majority of the fields are contained within the dielectric substrate. However a fraction of the fields are radiating, this results in the phase velocities of the fields being different. Therefore, the waves associated with microstrip lines are not purely TEM-waves. The fields are commonly known as being quasi-TEM. Therefore, the phase velocity, propagation constant, and characteristic impedance can be closely approximated from static, or quasi-static, solutions. [21]

Radiation effects are present at any discontinuity section because microstrip lines are not shielded, which adds extra radiation or leakage losses. The leakage losses depend on the dielectric constant, substrate thickness and circuit geometry. The lower the dielectric con-

stant, the less concentration of energy is in the substrate region, and hence, the greater the leakage losses [1]. The fringing fields at the open ends of a straight line microstrip resonator also results in foreshortening of the line [26].

The electric and magnetic field distributions can be seen in Fig. 2.7(a) and Fig. 2.7(b). Quasi-TEM (hybrid mode) has non-zero electric and magnetic fields in the direction of propagation. These modes are a combination of the transverse electric (TE) and transverse magnetic (TM) modes, thus have the longitudinal components of the electric and magnetic fields. The wave propagates in two different media (air and dielectric) in a hybrid mode.
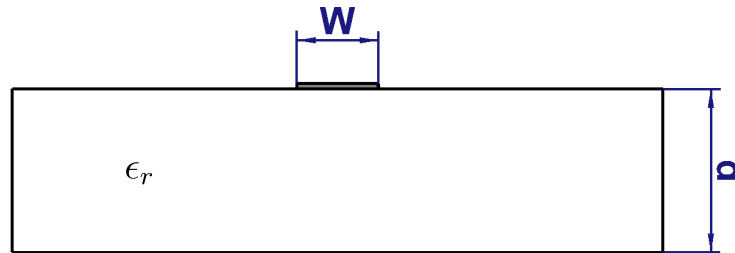


**Figure 2.6:** Cross-section of microstrip line.



**(a)** E-field distribution of microstrip line.     **(b)** H-field distribution of microstrip line.
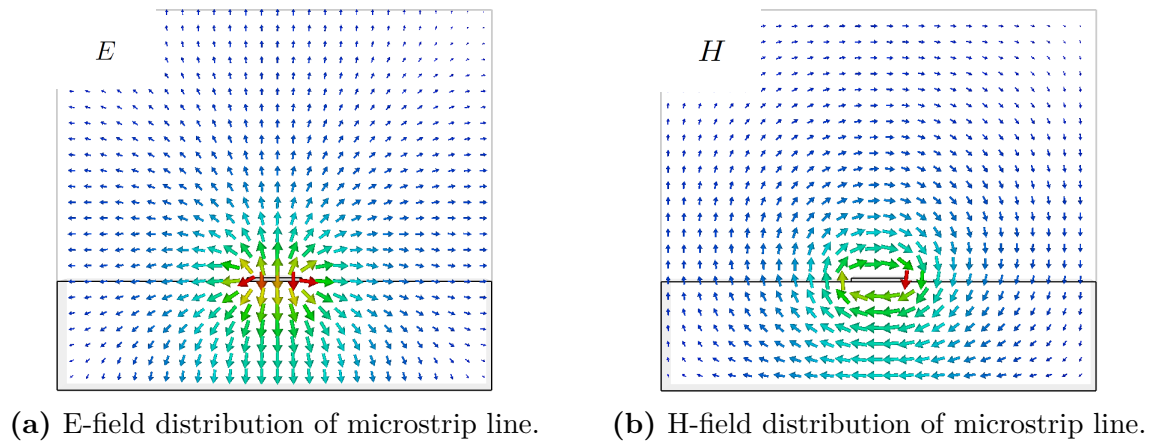
**Figure 2.7:** E and H -field distribution of microstrip line.

The phase velocity and propagation constant of a microstrip line can be expressed as

$$v_p = \frac{c}{\sqrt{\epsilon_{eff}}} \tag{2.34}$$

$$\beta = k_0\sqrt{\epsilon_{eff}} \tag{2.35}$$

where $\epsilon_{eff}$ is the effective dielectric constant of the microstrip line given as [21]

$$\epsilon_{eff} \simeq \frac{\epsilon_r + 1}{2} + \frac{\epsilon_r - 1}{2}\frac{1}{\sqrt{1 + 12d/W}} \tag{2.36}$$

Given the dimensions of the microstrip line the value of the characteristic impedance is calculated as [21]

$$
Z_0 = \begin{cases} \dfrac{60}{\sqrt{\epsilon_{eff}}} \ln\left(\dfrac{8h}{W} + \dfrac{W}{4d}\right) & \text{for } \dfrac{W}{d} \leq 1 \\[4mm] \dfrac{120\pi}{\sqrt{\epsilon_{eff}}\left(\frac{w}{d} + 1.393 + 0.667\ln\left(\frac{W}{d} + 1.444\right)\right)} & \text{for } \dfrac{W}{d} \geq 1 \end{cases}
$$

$$\text{(2.37)}$$
$$\text{(2.38)}$$

$$
\frac{W}{d} = \begin{cases} \dfrac{8e^A}{e^{2A} - 2} & \text{for } \dfrac{W}{d} < 2 \\[4mm] \dfrac{2}{\pi}\Big(B - 1 - \ln(2B - 1) + & \text{for } \dfrac{W}{d} > 2 \\[2mm] \dfrac{\epsilon_r - 1}{2\epsilon_r}\left(\ln(B - 1) + 0.39 - \frac{0.61}{\epsilon_r}\right)\Big) & \end{cases} \quad.
$$

$$\text{(2.39)}$$
$$\text{(2.40)}$$

$$
A = \frac{Z_0}{60}\sqrt{\frac{\epsilon_r + 1}{2}} + \frac{\epsilon_r - 1}{\epsilon_r + 1}\left(0.23 + \frac{0.11}{\epsilon_r}\right) \tag{2.41}
$$

$$
B = \frac{\eta_0 \pi}{2Z_0\sqrt{\epsilon_r}} \tag{2.42}
$$

The effect of the substrate height and line width on the characteristic impedance of a microstrip line, is shown in Fig. 2.8(a) and 2.8(b) respectively. To obtain the results in Fig. 2.8(a) $W$ is kept constant at 1 mm and $d$ is increased from 0.1 to 1 mm. To obtain the results in Fig. 2.8(b) $d$ is kept constant at 1 mm and $W$ is increased from 0.1 to 1 mm.
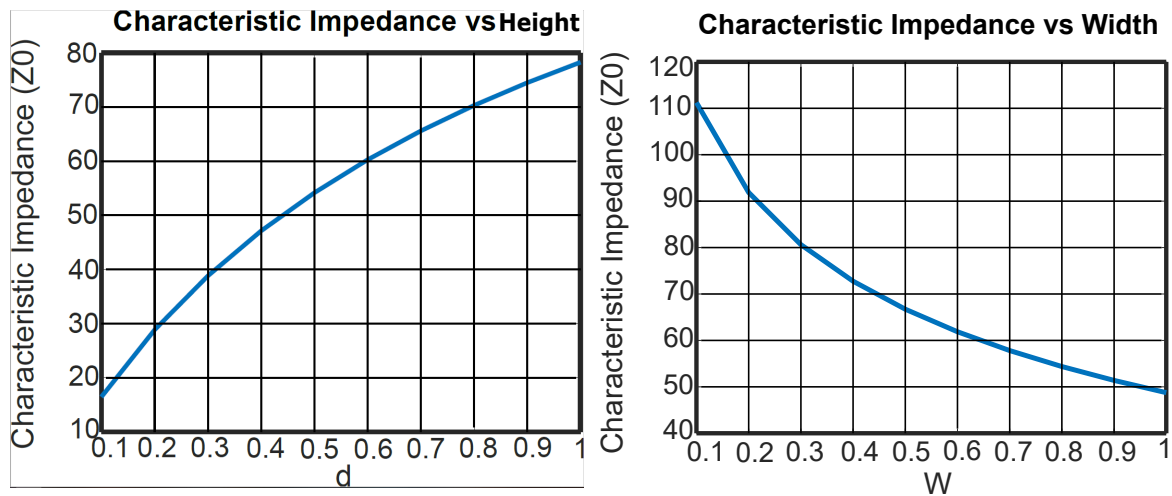


**(a)** Characteristic impedance vs height of microstrip line ($W = 1$ mm).

**(b)** Characteristic impedance vs width of microstrip line ($d = 1$ mm).

**Figure 2.8:** Characteristic impedance of micro-strip resonator.

It is clear that the characteristic impedance is directly proportional to the substrate height, but inversely proportional to the line width. As the substrate height increases the per unit capacitance between the line and ground plane decreases, thus from Eq.

2.5 the characteristic impedance increases. As the width of the line increases the total capacitance between the line and ground plane increases and therefore the characteristic impedance decreases as supported by Eq. 2.5.

### 2.5.1.1   Q factor and loss

As discussed in section 2.3 there are three main types of losses present in microwave resonators. These are conductor losses, dielectric losses and leakage losses. The finite resistance due to the line and ground plane metallization is the main contributor to the conductor loss coefficient $\alpha_c$ given as [21]

$$\alpha_c = \frac{R_s}{Z_0 W} \quad \text{Np/m} \tag{2.43}$$

where $R_s = \sqrt{\omega\mu_0/2\sigma}$.

The dielectric losses in the microstrip resonator are due to the ohmic losses in the dielectric substrate. The air above the substrate is normally considered lossless. The dielectric loss coefficient can be given as [21]

$$\alpha_d = \frac{k_0\epsilon_r(\epsilon_e - 1)\tan\delta}{2\sqrt{\epsilon_e}(\epsilon_r - 1)} \quad \text{Np/m} \tag{2.44}$$

Enclosure losses in microstrip resonators are due to the finite conductivity of the line and ground plate metallization. The leakage loss coefficient can be given by [1]

$$\alpha_\sigma = 1.64 \times 10^3 \sigma \sqrt{\frac{1 + W/d}{2}\left(\epsilon_r + \frac{1 - W/d}{1 + W/d}\right)^{-1}} \quad \text{Np/m} \tag{2.45}$$

where $\sigma$ is the conductivity of the metal used. The simulations here are done with a closed roof spacing on top of the microstrip line and fixed line length. It is important to note that the Q factor will change depending on the height of the roof. For a larger roof the Q factor will increase as the surface currents on the roof are less, therefore contributing less to conductor loss. The results shown is for a roof of 10 mm . A sweep of the line width ($W$) was done from 0.6 mm to 2 mm for different dielectric thicknesses from 0.2 mm to 1.8 mm.
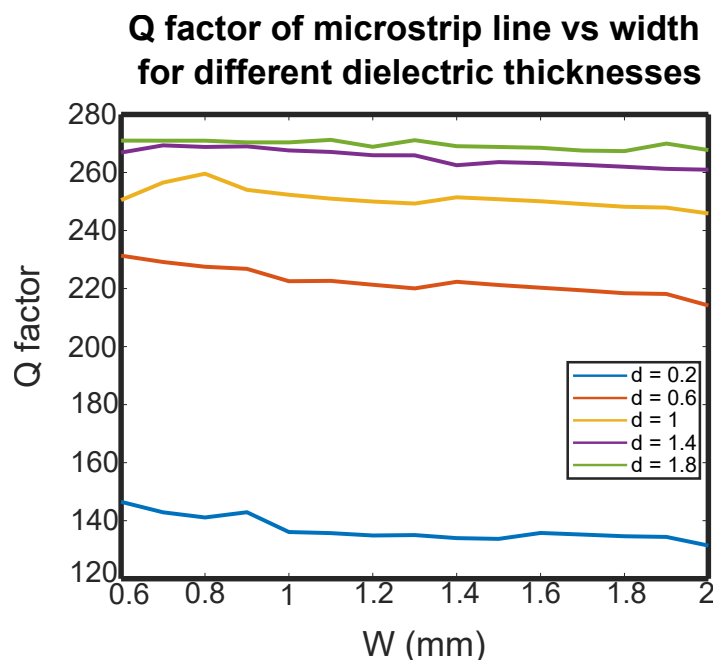
**Figure 2.9:** Q factor of microstrip line vs width for different dielectric thickness.

It is clear that the Q factor increases as the roof height increases. This is due to the decrease in both surface loss and dielectric loss. The decrease in surface loss and dielectric loss can be attributed to the decrease in field strength for both electric field and magnetic field. This is supported by Eq. 2.29 and 2.28. The rate at which the Q factor increases, decreases as the dielectric thickness increases. As the dielectric thickness increases the field distribution changes less. The Q factor and total loss remain relatively constant as the width of the strip increases, therefore the width does not have a substantial effect on the Q factor and total loss of the structure. This is because the main contributor to the total loss is the volume loss (dielectric loss). For the case where the dielectric thickness is $d = 1$ mm the contribution of volume loss (dielectric loss) with $\tan \delta = 0.004$ is 85% and the contribution of conductor losses are only 8.38%. However, for the case where the $\tan \delta = 0.0001$ the the contribution of volume loss (dielectric loss) drops to 12.4% and the contribution of conductor loss increases to 49% (the rest of the losses is due to the enclosure surface currents). From this it is clear that when a dielectric material with a $\tan \delta = 0.0001$ is used, a greater change in Q is noticed because the main contributor to the change in loss is the conductor.

## 2.5.2 Stripline resonator

A stripline consists of two parallel metallic plates, normally separated a distance $d$ by a dielectric material with a thin conducting strip of width $W$ between the two conducting plates as seen in Fig. 2.10. Striplines also fall within the planar transmission line category. The two conducting paths enable striplines to support TEM waves with the signal and ground currents flowing on separate conductors [21]. One benefit of stripline structures is that at high frequencies, emission and interference is minimized due to the shielded nature of a stripline [1]. Stripline structures are considered to be non-radiating structures. Another benefit is that stripline structures can, like microstrip structures, be constructed with high accuracy using low-cost circuit board materials and processes.

Since the dielectric medium is homogeneous, unlike microstrip structures, the phase velocity and characteristic impedance of the dominant TEM mode do not vary with frequency [21]. The E and H-field distributions can be seen in Fig. 2.11.
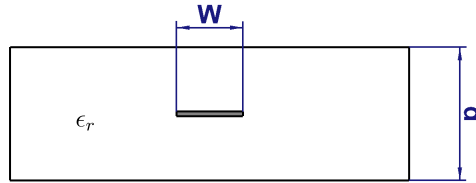


**Figure 2.10:** Cross-section of stripline.
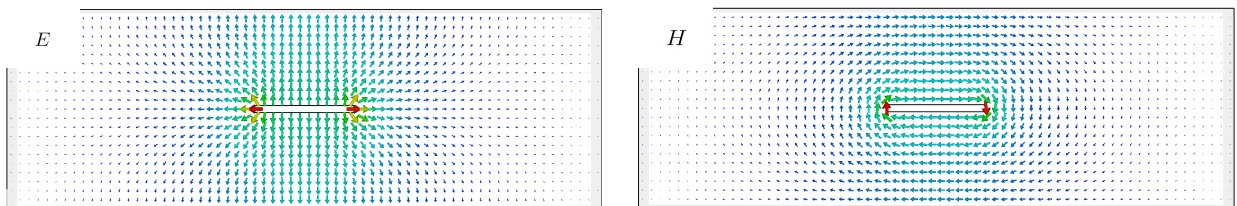


**Figure 2.11:** E and H field distributions of stripline.

In multilayered structures, various parts can be integrated vertically, thus saving space. Stripline is often used in multilayered structures because it can easily be placed between other planar components, making these structures ideal for applications in satellite systems. Another advantage of stripline is that it is already "boxed-in" also lending it well for satellite systems.[27] [28]

An important advantage of a two-conductor transmission line includes having no low-frequency cut-off, thus it can be utilized over a very broad frequency range. Performance limitations of stripline structures are often due to attenuation caused by finite conductivity and finite resistivity of the dielectric material. At higher frequencies the dielectric loss dominates.[1] The surface loss depends on the conductivity of the conductor and any surface roughness. One disandvantage of stripline structures is that they are difficult to connect electrically, requiring high precision and expensive connectors. Another disadvantage is that the fields in the transmission line tend to concentrate around the conductor, which has a smaller cross-section, thus limiting the power handling capabilities.

The characteristic impedance of a stripline depends on the dielectric constant and the cross-sectional geometry of the centre conductor and ground plates. From Eq. 2.47 [21] it is clear that the characteristic impedance is sensitive to the ratio of centre conductor width to dielectric thickness. However, the characteristic impedance is insensitive to the ratio of centre conductor thickness to dielectric thickness.

$$\frac{W_e}{d} = \frac{W}{d} - \begin{cases} 0 & \text{for } \frac{W}{d} > 0.35 \\ (0.35 - \frac{W}{d})^2 & \text{for } \frac{W}{d} < 0.35 \end{cases} \tag{2.46}$$

$$Z_0 = \frac{30\pi}{\sqrt{\epsilon_r}} \frac{d}{W_e + 0.441d} \tag{2.47}$$

For a constant dielectric thickness $d = 1$ mm the width of the centre-conductor was varied from 0.1 to 1 mm. In Fig. 2.16(a) the characteristic impedance is plotted against height, the centre conductor remains constant ($W = 0.43$ mm). In Fig. 2.16(b) the height of the centre conductor remains constant ($d = 1$ mm) while the width of the centre-conductor is varied from 0.1 to 1 mm.
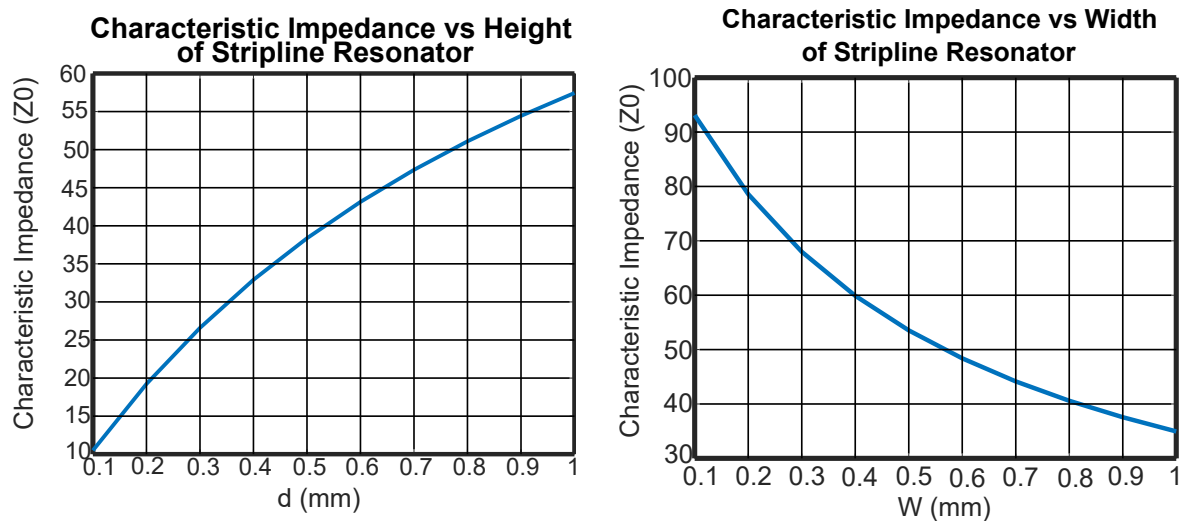


**(a)** Characteristic impedance vs height of stripline resonator ($W = 0.43$ mm).

**(b)** Characteristic impedance vs width of stripline resonator ($d = 1$ mm).

**Figure 2.12:** Characteristic impedance of stripline resonator.

From Fig. 2.16(a) it is evident that the characteristic impedance of the line increases as the height increases. The total capacitance between the centre conductor and two ground planes decreases as the height is increased, thus from Eq. 2.12 the characteristic impedance increases. It is clear that as the width is increased the characteristic impedance decreases for a constant height, as shown in Fig. 2.16(b). As the width of the centre conductor increases the total capacitance between the conductor and plates increases, thus from Eq. 2.12 the characteristic impedance decreases. This is also supported by Eq. 2.47.

### 2.5.2.1 Q factor and loss

A sweep of the line width $W$ is done from 0.6 mm to 2 mm for different dielectric thickness ranging from 0.2 mm to 1.8 mm.
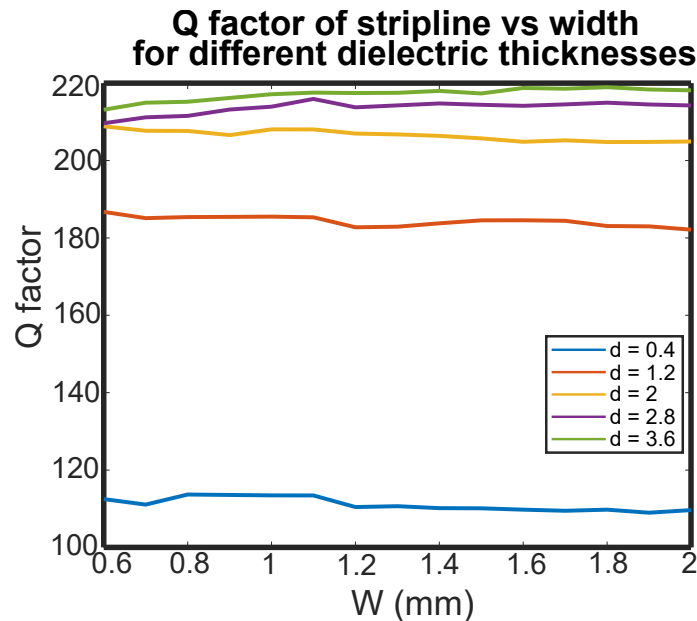
**Figure 2.13:** Q factor of stripline vs width for different dielectric thicknesses.

The Q factor remains relatively constant as the width of the line increases while the Q factor increases as the dielectric thickness increases. This is for the same reason explained in the previous section on microstrip lines. For the case where $\tan\delta = 0.004$ is used the volume losses is again the main contributing factor to the total losses (83.3%). A stripline normally consists of two layers of substrate, thus the dielectric thickness $d$ of a stripline is twice the dielectric thickness $d$ for a microstrip line, resulting in higher volume losses. For a microstrip line with dielectric thickness $d = 1$ mm a Q factor of around 250 is achieved, while a Q factor of around 210 is achieved for a stripline with dielectric thickness $d = 2$ mm. This is because a proportion of the fields from the microstrip line is in lossless air as opposed to a lossy dielectric media.

### 2.5.3 Coaxial resonator

Oscillators and filters are often designed using coaxial resonators [22], [23]. A coaxial transmission line is similar to a stripline in that it has a centre conductor. A coaxial transmission line, with a cross-section as shown in Fig. 2.14, can be seen as a cylindrical stripline. The inner conductor is at a specific potential while the outer conductor is at 0 V, the same as for stripline. A coaxial line supports TE and TM waveguide modes in addition to TEM modes [21]. The E and H-field distributions of a coaxial resonator can be seen in Fig. 2.21(a) and 2.21(b).
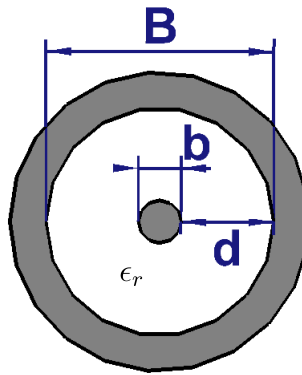
**Figure 2.14:** Cross-section of coaxial line.
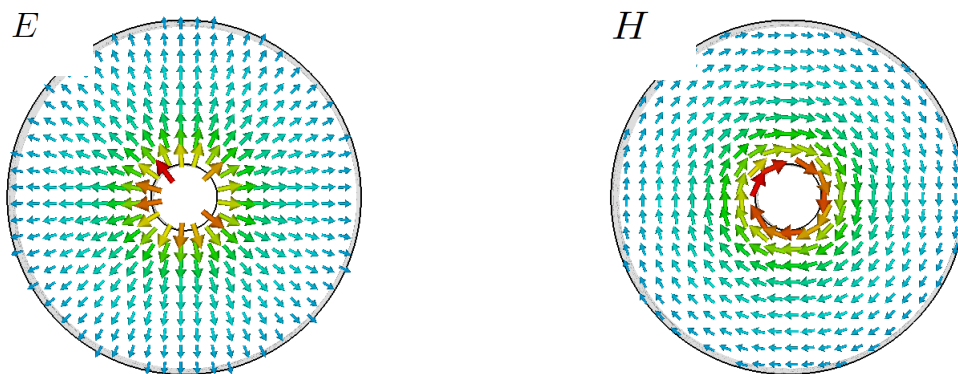


**(a)** E-field distribution of coaxial line.

**(b)** H-field distribution of coaxial line.

**Figure 2.15:** E and H - TEM field distribution of coaxial line.

The equation that describe the characteristic impedance of a coaxial line is [21]

$$Z_0 = \frac{138}{\sqrt{\epsilon_r}} ln(\frac{B}{b}) \tag{2.48}$$

As the dielectric material thickness ($d$) increases from 0.1 to 1 mm, the characteristic impedance increases, while the diameter of the centre conductor remains constant at $b = 0.6$ mm. As the diameter of the centre conductor increases the characteristic impedance decreases while the dielectric thickness remains constant. This is shown in Fig. 2.16. A coaxial line can be seen as parallel plates, as the height ($d$) between the two plates increases the capacitance decreases. From Eq. 2.12 this results in an increase of characteristic impedance. As the diameter of the coaxial line increases, the total metal surface increases. This can be seen as an increase in the capacitance, from Eq. 2.12 an increase in capacitance leads to a decrease in characteristic impedance.

**(a)** Characteristic impedance vs height ($b = 0.6$ mm).

**(b)** Characteristic impedance vs inner radius ($d = 1$ mm).
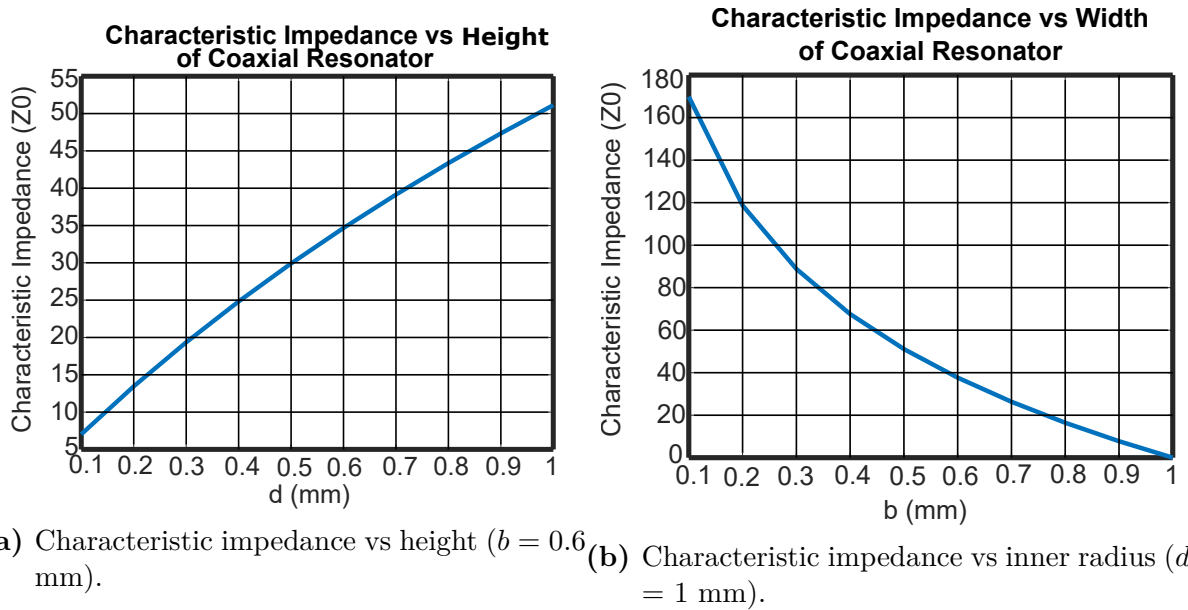
**Figure 2.16:** Characteristic impedance of coaxial line.

#### 2.5.3.1 Q factor and loss

The radius of the inner conductor is varied from 0.6 mm to 2 mm for different dielectric thicknesses ($d$). Again an increase in Q factor is seen as the dielectric thickness is increased. As the dielectric thickness increases the electric field strength decreases, resulting in lower losses.
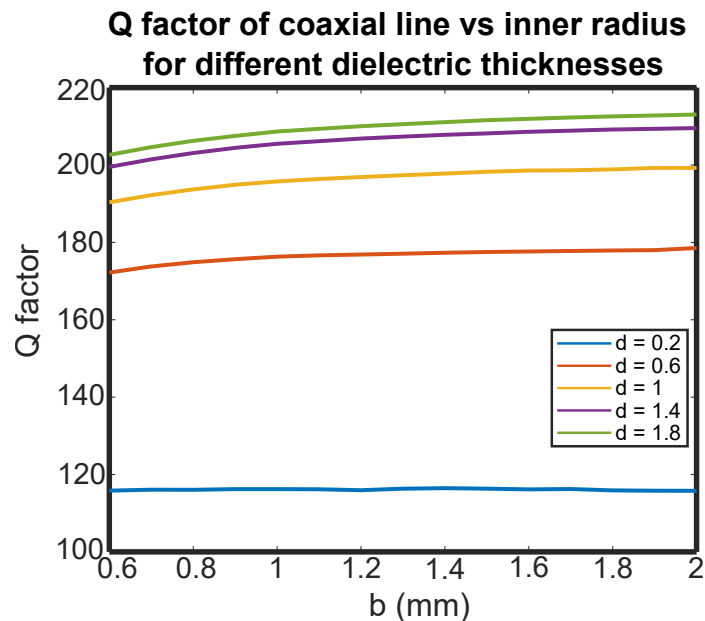


**Figure 2.17:** Q factor of coaxial line vs inner radius for different dielectric thicknesses.

When a coaxial line is shorted at one end it is possible to construct a coaxial resonator with an air dielectric, thus increasing the Q factor significantly. However, an air-dielectric increases the size of the resonator. Coaxial resonators can also be designed to have larger Q factors for the same characteristic impedance as the total size of the resonator

can easily be increased while keeping the characteristic impedance constant. Coaxial resonators can also achieve good coupling as the radius of the inner conductors can be larger in comparison to microstrip line resonators.

### 2.5.4 Ring resonator

Ring resonators are merely transmission lines formed in a closed loop, typically implemented in microstrip or stripline structures. Resonance is established when the mean circumference of the ring resonator is equal to an integral multiple of the guided wavelength. This can be expressed as [29]

$$2\pi r = n\lambda_g \tag{2.49}$$

The guided wavelength can be calculated as

$$\lambda_g = \frac{c}{f\sqrt{\epsilon_e}} \tag{2.50}$$

where $c$ is the speed of light and $\epsilon_e$ is given by Eq. 2.36. One distinct advantage of ring resonators is that there are no open-ended effects as in the case of straight microstrip lines. Disadvantages include larger size [30] and the effect of curvature. The curvature effect cannot be explained by the straight-line approximation shown above. Wolff and Knoppik [31] found that the influence of the curvature becomes large with small line impedances. For small impedance lines the width becomes large and a mean radius is not well defined. If small lines are used the effect becomes even greater due to the increased curvature. Microstrip ring resonators, as seen in Fig. 2.18, are most common in practice. The E-and H-field distribution is similar to straight line microstrip resonators.
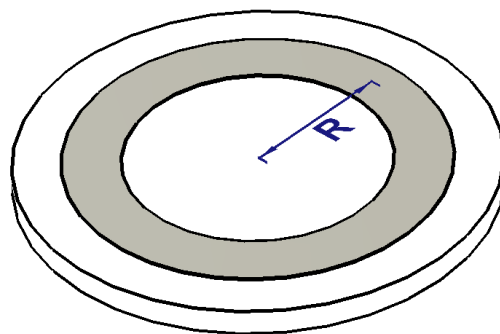


**Figure 2.18:** Microstrip ring Line

The characteristic impedance of a microstrip ring can also be calculated with Eq. 2.42. For a constant line width the height of the dielectric substrate is varied from 0.1 to 1 mm. The characteristic impedance can be seen in Fig. 2.8(a). For a constant substrate height the line width was varied from 0.1 to 1 mm, the characteristic impedance can be seen in Fig. 2.8(b).

### 2.5.4.1   Q factor and loss

As for the microstrip line, the width of the ring resonator line is changed from 0.6 mm to 2 mm for different dielectric thicknesses ($d$) varying from 0.2 mm to 1.8 mm. The same results are seen as for the microstrip line case, the Q factor increases as the dielectric thickness increases, this is for the same reason explained in section 2.5.1.
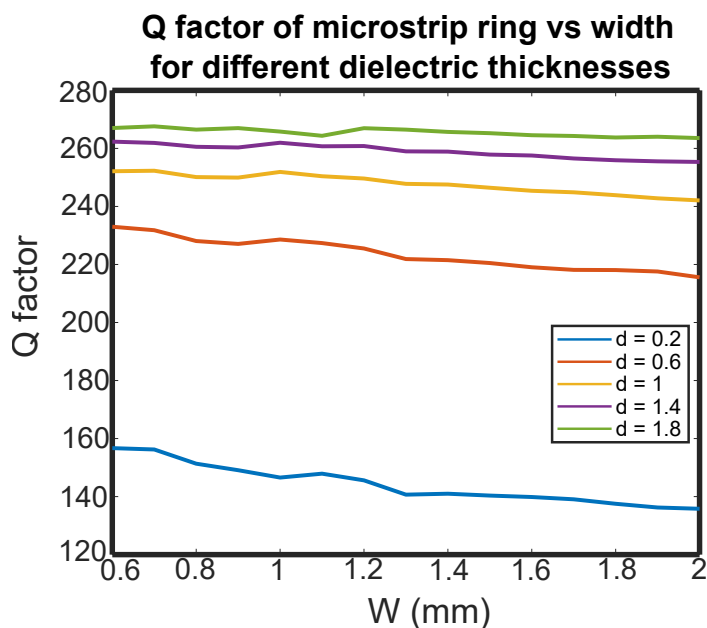


**Figure 2.19:** Q factor of microstrip ring vs width for different dielectric thicknesses.

With the correct dielectric material ring resonators are able to achieve quite high Q factors as in [32]. For a dielectric material with $\tan \delta = 0.001$ a microstrip line with dimensions, $W = 1.85$ mm and $d = 1$ mm, a Q factor of 899 is obtained. The microstrip ring resonator has a higher Q factor than the line resonator because there are no open - ended effects to increase losses and more energy is stored in a ring resonator than in a line resonator.

## 2.5.5   Cavity SIW resonator

As mentioned in the preceding chapter, a two-conductor transmission line can be used to guide Electro Magnetic (EM) energy from one point (generator) to another (load). A waveguide is another means of achieving the same goal. However, a waveguide differs from a two-conductor transmission line in some respect. A transmission line can support a transverse electromagnetic (TEM) wave, whereas a waveguide cannot. At microwave frequencies (roughly 3-300 GHz), planar transmission lines become inefficient due to the skin effect and dielectric losses; waveguides are used to obtain larger bandwidth and lower signal attenuation. Moreover, a transmission line may operate from 0 Hz to a very high frequency; a waveguide can operate only above a certain frequency called the cutoff frequency and therefore acts as a high-pass filter.

Cavity resonators have higher Q-factors and low losses. However, these structures are difficult to integrate with other planar structures and are bulkier. In order to resolve these disadvantages, SIW structures were introduced.  SIW structures retain some of

the advantages that cavity resonators have, such as low loss and high Q factors, electrical shielding and high power handling capabilities. The planar properties of SIW mean smaller size and easier system integration and addition of passive and active components [5]. SIW structures have two conductor plates separated by a dielectric substrate with arrays of via holes connecting the two plates and creating the side walls of the resonator. SIW structures are more easily integrated with other planar structures, have relatively high Q factors, lower losses, and are low in cost. [33]. The SIW cavity resonator can be seen in Fig. 2.20. SIW structures only consist of one conductor thus these strucures can propagate TE modes but not TEM modes [21]. The SIW half-wavelength resonator confines electromagnetic waves, that are reflected back and forth between the boundary walls created by the vias. When a source wave of the specific resonant frequency is applied, the opposing waves form standing waves in which electromagnetic energy is stored.



**Figure 2.20:** SIW cavity.



**(a)** E-field distribution of SIW cavity.
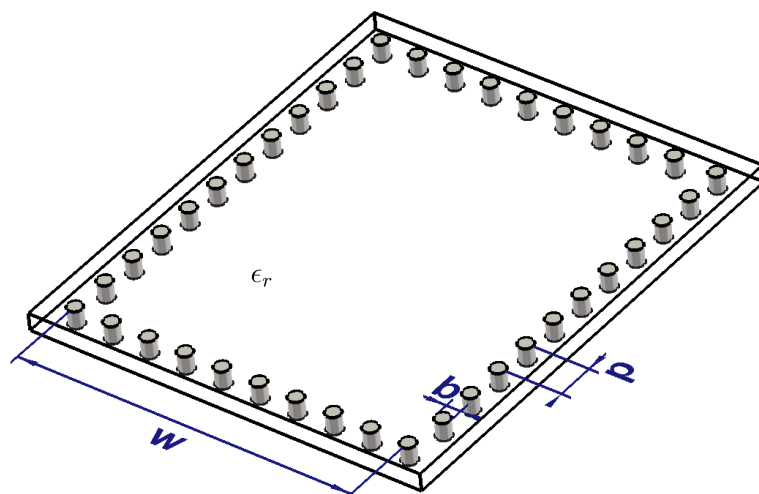


**(b)** H-field distribution of SIW cavity.
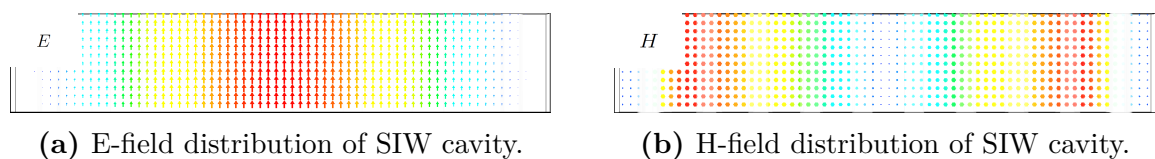
**Figure 2.21:** E and H -field distribution of SIW cavity.

A SIW cavity can be designed using the following relation (the vias are placed a standard distance appart from each other)

$$w_{eff} = w - 1.08\frac{b^2}{p} + 0.1\frac{b^2}{w} \tag{2.51}$$

where $w_{eff}$ is the effective width of the SIW cavity.

The wave impedance of an electromagnetic wave is the ratio of the transverse components of the electric and magnetic fields. The wave impedance is given by [21]

$$Z = \sqrt{\frac{j\omega\mu}{\sigma + j\omega\epsilon}} \tag{2.52}$$

### 2.5.5.1  Q factor and loss

Studies on SIW structures have shown that these structures also have the three main sources of loss as discussed in earlier sections of this chapter namely losses due to finite conductivity, dielectric substrates and leakage [34] [35]. In the case of SIW structures the leakage losses are related to how close the vias are spaced from each other. The spacing and size of the via-holes also directly influence the surface loss. Therefore to minimize this loss, the via-holes need to be less than 0.2 $\lambda$ apart. For the full-wave simulations in CST, the radius of each via is set to 0.2 mm and the distance between the vias are 0.8 mm. The height of the dielectric material is varied from 0.1 to 2 mm. The simulated results for Q factor can be seen in Fig. 2.22.
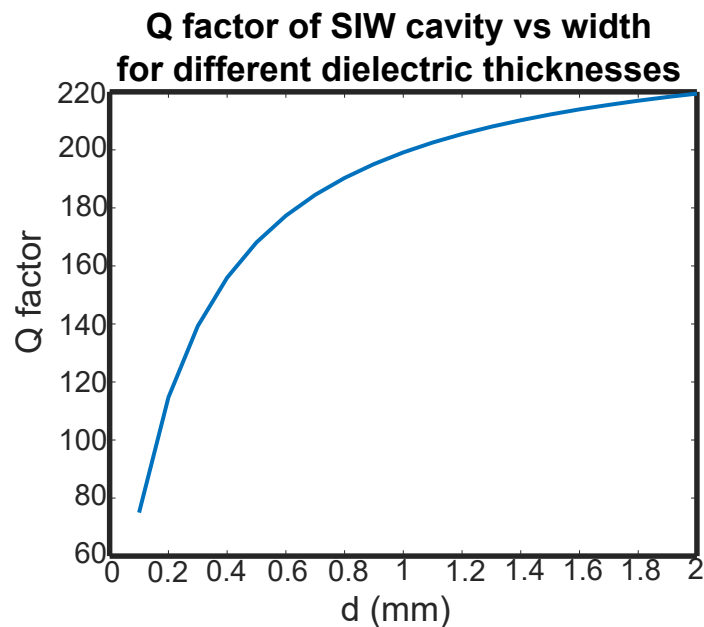


**Figure 2.22:** Q factor of SIW cavity vs height.

The Q factor increases as the height increases and thus the total loss decreases. When comparing the microstrip line to the SIW cavity for a dielectric material with $\tan\delta = 0.004$ it is found that the (enclosed) microstrip line has a higher Q factor than the SIW cavity for the same height. For example, for a height of 1 mm the microstrip line has a Q factor of around 250, while the SIW cavity has a Q factor of around 190. However, when a dielectric material with $\tan\delta = 0.0001$ is used the microstrip line has a Q factor of 1448 and the SIW cavity has a higher Q factor of 1760. Therefore, depending on what material is used, the one is not always better than the other.

## 2.6   Comparison of microwave resonators

In this section the Q factor of the four different line resonators; microstrip line, stripline, coaxial line and microstrip ring; are plotted against their characteristic impedances and

compared to one another. Then the Q factors of the different line resonators are plotted against dielectric thickness ($d$) and compared to one another.

In Fig. 2.23 the Q factor of different line resonators is plotted against characteristic impedances. All the resonators have dielectric thicknesses of 1 mm and the width of the lines are swept from 0.1 mm to 1 mm to change the characteristic impedances. For microstrip and ring, a 5 mm air cavity is used above the substrate, and enclosed by the same metal as the conductor.
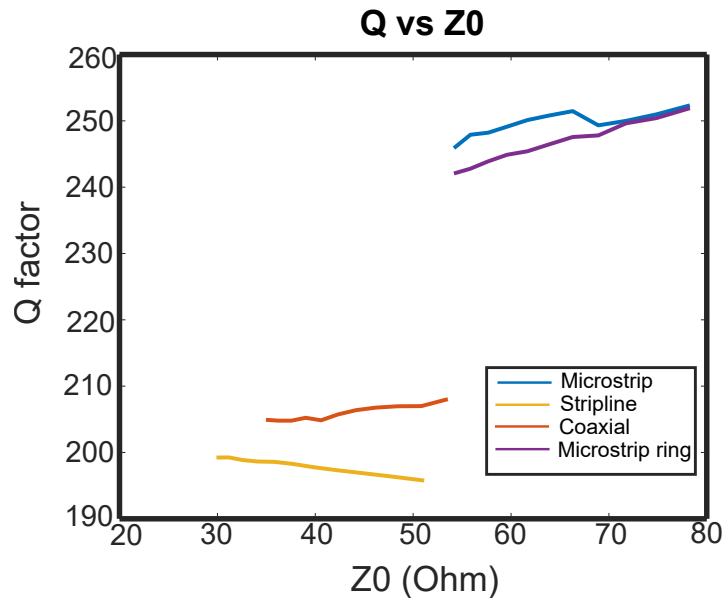


**Figure 2.23:** Q factor vs characteristic impedance for different line resonators.

From the results in Fig. 2.24, it is seen that the microstrip line resonator has the highest Q factor while the stripline line resonator has the lowest Q factor. The microstrip line and ring have similar Q factors, while the coaxial line falls between the microstrip line and stripline line. For the same line widths the microstrip and microstrip ring resonator has higher characteristic impedances than the stripline and coaxial line. The coaxial resonator has higher Q factors in comparison with the stripline resonator. The benefit of coaxial resonators is that these resonators are commonly designed in air, with $\tan \delta = 0$. Coaxial resonators can easily be made larger while maintaining the same characteristic impedance. With the thickness of the dielectric material remaining the same the Q factors is lower. Coaxial resonators are commonly designed using Teflon with a very low $\tan \delta$.

**Q factor vs dielctric thickness for different planar resonators**
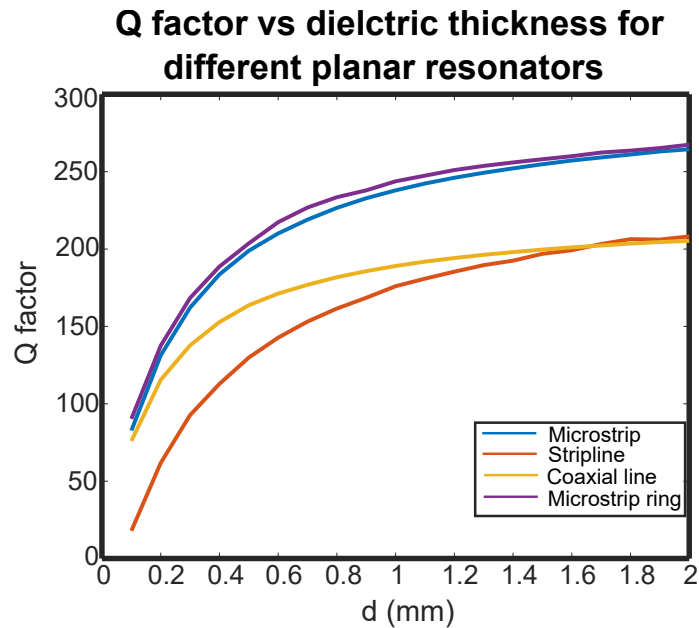
**Figure 2.24:** Q factor vs dielectric thickness for different planar resonators.

## 2.6.1 Discussion

It is commonly said that one topology of resonator is better than the other depending on the application. In this chapter it is seen that this is not always the case when looking at the Q factors and losses of different types of topologies of resonators. For the material used in these simulations (Mercury wave 9350) it is clear that there is no significant difference between the different Q factors. However, when a material with a lower $\tan \delta$ is used and the surface losses begin to play a bigger role in the total losses of the structure a bigger difference in Q factors can be seen.

There are a lot of factors that can influence a designers choice of topology for a resonator or filter depending on what the specifications are. For example, when coupling is the main specification in question, resonators like the coaxial and pedestal resonator are better choices than microstrip or stripline resonators. However, if ease of fabrication, cost or size become bigger factors, microstrip lines might be a better choice.

One advantage of the pedestal resonator is that the designer has more control over the Q factor as the total volume size can be chosen for a certain frequency. If a higher Q factor is needed a bigger structure can be selected for a certain frequency.

# Chapter 3

# Pedestal Substrate Integrated Waveguide resonator and filter

## 3.1 Introduction

Coupled resonator (CR) filters have the advantage of allowing cross-coupling between non-adjacent resonators. With cross-coupling between non-adjacent resonators transmission zeros are introduced increasing selectivity and/or resulting in equalization of the group delay [8],[9], [36], [10]. There are three different types of coupling that can exist between resonators. The cross-coupling can be predominantly capacitive (electric/negative), or inductive (magnetic/positive), or a combination of the two, denoted as mixed coupling. Cavity filters are most often designed with cross-coupling and source-load coupling [8], [37]. Positive coupling is most often used as it is the easiest to implement in cavity filter with simple apertures. Negative coupling is more complicated and difficult to implement, often requiring additional components. However, negative coupling is very common in planar technology. Negative coupling is easily realized with the capacitive coupling between lines.

Implementing both positive and negative coupling simultaneously in any of these classical structures can be difficult. However, this is exactly what is needed when improvements in the stop band and group delay are required. SIW structures offer a solution to this problem. SIW filters can be seen as dielectric filled waveguide filters. Most planar microwave filter topologies naturally accommodate either positive or negative coupling. Inductive aperture coupling is most commonly used to couple adjacent SIW resonators. However, because of the planar etched construction and dielectric material, negative coupling is also easy to implement.

The drawbacks and limitations of most SIW structures are that they are limited in range, require line outside of the structure, or require multi-layered SIW technology. In this section an alternative is proposed to easily realize all types of cross-coupling. The designs proposed cannot be realized without the use of the recently proposed pedestal resonator discussed in section 3.1.1.

In this chapter an in-depth study on coupling mechanisms for the pedestal resonator is done. With these resonators, negative coupling can be realized with an I-shaped etched line on the same plane as the tops of the pedestals. Positive coupling is achieved with

conventional irises between the cavities. Combining these two structures results in mixed coupling. Standard PCB techniques can be used to easily manufacture these structures. The structures are closed and offer a wide range of coupling values. An advantage not investigated in [18] is the possibility for implementing both negative and positive coupling mechanisms in one design. To illustrate the advantage of having both negative and positive coupling in one design, a sixth order filter with transmission zeros for improved selectivity, as well as group delay equalization, is presented. The filter is designed to operate at 5 GHz with a bandwidth of 5% [19].

### 3.1.1   Pedestal resonator

In [18] a novel resonator, denoted as *pedestal resonator*, was introduced to address the problem of spurious responses in SIW waveguides and to reduce resonator size. The work done in [18] is based on ridge waveguides implemented in SIW technology, where a normal ridge guide is formed into a T-ridge guide. These resonators offer many advantages including low cost, lighter weight, circuit miniaturization and electrically closed filters with wide stopbands.

The pedestal topology in [18] is similar to a so-called mushroom topology proposed in 2015 by Tomassoni *et. al* [38], [39], [40]. A mushroom resonator, is composed of a circular patch suspended in a SIW cavity short-circuited by a post in [38] a three-pole filter is presented using dual mode mushroom resonators cascaded through quarter-wave lines. A dual-mushroom resonator consists of two mushroom-shaped metal structures next to each other. With this design it is possible to have transmission zeros introduced in an in-line topology due to the non-resonating nodes creating coupling between non-adjacent resonators.

A pedestal resonator is essentially a loaded SIW resonator, and consists of a metal plate supported by one or multiple vias at a certain height. A side and top view of a typical pedestal SIW resonator is shown in Fig. 3.2(a) and 3.2(b). The field distribution of a pedestal resonator can be seen in Fig. 3.3(a) and 3.3(b). The maximum E-field is found at the top of the pedestal plate, while the maximum H-field is found around the post. With the pedestal resonator a designer has the ability to make an optimal choice between size, unloaded Q, weight, and second resonance spacing [18]. The pedestal resonator in this chapter is defined by the parameters $a$, $b$, $w1$, $w2$, $h1$ and $h2$ shown in Fig. 3.2(a) and 3.2(b)

A basic circuit model for a pedestal resonator can be seen in Fig. 3.1 with a capacitor in parallel with a series resistor and inductor. The capacitance correlates to the parallel plates created by the top wall of the cavity and pedestal plate. The post is then seen as a series resistor and inductor grounded to the bottom wall of the cavity.

**Figure 3.1:** Basic curcuit model of pedestal resonator.



**(a)** Side view of the pedestal SIW resonator.
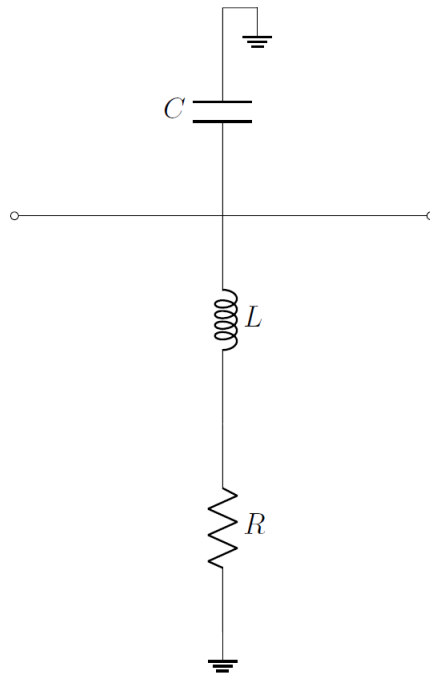


**(b)** Top view of the pedestal SIW resonator.
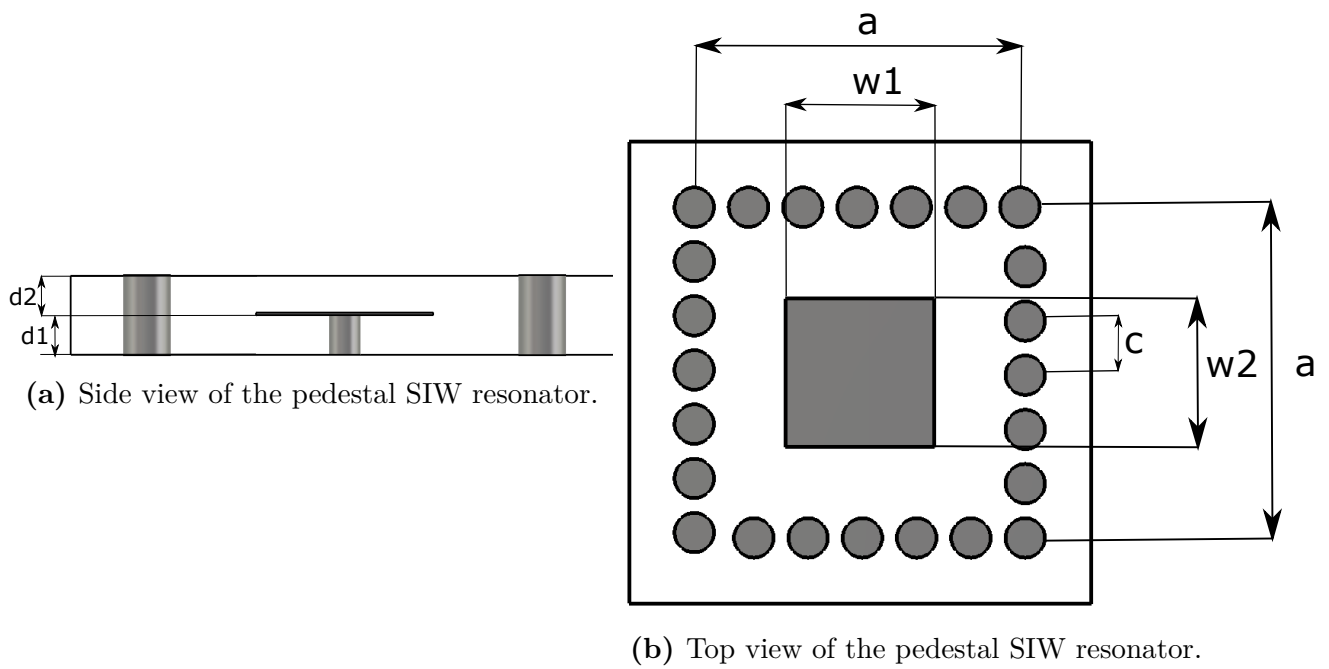
**Figure 3.2:** Top and side view of the pedestal SIW resonator.
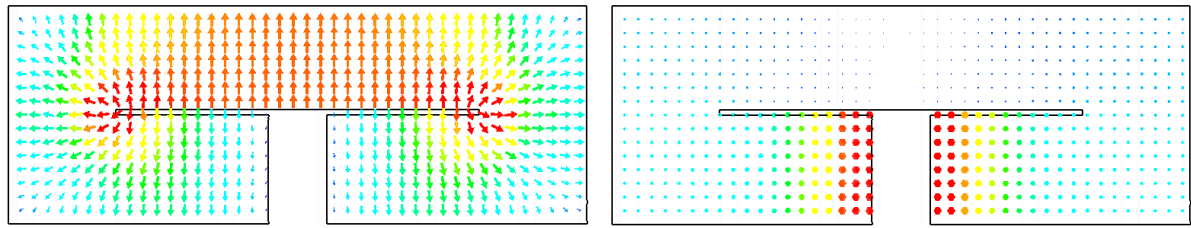
**(a)** Side view of the pedestal SIW resonator E-**(b)** Side view of the pedestal SIW resonator H-
field distribution.                                     field distribution.

**Figure 3.3:** Side view of the pedestal SIW resonator E-and H-filed distribution.

The main characteristics of the pedestal structure can be illustrated by a small parameter study on the height of the substrates and the area of the pedestal, looking at the effect these parameters have on the center frequency and unloaded Q. A resonator is designed with $a = 13$ mm and is simulated using the material Mercurywave 9350 as substrate ($\epsilon_R = 3.5$ and $\tan\delta = 0.004$). To investigate the loading effects of the pedestal on the center frequency, the dimension of the pedestal $w$ is swept over a range of 2 mm to 7 mm, while $d1 = d2$ is kept constant at 1 mm. The center frequency change can be seen in Fig. 3.4(a). As the area of the pedestal is increased, the total capacitance between the pedestal and top layer of the resonator is increased, resulting in a decrease in center frequency.

To investigate the effect of substrate height on the resonant frequency a constant dimension, $w = 4.5$ mm is set, the height of the substrate is varied from $d1 = d2 = 0.4$ mm to 2 mm. The change in resonant frequency can be seen in Fig. 3.4. As the height of the substrate increases the resonant frequency decreases. As the height of the substrate is increased in both layers, the length of he post increases which results in the inductance of the resonator increasing, resulting in a decrease in resonant frequency.
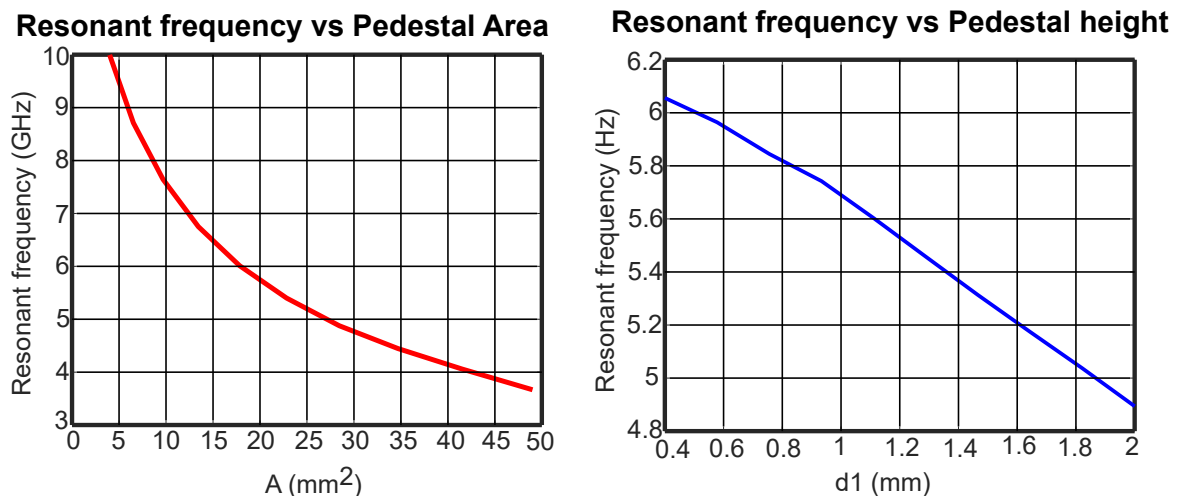


**(a)** Resonant frequency vs pedestal area ($d1 =$**(b)** Resonant frequency vs substrate height ($w$
$d2 = 1$ mm).                                          $= 4.5$ mm).

**Figure 3.4:** Resonant frequency vs substrate height and pedestal width.

When $d1$ is kept constant at $d1 = 1$ mm and $d2$ is swept from 0.4 to 1 mm the resonant frequency of the resonator increases. This is due to the fact that as the top layer height increases the capacitance between the pedestal and top plate decreases. This is seen in Fig. 3.5.



**Figure 3.5:** Resonant frequency vs pedestal height $d2$ ($w = 4.5$ mm).

The change in frequency versus area is much greater than versus height, making $w1$ and $w2$ parameters more suitable for coarse tuning while h1 and h2 are better suited for fine tuning. In general, the smaller $a$ and $b$ are, the higher the frequency of the empty cavity, and the larger the pedestal top needs to be to achieve resonance. This lowers the unloaded Q, but increases the second mode resonance separation [18].

### 3.1.1.1   Q factor and loss
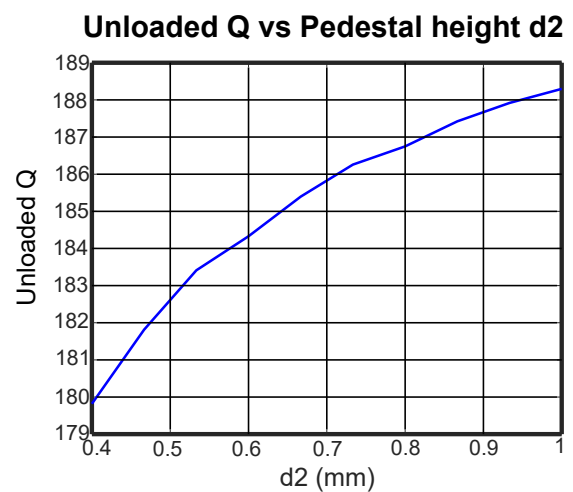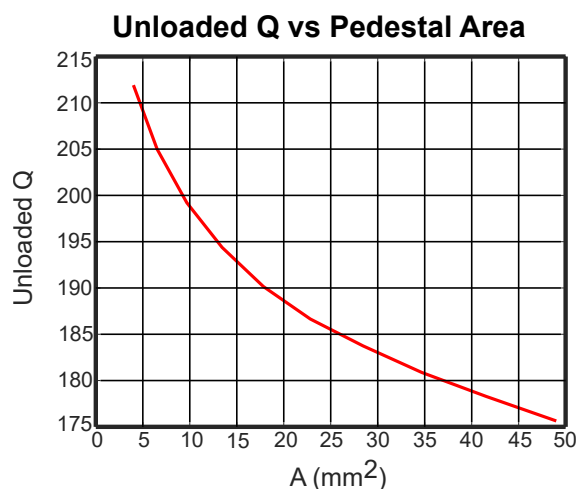


**(a)** Unloaded Q vs pedestal area ($d = 1$ mm).

**(b)** Unloaded Q vs pedestal height $d2$ ($w = 4.5$ mm).

**Figure 3.6:** Unloaded Q vs pedestal area and height $d2$.

From Fig. 3.6(a) and 3.6(b) it is seen that as the area of the pedestal is increased the unloaded Q factor decreases. As the top layer height increases the unloaded Q factor increases.

An SIW cavity loaded with a pedestal is simulated. The pedestal area is varied from 0 mm$^2$, representing no loading to the SIW cavity, to 196 mm$^2$ for different dielectric thicknesses, while the total cavity size remains constant at 26 mm x 26 mm. With these simulations the center frequency is not kept constant i.e. each Q-value is calculated at a different frequency. From the results it is clear that as the area of the pedestal increases the Q factor decreases. This is because as the area of the pedestal increases, the loading on the SIW cavity increases, increasing the total losses. The Q factor increases as the dielectric thickness decreases. As the dielectric thickness decreases more energy can be stored between the pedestal plate and top plate of the resonator resulting in a higher Q factor.
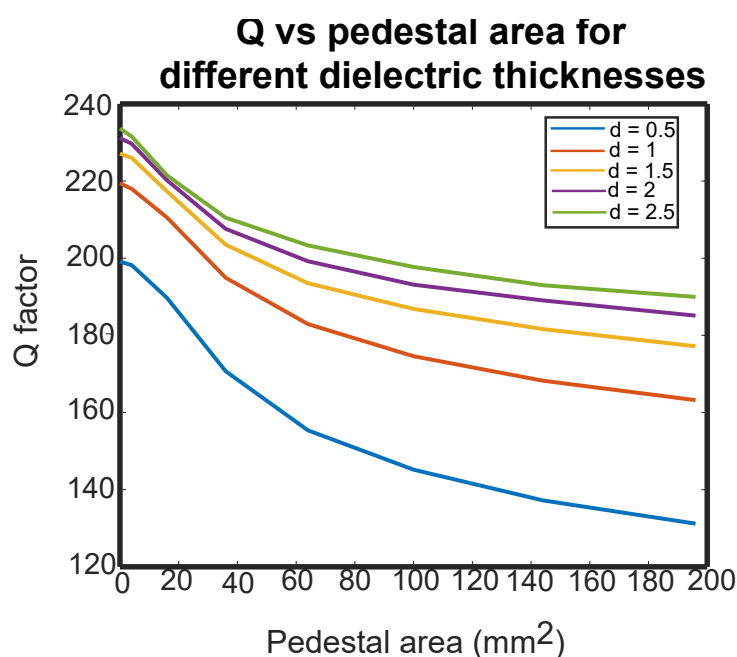


**Figure 3.7:** Q vs pedestal area for different dielectric thicknesses.

A benefit of the pedestal resonator is that the designer has more control over the Q factor when designing. If a larger Q factor is required for a certain frequency the SIW cavity can be chosen as being bigger with a corresponding loading to match the center frequency.

## 3.2 Coupling mechanisims

In certain types of structures transmission zeros at real frequencies are created with positive (or magnetic) cross-coupling between resonators to improve selectivity, while transmission zeros at imaginary frequencies are created with negative (or electric) cross-coupling between resonators to equalize group delay and reduce phase distortion. To achieve both of these advantages, transmission zeros at both real and imaginary frequencies are required. Thus both positive and negative cross-couplings are required, in addition to in-line couplings of typically one sign throughout.

In [41] and [42] the SIW resonators are folded vertically and slots are etched to create coupling windows at specific locations to couple electric fields. A fourth order multilayer partial H-plane folded-SIW filter at 10 GHz, proposed in [43], and another multilayer filter at 13 GHz, proposed in [42] are good examples of this method. In both [42] and [43] the aim is to suppress higher order modes by implementing magnetic, electric and mixed coupling. In [8] a fourth order in-line SIW filter is proposed where the four in-line SIW cavities are coupled magnetically with conventional irises and the first and fourth cavity is coupled electrically with a microstrip transmission line inverter.

Mixed coupling has also been demonstrated in coaxial waveguide structures. In [9] and [44] coupling strips or probes are used to achieve coupling. A third-order in-line coaxial filter with both electrical and magnetic mixed coupling is presented in [9]. Magnetic coupling is achieved with a coupling pin that connects to the inner rods of each coaxial resonator through a metallic gap and electric coupling is achieved by inserting a microstrip line between the coupling irises that connects the metallic caps at the open-end of both inner rods.

In [37] different types of coupling is used in a comb line SIW filter. In this example coupling is achieved with an open-ended coplanar transmission line between comb-line SIW resonators. Metallic posts are used to realize magnetic coupling and a metallic disk with an airgap between the disk and the top metal layer is used to realize electric coupling. This method can also be used to realize mixed coupling. In [45] an iris-based coupling is combined with a grounded coplanar-line etched on the top metal layer between the resonators to achieve mixed coupling.

In [46] a similar approach is used where a fourth order cross-coupled elliptic filter with mixed coupling is proposed. Both magnetic and electric coupling is created with a structure consisting of two layers. Electric coupling is achieved with an embedded stripline, while magnetic coupling is achieved with a conventional iris. Combining these two structures results in the realization of mixed coupling. In [47] mixed coupling is achieved with conventional irises and a grounded microstrip line.

The pedestal SIW resonator naturally allows for positive in-line couplings, and both positive and negative cross-couplings enclosed in the structure. Input and output couplings are also easily achieved using coplanar-line and a grounded via. A wide range of values can be achieved with this design.

### 3.2.1 Input-output coupling

The loaded Q of the first and last resonator of coupled-resonator filters defines the input and output couplings respectively. For wider bandwidth filters, the loaded Q needs to be lower. With this structure it is clear from Fig. 3.3(b) that high magnetic coupling can easily be achieved with a grounded via running through a hole in the pedestal. Therefore the input and output coupling consists of a 50 $\Omega$ coplanar line in the top ground plane of the structure and a grounded via. The coupling structure is shown in Fig. 3.8(a). Note that in the figure, the top ground plane is removed for clarity, with only the center conductor of the coplanar line visible. The magnetic field around the pedestal base couples with the magnetic field around the input via.
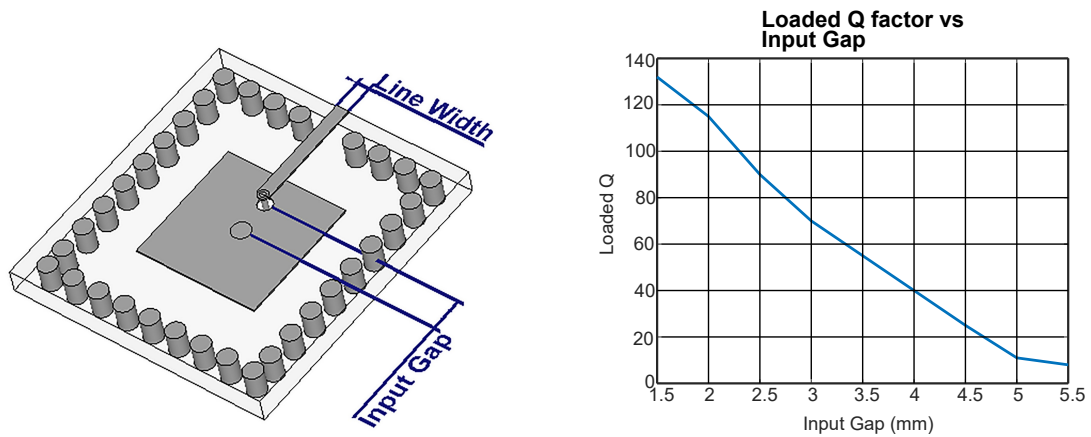
**(a)** Input/Output coupling of the pedestal SIW resonator

**(b)** Input/Output loaded Q values vs $InputGap$ ($LineWidth = 0.53$ mm).

**Figure 3.8:** Input/Output coupling of the pedestal SIW resonator and Output loaded Q values.

A large range of coupling values can be obtained by controlling the separation between the input via and the post of the pedestal. The calculated results can be seen in Fig. 3.8(b) where the loaded Q is plotted against the distance between the input via and pedestal post for a structure with the following dimensions $a = 10$ mm, $w = 4.5$ mm, $c = 1.6$ mm and $Linewidth = 1.2$ mm . As the distance decreases, the coupling increases, and the loaded Q, increases. It is clear that a wide range of values is obtained, corresponding to filter bandwidths ranging from below 1% to almost 13%. In comparison to [37] where a 1.14 - 7.14 % bandwidth range is shown, a wider range is achieved with the presented structure.

## 3.2.2 Positive coupling

The pedestal resonator can also be seen as a loaded SIW waveguide, thus positive (magnetic) inter-resonator coupling can be realised in the same way as for normal waveguides , i.e. using conventional inductive irises. In Fig. 3.9(a) two identical pedestal resonators is separated by a via wall. An aperture is formed by simply removing vias to effect magnetic coupling. The positive (magnetic) coupling coefficient is controlled by both the width of the aperture, and the spacing of the pedestal. The positive (magnetic) coupling coefficient is calculated using the standard two-frequency method for identical resonators [21].

$$k = \frac{f_1^2 - f_2^2}{f_1^2 + f_2^2} \qquad (3.1)$$

where k is the coupling coefficient, while f1 and f2 correspond to the even and odd mode resonant frequencies.

The positive coupling coefficient is plotted against the gap width ($GapW$) for various pedestal spacings ($d$) in Fig. 3.9(b). The range of coupling values are seen to be large for this type of coupling, as with standard waveguides. As the $GapW$ is widened the positive

coupling increases as more of the magnetic fields are able to couple with each other. As the spacing $d$ between the pedestals increase the coupling decreases. This is due to the fact that as the spacing increases the maximum of each magnetic field is moved further away from each other, thus smaller magnetic fields are coupling. Compared to normal SIW, this effect introduces a very useful extra parameter to control coupling. A closed wall represents zero coupling, while no wall represents total or direct coupling. With these results shown in Fig. 3.9(b), filter bandwidths ranging from zero to almost 10% is possible.
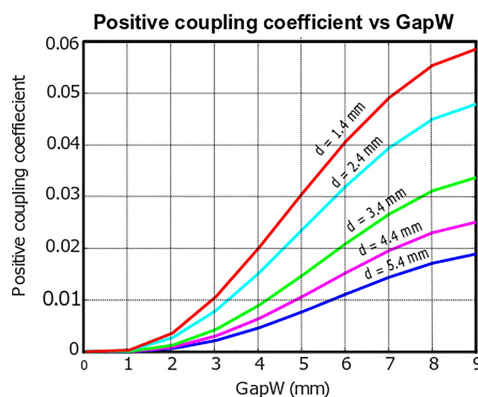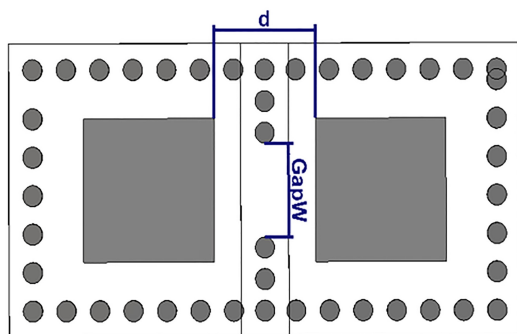


**(a)** Top view of the positive coupling structure for the pedestal SIW resonator.

**(b)** Positive coupling coefficient vs Gap width ($GapW$) for different pedestal spacings ($d$).

**Figure 3.9:** Top view of the positive coupling structure for the pedestal SIW resonator and Positive coupling coefficient vs Gap width ($GapW$)

## 3.2.3   Negative coupling

To create negative or electric coupling in standard SIW, the electric field in the guide has to be probed. For SIW structures, this is not as straight forward as for positive or magnetic coupling. One popular approach, is to couple the electric field by folding a filter in the vertical direction and etching slots at specific locations in the separating plate [41], [42]. A drawback to this approach is complex manufacturing with multilayered structures. Planar lines have also been used to achieve coupling as in [8], where microstrip transmission line inverters are used to couple the first and fourth cavities electrically. In [47] a shorted microstrip line is used to achieve electrical coupling. Coplanar-lines have also been used as in [45], where the electrical component of a mixed coupling scheme is achieved with a grounded coplanar-line etched at the top of the resonators. In [48] electric coupling is realised with a metallic disk etched on the top layer of the structure. With these planar line approaches however the structure is not a closed structure, resulting in possible energy loss. A solution to this problem can be found in [46] where an embedded strip line is used in a multilayered structure to create electrical coupling, but at the cost of additional complexity.

From Fig. 3.2(a) it is clear that the pedestal structure offers a variety of options to probe the electric field through simple capacitive coupling. A simple coupling structure can easily be etched in the same way as the pedestal top. Due to the placement, from Fig. 3.3(a), it is clear that the E-field distribution will not be disturbed. One of the simplest options is a coupling structure consisting of an I-shaped stripline, which is placed between

the resonators on the same layer as the pedestal tops. The top view of this coupling structure can be seen in Fig. 3.10(a). The coupling coefficient is calculated using Eq. 3.1. The negative coupling coefficient is plotted against the coupling gap ($Gap1$) for various strip widths ($StripW$), the results are shown in Fig. 3.10(b). As the gap decreases, or the strip width increases, the electric coupling coefficient increases. Again, a wide range of coupling values is achieved. As $Gap1$ increases, the capacitance between the plate and the strip decreases, resulting in smaller coupling values. As the strip width increases, the capacitance between the strip and the pedestal plate increases, resulting in an increase in electric coupling. It should be noted that this type of coupling in filters are normally very small, and the achieved values are sufficient for most applications.



**(a)** Top view of the negative coupling structure for the pedestal SIW resonator.

**(b)** Negative coupling coefficient vs Gap width ($Gap1$) for different strip widths ($StripW$).

**Figure 3.10:** Top view of the negative coupling structure for the pedestal SIW resonator and Negative coupling coefficient vs Gap width ($Gap1$).

## 3.2.4 Mixed coupling

In Fig. 3.11(a) it is shown that the two coupling mechanisms presented here can easily be combined to create mixed coupling. By simply changing the gap size, the coupling can be changed from negative to positive. Electric and magnetic coupling are added to give the total mixed coupling. The wider the $GapW$ the more magnetic fields are able to couple, resulting in the total coupling to be more positive. As $Gap1$ increases the electric coupling component decreases (as explained in section 3.2.3), resulting in the total mixed coupling to increase and become more positive (magnetic). As the $GapW$ increases the magnetic coupling increases (as explained in section 3.2.2), resulting in the total mixed coupling to increase. A wide range of coupling values can be seen in Fig. 3.11(b). The coupling values obtained with this structure is similar to most coupling structures, but is able to obtain a larger range of values in comparison to structures such as in [45].
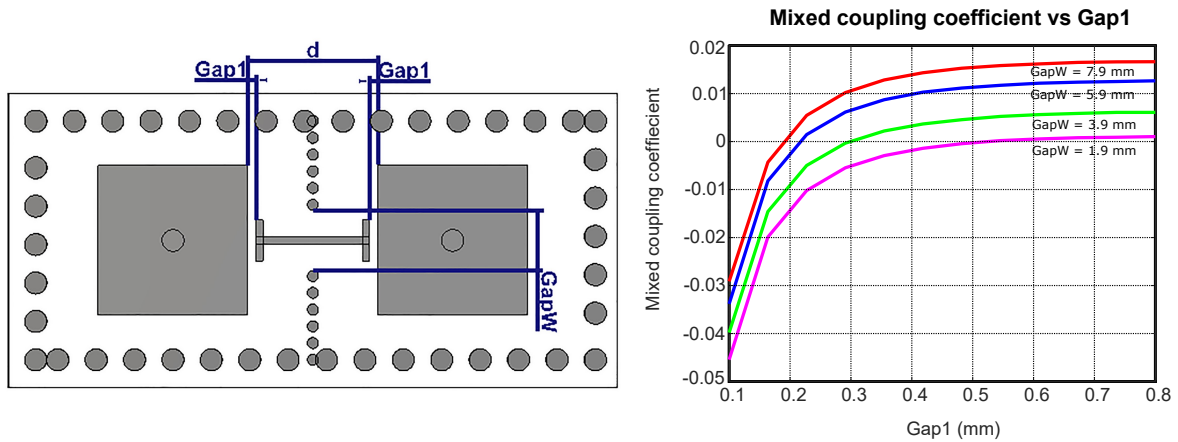
**(a)** Top view of the mixed coupling structure for the pedestal SIW resonator. **(b)** Mixed coupling coefficient vs Gap width ($Gap1$) for different gap widths ($GapW$).
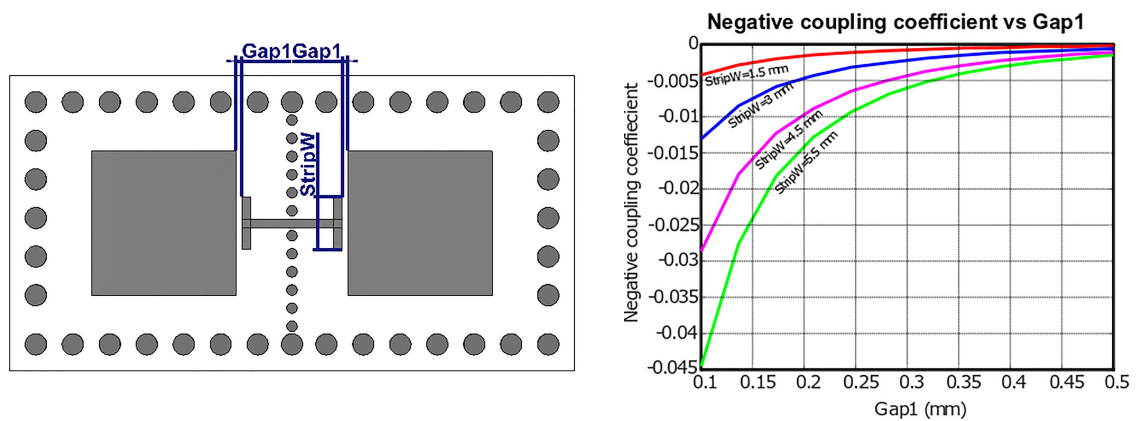
**Figure 3.11:** Top view of the mixed coupling structure for the pedestal SIW resonator and Mixed coupling coefficient vs Gap width ($Gap1$).

## 3.3 Filter design

A sixth-order bandpass filter is designed to demonstrate the implementation of different cross-coupling types to couple pedestal resonators, a sixth-order pedestal SIW bandpass filter is designed, simulated and manufactured. The filter is designed for WiFi-band, with a centre frequency at 5 GHz and a bandwidth of 5%. A sixth order low-pass response is used with an added transmission zero pair at a real frequency and another at an imaginary frequency. The transmission zero pair at the real frequency is added to improve selectivity, while the transmission zero pair at the imaginary frequency is added to optimize the phase response. Fig. 3.12 shows the coupling scheme to be implemented with this design. The solid lines indicates magnetic coupling, while the dashed line indicates electric coupling.
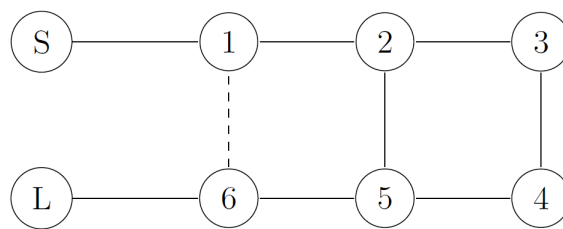


**Figure 3.12:** Coupling scheme of 6th-order filter.

Classical synthesis procedures are used to derive a coupling matrix for the pedestal filter from theory presented in [49] and [50]. The specifications for the filter are as follows: 6-th order, 20 dB return loss, Chebychev band-pass response, with transmission zeros at $\pm$ j1.81, $\pm$ 1.15, 0 and $\infty$. With the specified transmission zeros the transfer and reflection functions can be expressed as

$$S_{11} = \frac{F(\omega)/\epsilon_R}{E(\omega)} \qquad (3.2)$$

$$S_{21} = \frac{P(\omega)/\epsilon}{E(\omega)} \tag{3.3}$$

$$\epsilon = \frac{1}{\sqrt{10^{RL/10} - 1}} \left| \frac{P(\omega)}{F(\omega)/\epsilon_R} \right|_{\omega = \pm 1} \tag{3.4}$$

RL is the return loss in dB. The polynomial $P(\omega)$ is calculated using the transmission zeros as $P(\omega) = \prod_{n=1}^{n_z}(\omega - \omega_n)$, while the polynomials $F(\omega)$ en $E(\omega)$ can be obtained with the recursive technique from

$$G_N(\omega) = U_N(\omega) + V_N(\omega) \tag{3.5}$$

where

$$G_N(\omega) = \prod_{n=1}^{N} \left[ \left( \omega - \frac{1}{\omega_n} \right) + \omega' \sqrt{\left( 1 - \frac{1}{\omega_n^2} \right)} \right] \tag{3.6}$$

At the end of the recursive technique $G_6(\omega) = U_6(\omega) + V_6(\omega)$ is obtained, where $U_6(\omega)$ correlates to the normalized $F(\omega)$ polynomial. Along with the prescribed $P(\omega)/\epsilon$ polynomial, the $E(\omega)$ polynomial can be calculated using the alternating singularity principle [20]. The s-plane positions of the zeros and poles can be seen in Table 3.1 with the corresponding polynomials in Table 3.2. This combination of transmission zeros allow for good selectivity combined with optimum phase linearity.

| | Reflection zeros (Roots of $U_6(s) = F_6(s)$) | Transmission zeros (specified) | Transmission/ Reflection poles (Roots of $E_6(s)$) | In - Band reflection maxima (roots of $V_6(s)$) |
|---|---|---|---|---|
| 1 | - 1.0315j | 1.15 | -1.0738 + 0.0859j | -0.9517j |
| 2 | 0.9862j | -1.15 | -1.0570 - 0.1015j | 0.9139j |
| 3 | 0.7358j | 1.81j | -0.7529 + 0.2733j | 0.4293j |
| 4 | - 0.6445j | -1.81j | -0.7193 - 0.2736j | -0.1595 - 0.1958j |
| 5 | -0.1472 - 0.0230j | $-\infty$ | -0.2186 + 0.4109j | 0.1595 - 0.1958j |
| 6 | 0.1472 - 0.0230j | $\infty$ | -0.2018 - 0.3949j | |
| | $\epsilon_R = 1.00056111$ $\epsilon = 29.86536185$ | | | |

**Table 3.1:** The s-plane coordinates of the zeros and poles

The next step is to formulate the admittance function $[Y_N]$ from the transfer and reflection polynomials. In a doubly terminated network with source and load terminations of $1\,\Omega$, the equations for an even order filter for $y_{21}(s)$ and $y_{22}(s)$ are

$$y_{21}(s) = \frac{P(s)/\epsilon}{m_1(s)} \tag{3.7}$$

$$y_{22}(s) = \frac{n_1(s)}{m_1(s)} \tag{3.8}$$

|   | $E(s)$ | $F(s)$ | $P(s)$ |
|---|--------|--------|--------|
| 0 | 0.1454 + 0.0069j | -0.0107 | -4.33264j |
| 1 | 0.9149 + 0.0199j | 0.0238j | |
| 2 | 2.9760 + 0.0251j | 0.4525 | -1.9536j |
| 3 | 5.8000 + 0.0155j | -0.0015j | |
| 4 | 6.6184 + 0.0037j | 1.4755 | 1j |
| 5 | 4.0234 - 0.0001j | | |
| 6 | 1 | 1 | |

**Table 3.2:** The $E(s)$, $F(s)$, $P(s)$ polynomial coefficients.

where $n_1(s)$ and $m_1(s)$ are given as

$$m_1(s) = \mathrm{Re}(e_0 + f_0) + j\mathrm{Im}(e_1 + f_1)s + \mathrm{Re}(e_2 + f_2)s^2 + j\mathrm{Im}(e_3 + f_3)s^3 \\ + \mathrm{Re}(e_4 + f_4)s^4 + j\mathrm{Im}(e_5 + f_5)s^5 + \mathrm{Re}(e_6 + f_6)s^6 \quad (3.9)$$

$$n_1(s) = j\mathrm{Im}(e_0 + f_0) + \mathrm{Re}(e_1 + f_1)s + j\mathrm{Im}(e_2 + f_2)s^2 + \mathrm{Re}(e_3 + f_3)s^3 + j\mathrm{Im}(e_4 + \\ f_4)s^4 + \mathrm{Re}(e_5 + f_5)s^5 + j\mathrm{Im}(e_6 + f_6)s^6 \quad (3.10)$$

The following results are obtained

$$m_1(s) = s^6 - 0.00005js^5 + 4.04695x^4 + 0.007js^3 + 1.71425s^2 + 0.02185js + 0.06735$$

$$n_1 = 2.0117s^5 + 0.00185js^4 + 2.9s^3 + 0.01255js^2 + 0.45745 + 0.00345j$$

Note that the $e_i$ and $f_i$ are the complex coefficients of $E(s)$ and $F(s)/\epsilon_R$ respectively. The residues of $y_{21}(s)$ and $y_{22}(s)$ can be found with partial fraction expansion because the denominator and numerator polynomials are known. The real eigenvalues $\lambda_k$ can also be found by calculating the root values of the denominator polynomial $m_1(s)$. With this information for the overall network $[Y_N]$ can be expressed as

$$[Y_N] = j \begin{bmatrix} 0 & K_\infty \\ K_\infty & 0 \end{bmatrix} + \sum_{k=1}^{N} \frac{1}{s - j\lambda_k} \begin{bmatrix} r_{11k} & r_{12k} \\ r_{21k} & r_{22k} \end{bmatrix} \quad (3.11)$$

When the number of finite transmission zeros $n_{zf}$ is equal to the order of the filter, the network is considered fully canonical. In this case, $K_\infty$ is extracted from $y_{21}(s)$, and it is also necessary to multiply $P(s)$ with j to ensure that the scattering matrix adheres to the

unitarity conditions. To extract $K_\infty$, it is evaluated at $s = j\infty$.

$$jK_\infty = \left.\frac{jP(s)/\epsilon}{y_d(s)}\right|_{s=j\infty} \tag{3.12}$$

$$K_\infty = 0.0167418$$

The fully canonical equivalent circuit can be modeled as six complex resonators separated by K- inverters (or J inverters) as in Fig. 3.13.
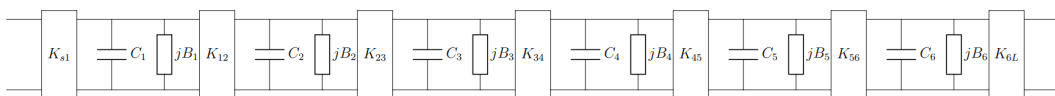


**Figure 3.13:** Fully canonical equivalent circuit.

$[Y_N]$ can also be written as

$$[Y_N] = j\begin{bmatrix} 0 & M_{SL} \\ M_{SL} & 0 \end{bmatrix} + \sum_{k=1}^{N}\frac{1}{sC_k + jB_k}\begin{bmatrix} M_{Sk}^2 & M_{Sk}M_{Lk} \\ M_{Sk}M_{Lk} & M_{Lk}^2 \end{bmatrix} \tag{3.13}$$

Here $M$ and $K$ is interchangeable. Then the $M$ values can be obtained from

$$\frac{r_{21k}}{s - j\lambda_k} = \frac{M_{Sk}M_{Lk}}{sC_k + jB_k} \tag{3.14}$$

$$\frac{r_{22k}}{s - j\lambda_k} = \frac{M_{Lk}^2}{sC_k + jB_k} \tag{3.15}$$

By equating the real and imaginary parts, the following relationships hold and the circuit parameters can be given as

$$
\begin{aligned}
C_k &= 1, \\
B_k &= M_{kk} = -\lambda_k, \\
M_{Lk}^2 &= r_{22k}, \\
M_{sk} M_{Lk} &= r_{21k}, \\
M_{Lk} &= \sqrt{r_{22k}} = T_{Nk}, \\
M_{Sk} &= r_{21k}/\sqrt{r_{22k}} = T_{1k}, k = 1, 2, 3, 4, 5, 6.
\end{aligned}
\tag{3.16}
$$

$T_{Nk}$ and $T_{1k}$ being the eigenvectors. The eigenvalues, residues and eigenvectors is summarised in Table 3.3.

| k | $\lambda_k$ | $r_{22k}$ | $r_{21k}$ | $T_{Nk}$ | $T_{1k}$ |
|---|---|---|---|---|---|
| 1 | -1.89023 | 0.7106 | -0.0697 | 0.8429 | -0.2640 |
| 2 | +1.8898 | 0.7120 | 0.0700 | 0.8438 | 0.2645 |
| 3 | 0.6679 | 0.1710 | 0.0786 | 0.4135 | 0.2803 |
| 4 | -0.6442 | 0.1734 | -0.0946 | 0.4164 | -0.3075 |
| 5 | -0.2212 | 0.1224 | 0.2705 | 0.3498 | 0.5201 |
| 6 | 0.1981 | 0.1222 | -0.2548 | 0.3495 | 0.5047 |

**Table 3.3:** Eigenvalues, residues and eigenvectors values.

The last step is to obtain the folded coupling matrix for the coupling scheme shown in Fig. 3.12. Setting the input and output impedance values to 1.0049 $\Omega$, the resulting normalized folded coupling matrix is then calculated as

$$
\begin{bmatrix}
0 & 0.843 & 0 & 0 & 0 & -0.0314 \\
0.843 & 0 & 0.6102 & 0 & 0.0394 & 0 \\
0 & 0.6102 & 0 & 0.5628 & 0 & 0 \\
0 & 0 & 0.5628 & 0 & 0.6102 & 0 \\
0 & 0.0394 & 0 & 0.6102 & 0 & 0.8430 \\
-0.0314 & 0 & 0 & 0 & 0.8430 & 0
\end{bmatrix}
\tag{3.17}
$$

showing all positive in-line couplings, and both positive and negative cross-couplings.

The filter stack-up consists of two Mercurywave 9350 cores ($\epsilon_r$= 3.5, $\tan\delta = 0.004$ at 10 GHz) of thickness = 0.508 mm each. The two cores are bonded with a single layer of Mercurywave 1080 prepreg ( $Er$= 3.5) of thickness = 0.076 mm, as shown in Fig. 3.15(a). The pedestal plate is then etched on one of these core substrates with a blind via forming the pedestal base. Vias through both of the Mercurywave cores are used as the walls of the SIW guide.

The dimensions of the pedestal resonator used in the filter design presented are shown in Table 3.4. The resonator is designed to operate at 5 GHz. The vias are placed a standard distance appart from each other.

| Dimension name | Value (mm) |
|:---:|:---:|
| $a$ | 10.26 |
| $b1$ | 9.54 |
| $b2$ | 10.93 |
| $b3$ | 10.06 |
| $c$ | 1.35 |
| $w1$ | 6.12 |
| $w2$ | 5.92 |
| $w3$ | 5.89 |
| $w4$ | 4.82 |
| $w5$ | 4.85 |
| $w6$ | 4.67 |
| $g$ | 3.35 |
| $h$ | 1.73 |
| $LineWidth$ | 0.56 |
| $ViaR$ | 0.4 |

**Table 3.4:** Dimensions of 6-th order pedestal filter.
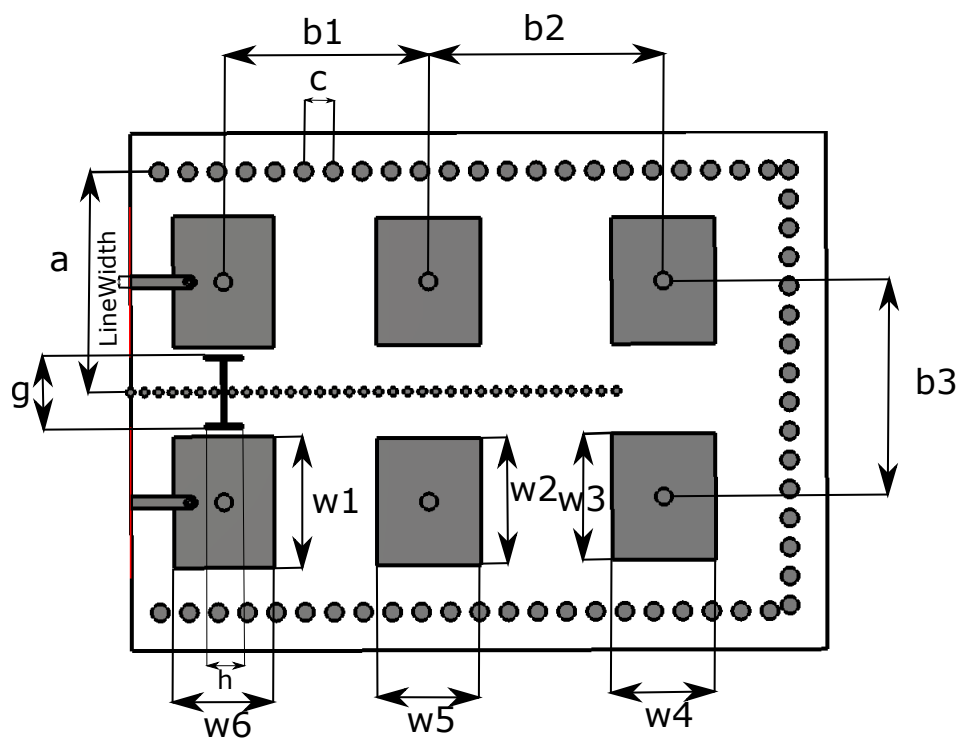


**Figure 3.14:** Internal view of Sixth-order Pedestal SIW Filter with Electrical and Magnetic cross-coupling.

Using the coupling methods described in section 3.2 the final filter design in Fig. 3.15(a) and Fig. 3.15(b) is obtained.
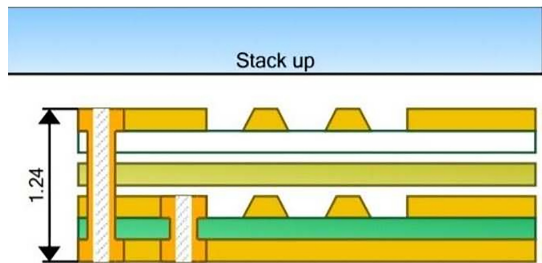
(a) Filter stack-up.
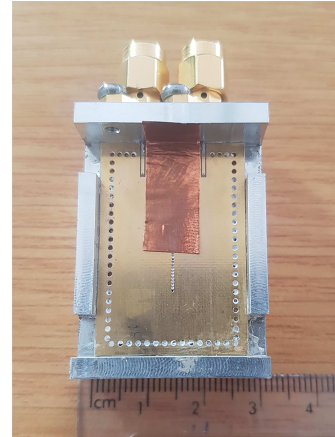


(b) Fabricated 6th order SIW pedestal filter fabricated filter.

**Figure 3.15:** Filter stack-up and image of the fabricated filter

## 3.4 Simulated and measured results

A Keysight PNA-X network analyser is used to do the measurements of the filter. During the measurement process copper tape is added to minimize coupling between the input and output coaxial connectors. The measured results can be seen in Fig. 3.16 to 3.18. A frequency shift of 0.22 GHz is observed with a slight increase in bandwidth. This is due to the difference in thickness of the manufactured filter's upper substrate layer from that originally specified (shown in Fig. 3.15(a). For adequate comparison of the manufactured versus simulated results, the upper substrate layer thickness is increased by 0.1 mm in simulation.
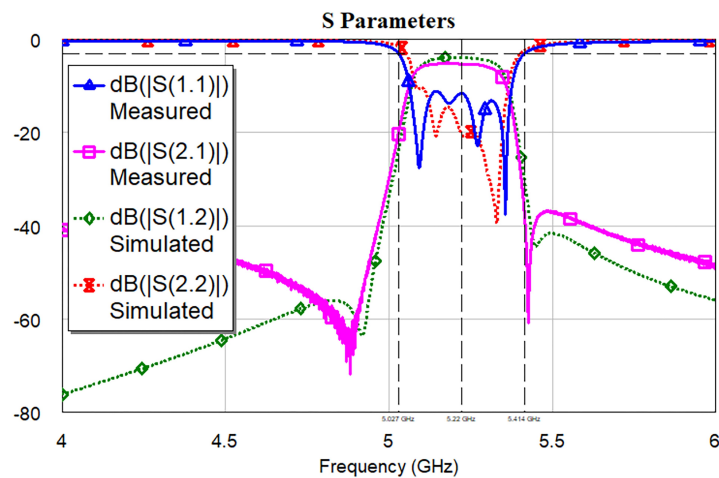


**Figure 3.16:** Simulated vs Measured S Parameters.
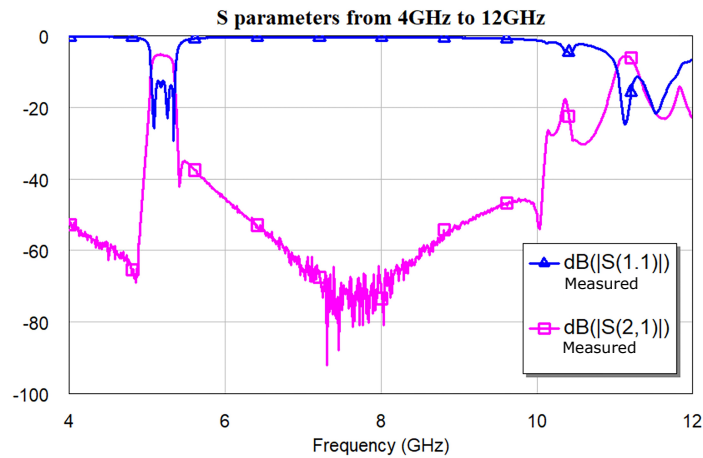
**Figure 3.17:** Measured wide band frequency response.
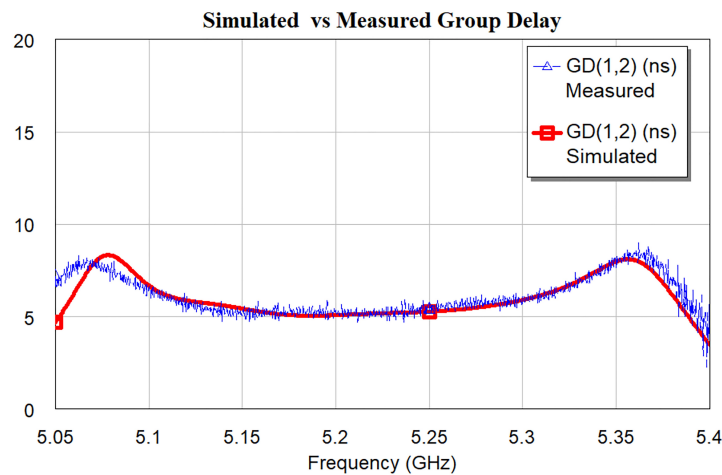


**Figure 3.18:** Simulated vs measured group delay.

Good agreement between the simulated and measured results are obtained for both the amplitude and group delay responses except for the low-frequency band region. From the flat response in the group delay, and transmission zero in the stopband, it is clear that both the real and imaginary transmission zeros are implemented correctly, therefore both positive and negative cross-couplings are demonstrated. All the in-line couplings are accurately implemented due to the good correspondence of the bandwidths shown, while good return loss agreement show that the input and output couplings are also implemented correctly. A small increase in insertion loss is seen because during the simulation process ideal conductivity of copper is used and no surface roughness is taken into account.

In the lower stopband signifiant differences can be seen due to coupling between the coplanar feed lines on the top of the substrate. This can be reduced by improving the isolation between the feed lines, using physical shielding, or redesigning the input and output lines to be at the sides of the filter as in [18]. The measured, simulated and ideal results are summarized in Table 3.5.

|  | f0 (GHz) | 3dB BW | S11 @ f0 | S21 @ f0 | GD @ f0 |
|---|---|---|---|---|---|
| Measured | 5.22 | 7.66 % | -11.11 dB | -5.039 dB | 5 ns |
| Simulated | 5.22 | 6.97 % | -10.45 dB | -3.856 dB | 5 ns |
| Theoretical | 5 | 5 % | -20 dB | -5 dB | 5 ns |

**Table 3.5:** Measured, simulated and theoretical results.

## 3.5   Comparison and conclusion

The coupling ranges of other published SIW coupling mechanisms are compared to this work in Table 3.6. The coupling structures presented offers similar ranges when compared to work done in [8], [10], [37], [42], [45] and [46]. However this design shows the added benefit of realising both positive and negative couplings in the same structure, without any external lines or slots. The structure also retains the miniaturisation advantages of the T-ridge guide as compared with normal dielectric filled waveguide or standard SIW guide. Finally it is shown that the pedestal resonator is easily implementation in SIW, as shown in the filter design.

| Work | Coupling Range | | | f0 | BW |
|---|---|---|---|---|---|
|  | Positive | Negative | Mixed | (GHz) | (%) |
| [37] | 0.002 - 0.0325 | -0.0325 - -0.002 | - | 20.5 | 4 |
| [8] | 0 - 0.0109 | -0.0105 - 0 | - | 5.87 | 2 |
| [42] | 0.0125 | -0.0408 | -0.0608 | 13 | 4.5 |
| [45] | 0.004 - 0.036 | - | -0.015 - 0.034 | 14.3 | 1.4 |
| This work | $0 - 0.0858$ | -0.045 - 0 | $-0.045 - 0.018$ | 5 | 5 |

**Table 3.6:** Comparison of coupling ranges.

In this chapter a proof-of-concept sixth order cross-coupled SIW bandpass filter is presented for coupled resonator filters requiring both electric and magnetic coupling in the same structure. All coupling mechanisms are discussed in detail, with graphs showing typical achievable values. After compensating for a difference in post-processed layer thickness of the top layer, the measured results are in good agreement with the simulation and theory. From the results it is clear that the use of both positive and negative cross-coupling allows for transmission zeros at real frequencies, as well as group delay equalization. The SIW pedestal resonator structure lends itself very well to the implementation of both positive and negative cross-coupling.

# Chapter 4

# Partially air-filled pedestal resonator and filter

## 4.1 Introduction

Microwave filters and resonators are commonly designed with planar or waveguide technology. Planar topologies include microstrip line, stripline, coaxial line etc. while waveguide topologies can be different shapes including rectangular or circular. Planar structures are very easy to manufacture and are easily integrated into systems, they are also cheap, small and light weight. However, because most of these structures include the use of dielectric material, they have lower Q factors and higher losses associated with them. Waveguides have much higher Q factors as the main propagating medium is air, they also have better power handling capabilities. However, these structures are larger, heavier and difficult to integrate into systems.

One of the main reasons for lower Q factors in SIW structures in comparison to other guides is the presence of dielectric material. To reduce the losses and improve the Q factor air-filled SIW (AFSIW) structure was proposed in 2006 [11], where air is the main propagating medium of the signal. AFSIW structures provides a good compromise between SIW and standard waveguides. Since then this topology has been investigated to a great extent. Several components other than filters have been presented such as phase shifters [51], [52], and a leaky-wave antenna [53]. This chapter will focus on microwave filters.

A number of AFSIW, also known as empty SIW (ESIW) [54], filters have been presented [55],[56], [57], [58], [12], [14], [59], [60], [61], [61]. In most cases the proposed filters consists of three layers, a top and bottom metal layer with a micro-machined dielectric middle layer. These structures are still easy to integrate into planar systems and relatively small in size. The filters also show higher Q factors in comparison to traditional SIW topologies. For filters operating in the C-and X-frequency bands Q factors of around 350 is obtained [14]. For filters operating in the K-band Q factors around 740 is obtained [55]. One drawback of AFSIW structures is that these structure are larger than traditional SIW structures. In this chapter a solution to this problem is given. A partially air-filled resonator is introduced and manufactured. A second order partially air-filled pedestal filter prototype is also manufactured. Further recommendations to increasing the Q factor is given in the conclusion section.

## 4.2 Partially air-filled pedestal resonator

In this section the partially air-filled pedestal resonator is introduced. The basic topology is discussed and the input/output structure is explained. A comparison of Q factors for different pedestal resonators is given to illustrate the advantages of the partially air-filled pedestal resonator.

### 4.2.1 Partially air-filled pedestal resonator topology

The design of the partially air-filled pedestal resonator is based on work done in sections 3.1.1. The basic topology of the partially air-filled pedestal resonator consists of a pedestal plate with dielectric material underneath, to support the plate, and a via in the centre of the pedestal from, the pedestal plate to the bottom metal layer. The basic partially air-filled pedestal resonator can be seen in Fig. 4.1 with the substrate material (in blue) only located underneath the pedestal. The partially air-filled pedestal resonator consists of three main layers as seen in Fig. 4.8, a top and bottom metal layer with the micro-machined dielectric substrate layer. The side walls of the substrate cavity is metallized to create the full cavity. From Fig. 4.2 it is seen that the E-field is concentrated between the top metal layer and metal pedestal.
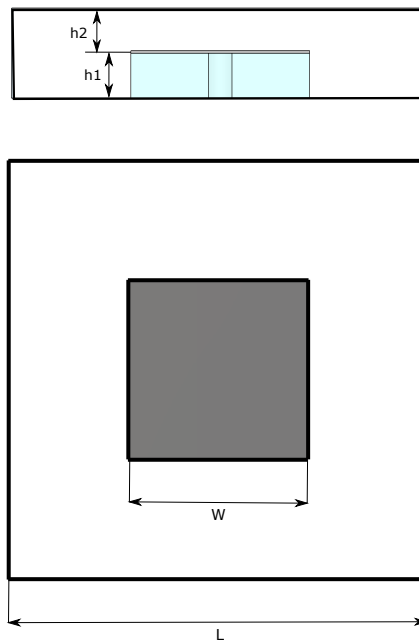


**Figure 4.1:** Basic partially air-filled pedestal resonator.
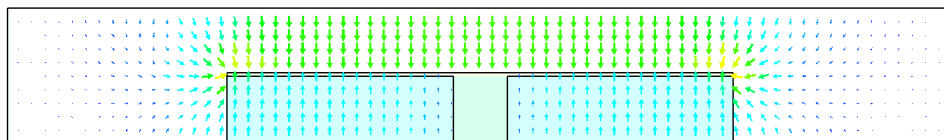


**Figure 4.2:** E field distribution of basic partially air-filled pedestal resonator.

## 4.2.2   Q factor comparison

The main advantage of the partially air-filled pedestal resonator is the increase of the Q factor while maintaining a small size. The Q factor is increased due to the lower dielectric losses associated with the structure. By removing the dielectric material on the top of the pedestal where the field strength is at its maximum, a large decrease in losses, associated with the dielectric, is achieved.

The eigenmode solver in CST is used to compute the Q factor for three different pedestal resonators, a totally filled pedestal SIW resonator, a partially air-filled pedestal resonator and an empty pedestal resonator. It is important to note that the empty pedestal resonator cannot be manufactured, it is only included for comparison reasons. The centre frequency is kept the same by changing the pedestal area accordingly. The setup of the solver and mesh is the same as explained in section 2.4. For these comparisons the centre frequency of each resonator is kept constant at 5 GHz as the outer dimensional area ($LxL$) is increased. The frequency is kept constant by tuning the pedestal width ($W$) accordingly. The ratio of $W/L$ for different $LxL$ areas can be seen in Fig. 4.3. The ratio between $W$ and $L$ decreases as the outer area ($LxL$) increases to keep the centre frequency constant at 5 GHz. The same dielectric material is used for the totally filled pedestal resonator and partially air-filled resonator. The dielectric material used is Mercurywave 9350 with $\epsilon_r = 3.5$ and $\tan \delta = 0.004$. The metal used on all metal surfaces is pure copper with $\sigma = 5.96 \text{ x} 10^7$.

From Fig. 4.3(a) it is clear that for the same outer dimensional size the Q factor is increased. For an outer dimensional area of 196 mm$^2$ the Q factor of the totally dielectric filled pedestal resonator is 186 and for the same size and frequency (5 GHz) the Q factor of the partially air-filled pedestal resonator is 285, resulting in an increase of 53%.
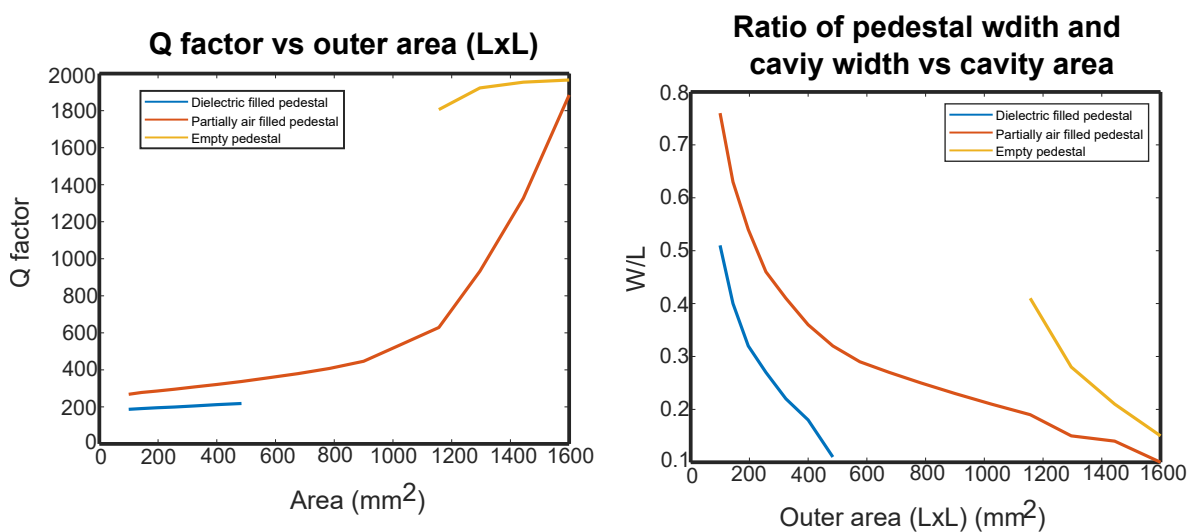


**(a)** Comparison of Q factors for different pedestal resonators.

**(b)** Ratio of pedestal wdith and caviy width vs cavity area.

**Figure 4.3:** Comparison of Q factors and Ratio of pedestal width and caviy width.

There exists a trade off between Q factor and size of a resonator. As the size increases

the Q factor increases because more energy is able to be stored. The Q factors obtained for the empty pedestal resonator is in the range of 1800 - 2000, this is much higher in comparison with the totally dielectric filled pedestal resonator and partially air- filled resonator. However the smallest area that is obtainable for a 5 GHz resonator is 1156 mm² which is much larger in comparison. The partially air-filled pedestal resonator is able to achieve a wide range of sizes where the totally dielectric filled pedestal resonator is limited in size and thus limited in Q factor for the same material and centre frequency. Where the area of the cavity is around 1600 mm² the pedestal is so small that it looks like an empty cavity. From the results it is clear that the partially air-filled pedestal results in a large range of design options.

## 4.3   Manufacturing process overview

Micro-machining manufacturing techniques are utilized to develop a partially air-filled pedestal resonator. The process of manufacturing a partially air-filled pedestal resonator consists of eight steps. These steps are shown in Fig. 4.5 to 4.7. In the figures the blue indicates dielectric material and the orange indicates copper.

A double sided metallized dielectric slab is taken and the input structures with the pedestal is etched out of the slab, this can be seen in Fig. 4.5 where AA' and BB' shows the different cross-sections of the resonator.

The next step is to drill the input/output and post via holes. The bottom layer of substrate is micro-machined away leaving the pedestal and input structures connected to the cavity walls, seen in cross-section BB'and CC' in Fig. 4.6. Metallization through electroplating is done to the entire structure to ensure the via holes are metallized inside and the sides of the cavity is metallized. The drilled via holes and metallization can be seen in Fig.4.6.

Because metallization is done to the entire structure, de-metallization of certain part is needed. The sides of the input structure and the sides of the pedestal is de-metallized with a drill. A copper foil is then pressed and attached to the bottom of the resonator through thermo-diffusion to ensure the sides of the wall is connected to ground, as seen in crosss-ection BB' and CC' in Fig. 4.7.The same is done on the top to ensure the cavity is created. The last step is to etch the coplanar input line on the top layer as seen in cross-section AA' of Fig. 4.7.



**Figure 4.4:** Double sided metallized dielectric slab.
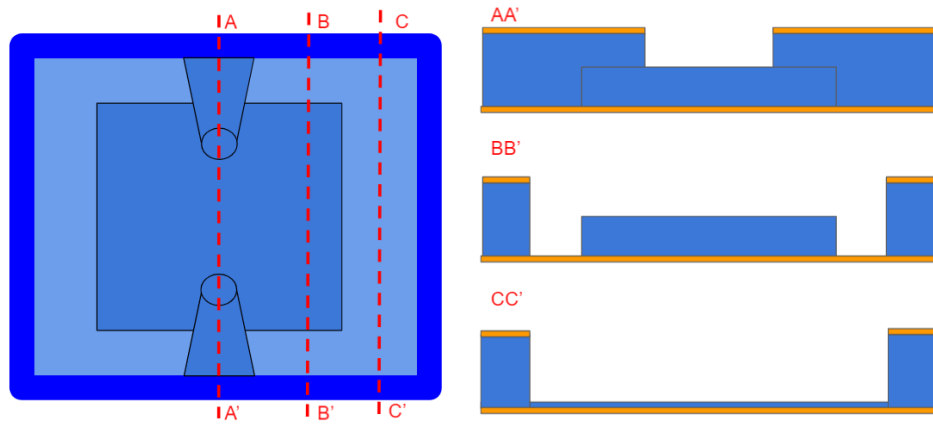
**Figure 4.5:** Top and side view after manufacturing step 1 at different cuts.
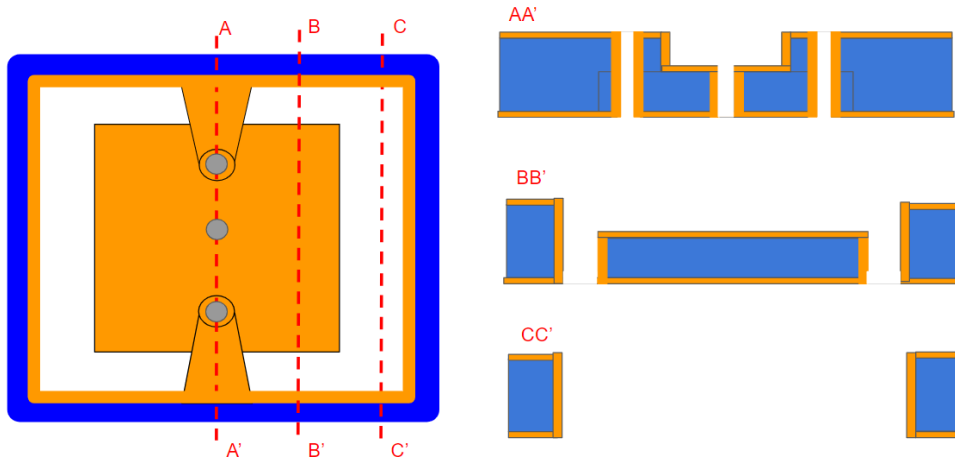


**Figure 4.6:** Top and side view after manufacturing steps 2,3 and 4 at different cuts.
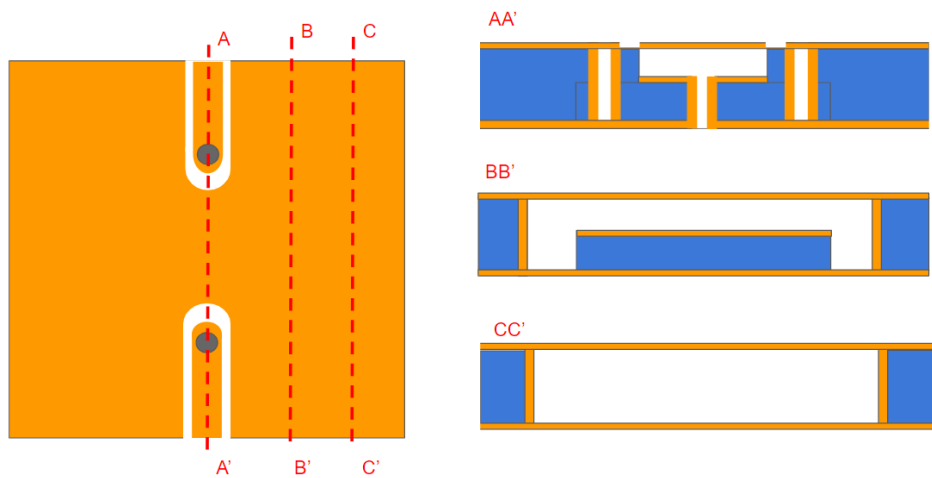


**Figure 4.7:** Top and side view after manufacturing steps 5,6,7 and 8 at different cuts.

## 4.4   Final partially air-filled pedestal resonator topology
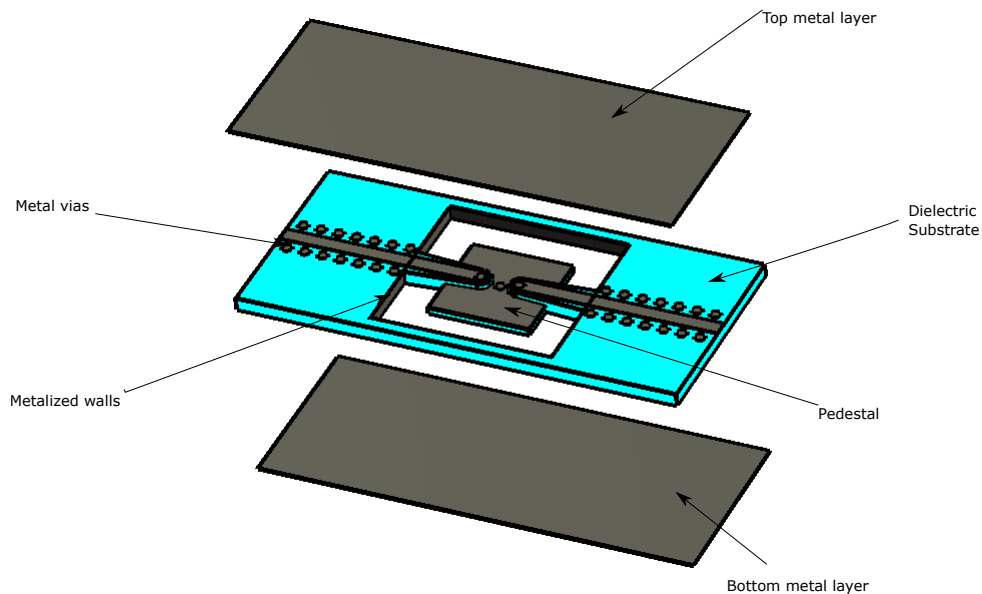


**Figure 4.8:** 3D structure partially air-filled pedestal resonator with input and output.

The input/output structure is based on the previous input/output structure in section 3.2.1. To support the 50 Ω coplanar input line and coupling via, substrate is needed. The input/output substrate is the full height of the substrate layer and is tapered from the cavity wall to the feed via. This is to ensure structural support when manufacturing. The tapered input dielectric structure merges with the square pedestal substrate, this is done so that the square pedestal is secured to the rest of the cavity and is not floating. As in the previous designs the pedestal is placed at half of the total height of the cavity. The feed via is drilled from the top to the bottom of the substrate and is placed a distance $d$ from the post via of the pedestal, in this way magnetic coupling is achieved as in section 3.2.1. The coplanar-line is extended 10 mm outside the cavity to enable measurement of the resonator. Via holes are placed along side the coplanar-line to ensure good connection to ground. A top and side view of this structure can be seen in Fig. 4.10 and Fig. 4.9, respectively.
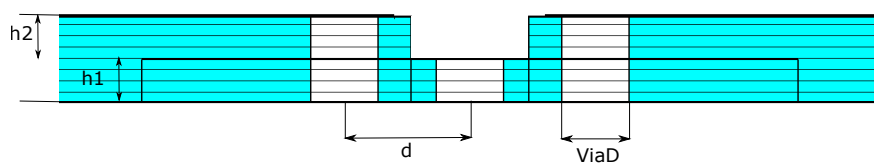


**Figure 4.9:** Side view of partially air-filled pedestal resonator.
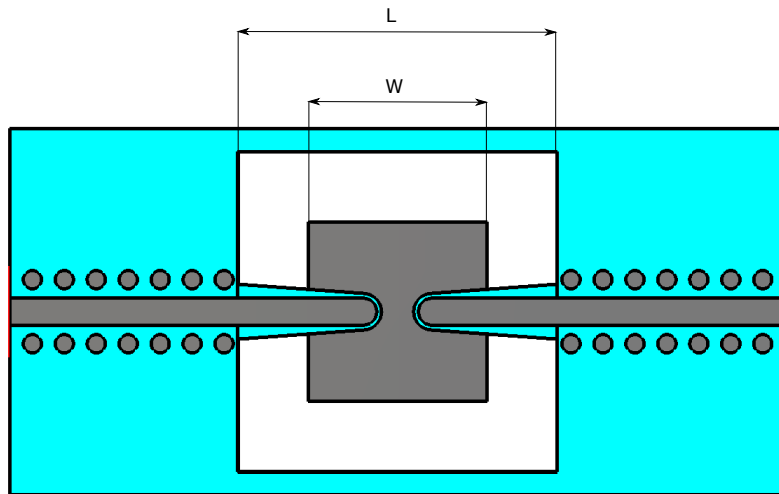
**Figure 4.10:** Top view of partially air-filled pedestal resonator.

The input/output coupling values for this structure can be seen in Fig. 4.11. The coupling value is varied by varying the distance ($d$) between the pedestal post and input via. Values from 0.004 to 0.0095 is obtained. As the distance between the two vias increases the coupling decreases.
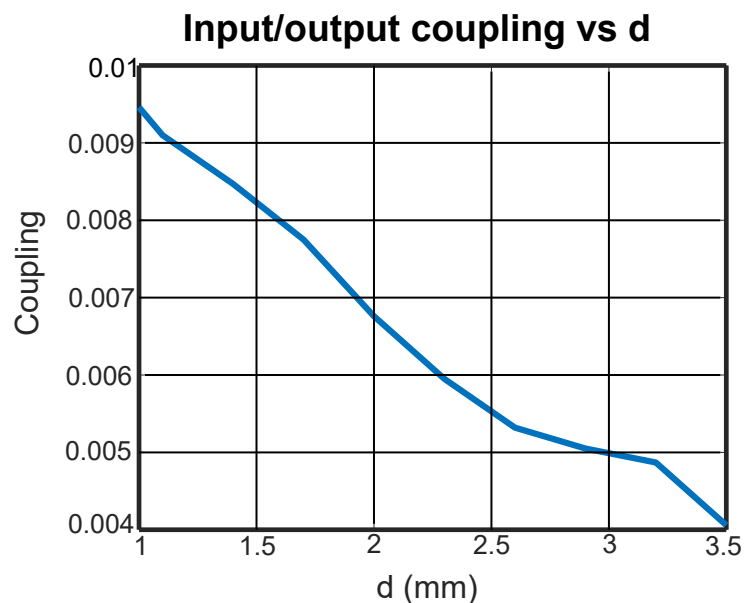


**Figure 4.11:** Input/output coupling values vs $d$ for a fixed pedestal and cavity size.

## 4.5 Partially air filled pedestal resonator and filter results

A partially air-filled resonator and second order filter is manufactured at Protecno with the manufacturing process explained in section 4.3. The dielectric material chosen is Rogers 4003 with $\epsilon_r = 3.55$ and $\tan \delta = 0.0027$. The structure is metallized with copper. The resonator and filter is designed to operate at 5 GHz.

### 4.5.1 Partially air-filled resonator

The dimensions of the partially air-filled resonator are summarized in Table 4.2.

| Parameter | $L$ (mm) | $W$ (mm) | $h1$ (mm) | $h2$ (mm) | $viaD$ (mm) | $d$ (mm) |
|---|---|---|---|---|---|---|
| | 14 | 7.84 | 0.5 | 0.5 | 0.8 | 1.5 |

**Table 4.1:** Parameter values for partially air-filled pedestal resonator.
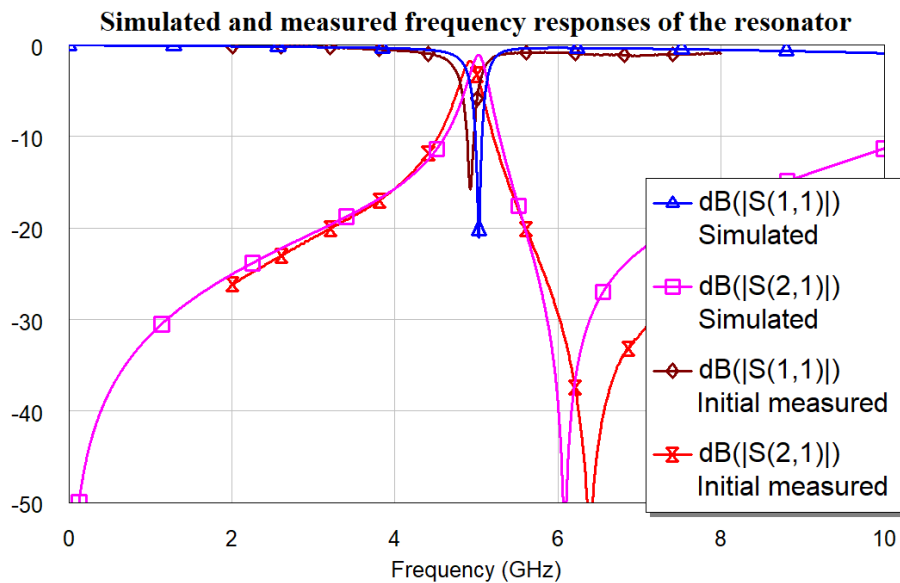


**Figure 4.12:** Initial comparison between the simulated and measured frequency responses for the resonator.

The initial simulated and measured results can be seen in Fig. 4.12. A small change in centre frequency can be seen. This is due to the top metal layer of the resonator not being perfectly straight and at the correct height. Due to the pressing of the top metal layer a slight dip is observed, this can be seen in the slight colour difference. A picture of the resonator can be seen in Fig. 4.13.
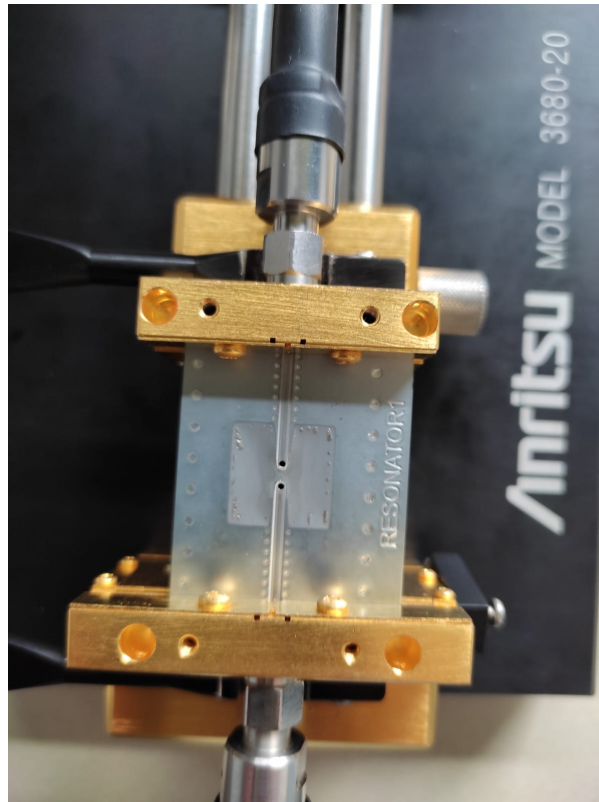
**Figure 4.13:** Photo of PAPSIW resonator.
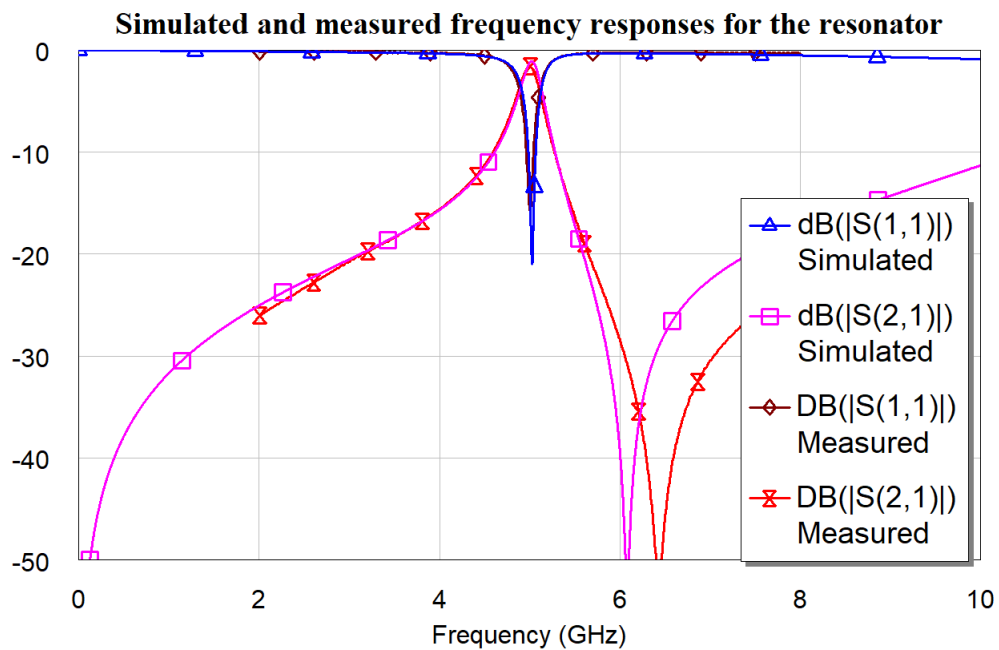


**Figure 4.14:** Comparison between the simulated and measured frequency responses for the corrected resonator.

The frequency shift is solved by using additive tape to correct the top metal plate position and shape, this is seen in Fig. 4.14. Another and better solution to this problem

would be to use more ridged and thicker copper foils. There is also a shift seen in the transmission zero. The transmission zero is created by the input and output coupling inside the structure. This fact was confirmed by placing a metal plate between the input and output and no change was seen. The simulated Q factor for a fully dielectric pedestal resonator at 5 GHz is 186, while the measured Q factor for the PAPR is 285.

### 4.5.2 Partially air-filled second order filter

The second order partially air-filled pedestal filter can be seen in Fig. 4.15
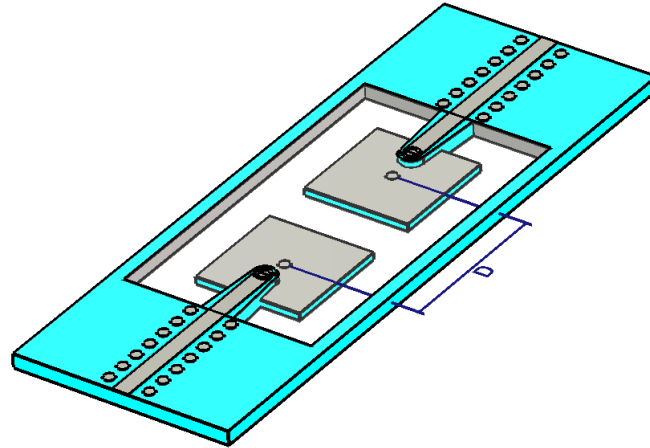


**Figure 4.15:** Second order partially air-filled pedestal filter.

The dimensions of the partially air-filled filter is summarized in Table 4.2.

| Parameter | $L$ (mm) | $W$ (mm) | $h1$ (mm) | $h2$ (mm) | $viaD$ (mm) | $d$ (mm) | $D$ (mm) |
|---|---|---|---|---|---|---|---|
| | 14 | 7.75 | 0.5 | 0.5 | 0.8 | 2.16 | 11.4 |

**Table 4.2:** Parameter values for second order partially air-filled pedestal filter.
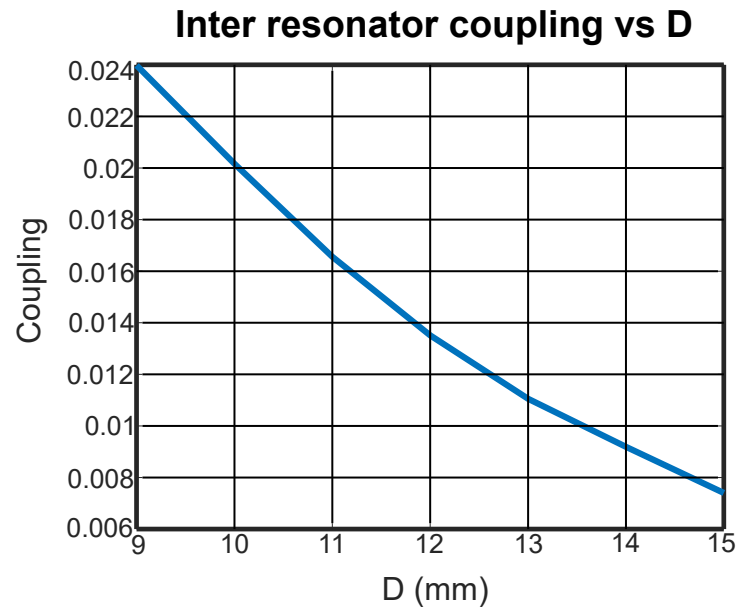
**Figure 4.16:** Inter resonator coupling vs $D$ for fixed pedestal and cavity size.

Inter-resonator coupling for this structure can be seen in Fig. 4.16. Inter-resonator coupling values from $0.006$ to $0.024$ can be obtained by changing the distance $(D)$ between the adjacent resonators. As the distance increases between the resonators the coupling strength decreases.
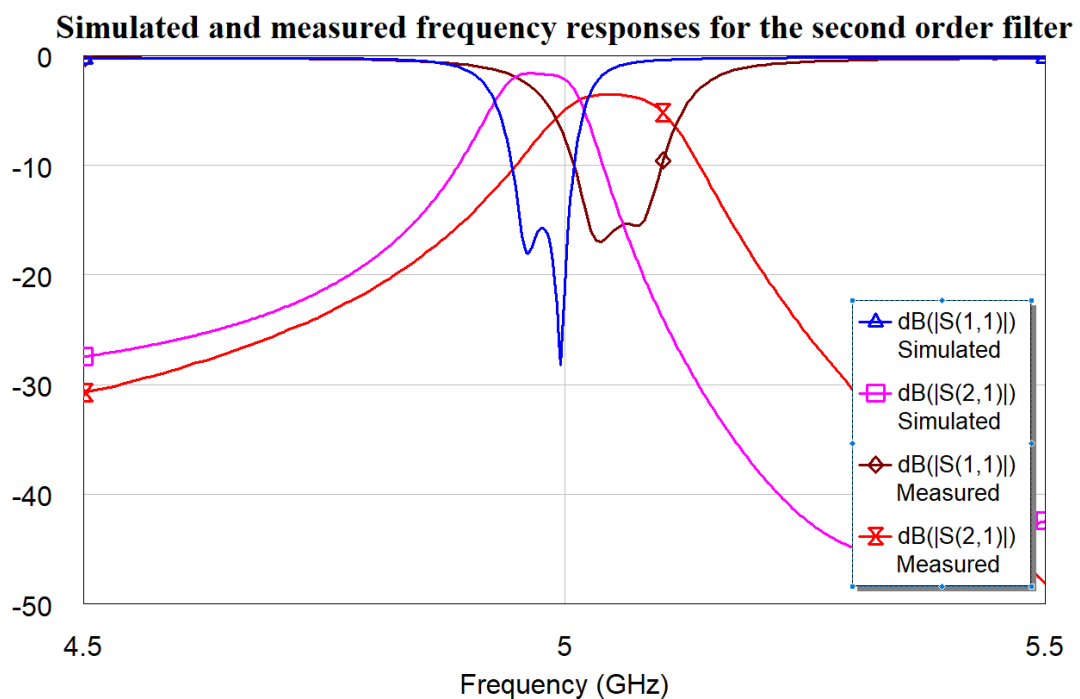


**Figure 4.17:** Comparison between the simulated and measured frequency responses for the second order filter.

The simulated and measured results can be seen in Fig. 4.17. Again a slight frequency shift is seen for the same reason as discussed above. However, over all good results are

obtained and the filter functions well. A picture of the fabricated filter can be seen in Fig. 4.18. The measured centre frequency is 5.047 GHz. A -3 dB bandwidth of 2.65% is obtained from 4.981 GHz to 5.115 GHz. The insertion loss is -3.533 dB. The simulated insertion loss is 1.622 dB. The insertion loss is slightly more than the simulated response. This is due to the fact that surface roughness was not accounted for in the simulated results.
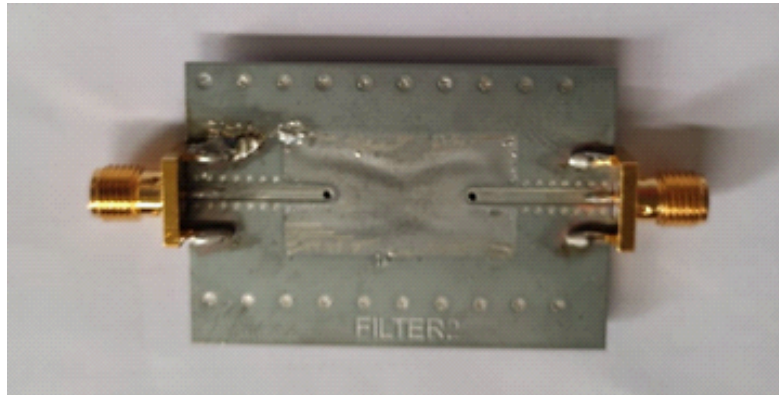


**Figure 4.18:** Photo of second order partially air-filled pedestal filter.

## 4.6 Conclusion

This chapter introduced the novel partially air-filled pedestal resonator to increase the Q factor of relatively small sized cavities. The resonator is based on work done in section 3.1.1. A comparison of three different types of pedestal resonators was done between a totally filled pedestal SIW resonator, a partially air-filled pedestal resonator and an empty pedestal resonator, showing the increase in Q factor for the same size as the totally filled pedestal resonator and the wide range of Q factors that can be obtained with the partially air-filled pedestal resonator. Then the use of micro-machining to create these novel resonators is illustrated and explained. Utilizing micro-machining a structure like the partially air-filled pedestal is possible and making it possible to increase the Q factor while maintaining a small size. A resonator and second order filter prototypes are manufactured, using the manufacturing process explained, and tested. The manufacturing processed resulted in good resonators and filters operating with higher Q factors in comparison to resonators and filters manufactured with dielectric material. It was shown that the Q factor can be increased from 186 for a fully filled dielectric resonator to 285 for a partially air filled resonator. This shows a 34.7% increase.

The Q factor can further be increased by changing the distance between the top metal wall and the metal pedestal. From Fig. 4.19 it is clear that as the distance decreases the Q factor increases. From Fig. 4.2 it is known that the field is concentrated between the top metal wall and metal pedestal, when the distance between these two metal plates are decreased the field intensity increases thus more energy is stored, thus increasing the Q factor. For these simulations the centre frequency is kept constant at 5 GHz with a constant outer dimension $L = 14$ mm and a constant $h1 = 1$ mm while the height $h2$ is increased. The centre frequency is kept constant by changing the pedestal width $W$ accordingly. The change in ratio $W/L$ as the height $h2$ is changed can also be seen in Fig. 4.19.

**Figure 4.19:** Q factor and Ratio of pedestal width and cavity width vs ratio of top height over total height ($h1 = 1$ mm) .

# Chapter 5

# Tunable SIW pedestal resonator and filter

## 5.1 Introduction

The frequency spectrum is increasingly being used for multiple purposes with more bands needed to provide more services. Various solutions to cover more frequency bands already exist, such as filter banks, multi-band filters and tunable/reconfigurable filters. Filter banks provide very high quality performance, however these structures are large. Isolation problems occur in multi-band filters. Tunable filters however do not have this problem. Tunable filters are also useful in post-fabrication to optimize the performance. Better isolation can be achieved with tuning of devices.

In this chapter the focus will be on tuning of microwave SIW filters. Two methods exist for tuning the centre frequency of a filter, i.e. changing the capacitive characteristics or inductive characteristics, or both, of a resonator. Inductive tuning of a SIW cavity is possible with using ferrite slabs. This concept was first introduced in [62]. This method consists of placing ferrite slabs within a SIW cavity and then applying a transverse magnetic field. In [63] the writers make use of both electric and magnetic tuning. Electric tuning is achieved using a similar method proposed in [64]. Magnetic tuning is made possible by the ferrite slabs and varying transverse magnetic field applied causing variable external magnetic fields. A tuning range of 8% is achieved by manipulating the electric and magnetic fields simultaneously. An unloaded Q factor of 130 is possible. A drawback to this approach is that it is difficult to insert the ferrite slabs into the dielectric material.

It is more common to tune the centre frequency by changing the capacitive characteristics with active components. In the field of microwave tunable resonators and filters, solutions exist for both continuous tuning and switched tuning. The most common active component used to achieve continuous tuning is the varator diode. Continuous tuning can also be realized with mechanical screws such as in [65]. Positive-intrinsic-negative (PIN) diodes or RF microelectromechanical systems (RF-MEMS) switches are commonly used in switched systems. The basic consept is that the cavity is loaded in some way, most commonly a via from top to bottom that is isolated from the ground plane with an etched slot, then the active component is place over the etched slot connecting the ground plane to the loading structure.

In [65] a mechanically tuned SIW filter is introduced. The main tuning element consists of a mechanically controlled screw that is then connected to a metal flap. The screw is isolated from the cavity with an etched annular ring slot. When the screw is turned, the point at which the metal flap is connected is changed, thus altering the E-field distribution and changing the resonant frequency. For a single resonator a tuning range of 8% is achieved with measured Q factor of 94. Using multiple tuning elements, the tuning range can be increased. A drawback to this design is the difficulty in fabrication because of the insertion of the metal flap connected to the screw and via post. An advantage to this tuning element is that it can be placed anywhere in the cavity, therefore even bandwidth tuning is possible by placing the tuning element between resonators.

A big advantage with electrically tuned filters is that the filter can be designed in an enclosed system, as opposed to mechanically tuned filters that are naturally open systems. When designing tunable filters the tuning range and Q factor are commonly the most important factors to consider. There exists a trade off between these two factors. Either the frequency range is very low with high Q factors at each stage or the frequency range is wide with a decreasing Q factor. Another problem that arises when tuning a filter is that the coupling between resonators and the external Q factor also needs to be tuned when changing the centre frequency, giving rise to a more complex design with added components and thus more losses in the system. The bandwidth of a filter does not stay constant as the centre frequency is tuned if the coupling between resonators is not tuned simultaneously. The response of the filter also deteriorates when the external Q factor is not tuned simultaneously. In this chapter the focus is on centre frequency tuning and tuning of the external Q factor to optimize the response of the filter over the tuning range.

A popular tuning approach is continuous tuning with varactor diodes. Sirci, *et al.* [64] first introduced a tuning method where a metallized via post is connected to a metal patch on the top of the cavity. The biasing voltage of the varactor diode is changed, thus changing the loading on the via post. This changes the electric field distribution resulting in a change of resonant frequency. A tuning range of 18% is achieved with this method, with an unloaded Q factor of 40 - 160 over the tuning range. An advantage of this structure is that it consists of only one layer, thus simplifying the fabrication process. A drawback to this structure is that for multiple tuning structures the total leakage from the top wall increases, resulting in a decrease in Q factor. In [66] a varactor diode is coupled to a SIW cavity from the side wall, to create a tunable SIW cavity-backed antenna oscillator. The varactor diode is coupled to the SIW cavity through an opening in the side wall. A tuning range of 2% is achieved with a Q factor of 286-299 over the tuning range. Because the tuning element is placed where the electric field is at its weakest, the tuning range is limited but the Q factor is affected less. In [67] a cylindrical SIW cavity with a centre via post connected to the top and bottom layers of the cavity is presented. An annular slot ring is used to isolate the centre via from the rest of the cavity. A number of varactor diodes are placed over the etched slot to load it. For a single resonator a tuning range of 1.6 - 2.84 GHz is achieved with an unloaded Q factor of 35 - 150 over the tuning range. It should be noted that all of these results are for normal, unloaded SIW. For loaded SIW resonators, the Q factor decreases as the loading increases.

As mentioned earlier, another approach to tuning, is switched tuning using either PIN diodes or RF-MEMS switches. In [68] a RF-MEMS switched tunable two-pole SIW filter is presented. The tuning structure consists of tuning posts connected to RF-MEMS

switches within the SIW cavities. When the switch is turned on, surface currents are induced on the tuning via, the magnetic field is then concentrated around the tuning via resulting in a change of all the fields inside the cavity, causing a frequency shift. The filter is able to tune from 1.2 - 1.6 GHz with an insertion loss of 2.2 - 4.1 dB and Q factor of 93 - 132 over the tuning range. Using 3 RF-MEMS switches per post and 3 posts per cavity, 14 different states are possible. This filter showed fine frequency resolution giving a continuous type of result. A drawback to this structure is that it consists of two layers to accommodate for biasing of the switches, thus increasing the fabrication complexity.

A fouth order digitally tunable SIW filter is presented in [69] using RF-MEMS single-pole single-throw (SPST) switches. Four switches were placed on the top layer of the cavity with four tuning posts, each isolated from the top layer with a gap, at specific point within the cavities. Four different frequency states are achieved with this design, with a total tuning range of 2.3%. A two-pole half mode tunable SIW filter is presented in [70]. The resonator is tuned using tuning networks attached to the open side of the resonator. Each tuning network consists of a parallel network of transmission lines connected to a via-hole to ground. The transmission lines are switchable with the FR-MEMS switches and can be connected or disconnected to or from the resonator. A tuning range of 28% is achieved with 13 different states from 1.2 GHz to 1.6 GHZ. The Q factor varied from 75 to 140 over the tuning range with an insertion loss of 1.2 dB to 3.4 dB over the tuning range.

Recently an RF-MEMS tunable bandpass filters was presented in [71]. The filter consists of folded ridged quarter-mode SIW cavities. Two different folded ridged quarter-mode substrate integrated waveguide (FRQMSIW) filters with different loading is given. The folded resonator consists of two layers of substrate divided with a metal layer connected to the top wall with a blind via. The tuning structure is connected to the blind via with an RF-MEMS switch. The switches are used to change the loading admittance seen by the resonator. The RF-MEMS switch is loaded capacitively or inductively. The inductively loaded second order filter achieved 4.4% tuning range with a Q factor varying from 71 to 135. The capacitively loaded filter achieved a much higher tuning range of 33.1% and a varying Q factor of 33 to 204.

In 2006 the authors of [72] proposed a novel tunable cavity compatible with planar technology. A metallic vertical post is inserted in the cavity with a floating circular ring etched around to the post. Surface actuators are used to connect the metallic ring to the ground plane. The filter is able to tune from 8 to 10 GHz. In [73] a two-pole SIW filter was made tunable with PIN diodes. A single PIN diode is connected to a via post isolated with a square etched slot. The second order filter consisted of 4 via post with a PIN diode each. The filter provides 6 states resulting in a 25% tuning range from 1.55 GHz to 2 GHz. The Q factor varied from 120 to 101 over the tuning range.

A similar design was presented by Sirci *et. al* in [74]. A 2-pole tunable SIW filter is presented. Coupled coaxial SIW resonators is the basis of the structure presented. PIN diodes are connected to a via post with an etched slot. The proposed filter is able to tune in 3 states from 5.58 to 6.17 GHz with an insertion loss of 2.4 dB to 1.6 dB over the tuning range. Low resistance PIN diodes are used with a forward resistance of 1.38 $\Omega$ resulting in higher Q values.

It is clear that there are several methods for implementing tunability in SIW filters us-

ing PIN or varactor diodes, or other tuning mechanisms. The choice of tuning element depends on the application. The next section discusses more on how the tuning elements work and what their main advantages and disadvantages are.

## 5.2    Tuning elements

The resonant and/or coupling properties of a transmission line can be altered with the use of tuning elements. For the purpose of this dissertation, only centre frequency tuning is considered. Centre frequency tuning is commonly achieved by changing the effective length of a resonator. The effective length of a resonator consists of the physical length of the line and the additional capacitive or inductive components. Centre frequency tuning can be realized by using a continuously variable component or by switching line sections in and out of the circuit. To achieve continuous tuning, the most common element used is the varactor diode. While elements such as PIN diodes and Micro-Electro-Mechanical System (MEMS) switches are commonly used to achieve switched tuning.

### 5.2.1    Varactor diodes

Varactor diodes have fast tuning speeds, large tuning ranges, are cheap, readily available and have good power consumption. However, they have high losses associated with them (because of the series resistance) and have non-linear characteristics as can be seen in Fig. 5.1. A varactor diode (varicap diode/tuning diode) is a p-n junction diode. The p (donor) terminal is positive consisting of p-type material and the n (acceptor) terminal is negative consisting of a n-type material. A depletion region is created when the two terminals make contact for the first time. By applying a reverse biasing voltage across the terminals, the width of the depletion region is changed. This acts as a variable capacitor. Varactor diodes operate close to the breakdown voltage. There are two types of varactor diodes: abrupt and hyper-abrupt.
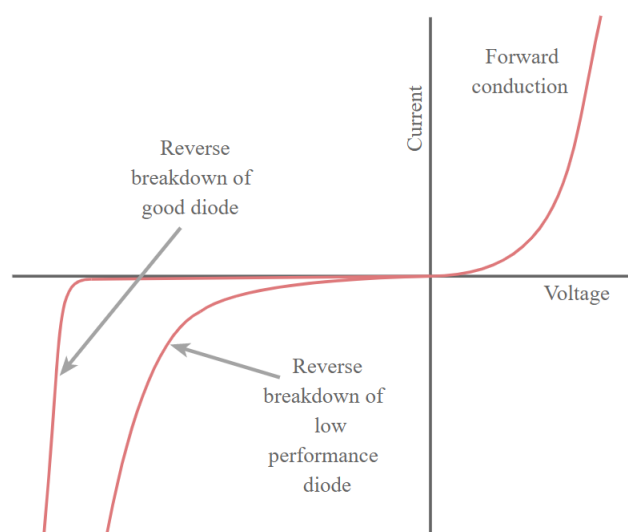


**Figure 5.1:** Typical IV characteristic of a varactor diode [2].

## 5.2.2 PIN diodes

PIN diodes have fast switching times and high power handling capabilities. A PIN diode is a semiconductor devise that can operate as a switch or variable resistor at high frequencies. Unlike varactor diodes that operate using voltage, the PIN diode is operated with current. A PIN diode is used for switching if the current is turned on or off. PIN diodes are used as switches in the forward biased state at RF and microwave frequencies, unlike the varactor diode that is used in the reverse biased state. The circuit models for the on and off states of a PIN diode can be seen in Fig. 5.2.
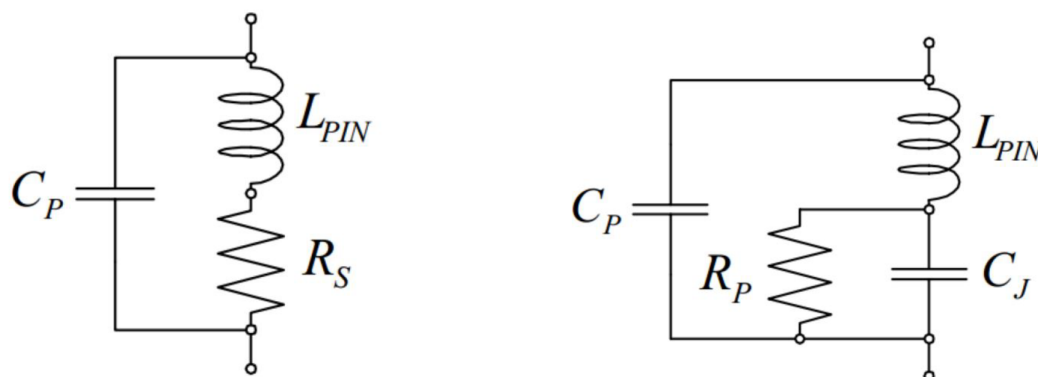


**(a)** Circuit model for the On state of a PIN diode. **(b)** Circuit model for the Off state of a PIN diode.

**Figure 5.2:** Circuit model for On and Off states of a PIN diode [3].

The capacitance of the package is $C_p$, $L_{PIN}$ is the inductance of the package, $R_s$ is the forward bias series resistance, $R_p$ is the dissipative resistance and $C_j$ is the junction capacitance. These models were used in simulation. The intrinsic region of a PIN diode consists of an un-doped silicon material. Due to this un-doped region there exists a resistive section in the diode and current flow is only possible with a high level of charge carriers. A thin intrinsic region results in faster switching speeds, while thicker regions are better for high power applications.

## 5.2.3 MEMS

MEMS have low losses and are small in size. However, these components break easily, have slow tuning speeds, and can provide either small tuning ranges or binary tuning. MEMS technology can be used as variable capacitors (varactors) or capacitive switches. A MEMS component consists of a micro-machined cantilever/bridge which bends in response to an applied voltage. These components require large voltages to be tuned, they are more complicated to incorporate in designs. Because MEMS are so fragile these components require the use of packaging that causes these components to lose most of their benefits. The other option is to integrate the MEMS component into the structure, this leads to complex design problems.

## 5.3 Tunable resonator topology

The proposed resonator is based on previous work done by [18] in combination with work done by [69]. The basic SIW resonator is designed similar to conventional rectangular waveguide cavities. The pedestal is added and tuned to realize a resonator at 5 GHz. The pedestal resonator leds itself well for adaptation because there exists a loading structure at the maximum E-field of the SIW cavity to which components can easily be added from the outside. From Fig. 5.3 it can be seen that the inductance will change when variable components are added. The resonator can be designed to have continuous tuning by using a varactor diode or switched tuning by using a PIN diode for example. As mentioned before varactor diodes have high losses associated with them and is a non-linear component. When a component is added a series resistance will also be added increasing the losses of the resonator. In the interest of designing a high Q resonator PIN diodes are chosen due to their commonly smaller $Rs$ values.
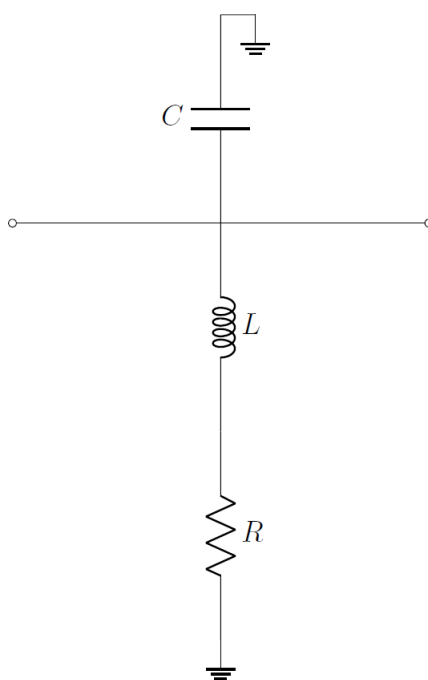


**Figure 5.3:** Basic circuit model of pedestal resonator.

### 5.3.1 Tunable pedestal resonator with wire bondings

As a first approach to making the pedestal resonator tunable, the principle used in [69] is extended for use on the pedestal resonator structure. As discussed in the introduction, in [69] a via post is inserted in the SIW cavity from the top wall to the bottom wall and isolated from the top wall with etching. Wire connections is placed over the etched slot connecting the via post to the top wall of the cavity. To apply this idea to the pedestal structure, four bonding wires are used. The bonding wires are also connected over an etched slot separating the loading structure from the ground planes. The initial tunable pedestal can be seen in Fig. 5.4(a).

**(a)** Side and top view of tunable pedestal resonator with wires.



**(b)** Different current distributions for different number of wire bondings.
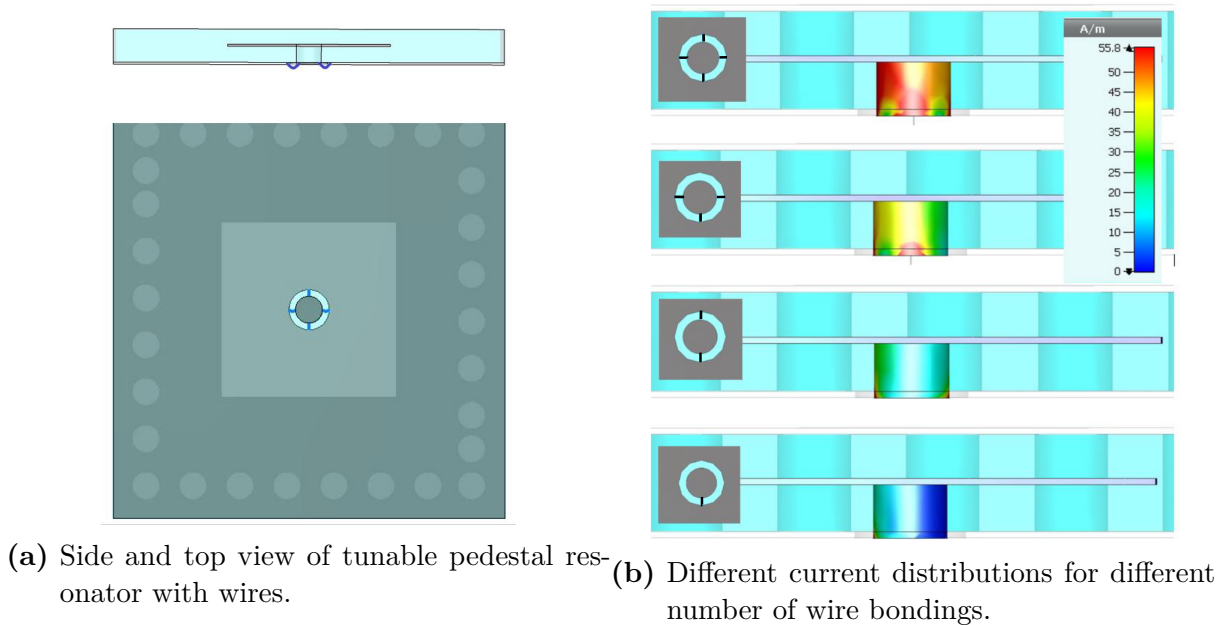
**Figure 5.4:** Side and top view of tunable pedestal resonator with wires and different current distributions for different number of wire bondings.

The input and output coupling is achieved with a 50 Ω coplanar-line in the top ground plane of the resonator and a via grounded at the bottom ground plane of the resonator, as in section 3.2.1 and shown here again for ease of reading in Fig. 5.5.
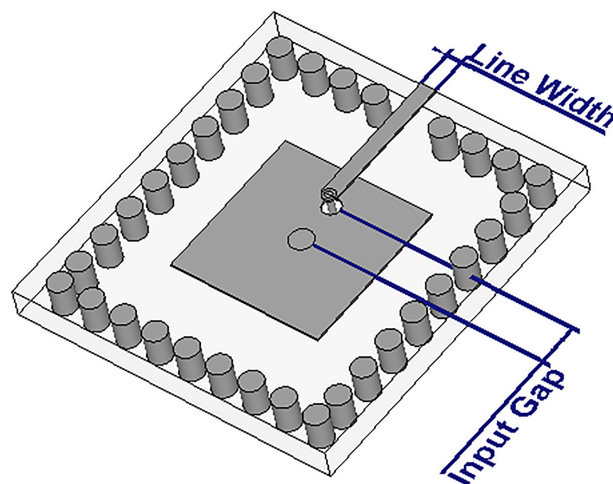


**Figure 5.5:** Input/Output coupling of the pedestal SIW resonator.

A simple circuit model for the pedestal resonator with wire bondings can be seen in Fig. 5.6. The pedestal plate and the top layer of the cavity can be modeled as a capacitor, the via post can be modeled as an inductor in series with a resistor as mentioned in section 3.1.1. It should be clear from Fig. 5.6 that the model shown here is only a rough one, as it does not account for the difference in effective inductance caused by the asymmetric current distribution due to the wires. A strip is seen as an inductor in series with a

resistor. The four strips are seen in parallel with each other to ground. The ring slot is seen as a capacitance in parallel with the wires.
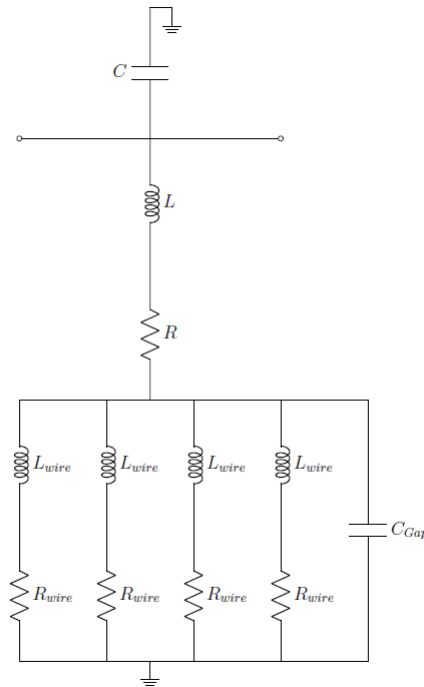


**Figure 5.6:** Circuit model of pedestal resonator with wire bindings.

Depending on the number of wires connected, the cavity resonance undergoes a specific frequency shift. This is due to the surface current distribution changing as the number of wires change, resulting in a change in the electric and magnetic field distributions. The change in surface current can be seen in Fig. 5.4(b). As the number of wire bondings change, the total inductance of the resonator changes and thus leads to a frequency shift. Each set of wires represents a different state. As the number of wires increase the frequency increases. There are different combinations of 2 wires (adjacent or opposite) and depending on which combination is chosen the frequency is different. The results refer to the case of two opposite wires, this is chosen to ensure proportional frequency shifts. The frequency shifts are not proportional for the case where adjacent wires are chosen. The simulated results for a single resonator with four different states are shown in Fig. 5.7.
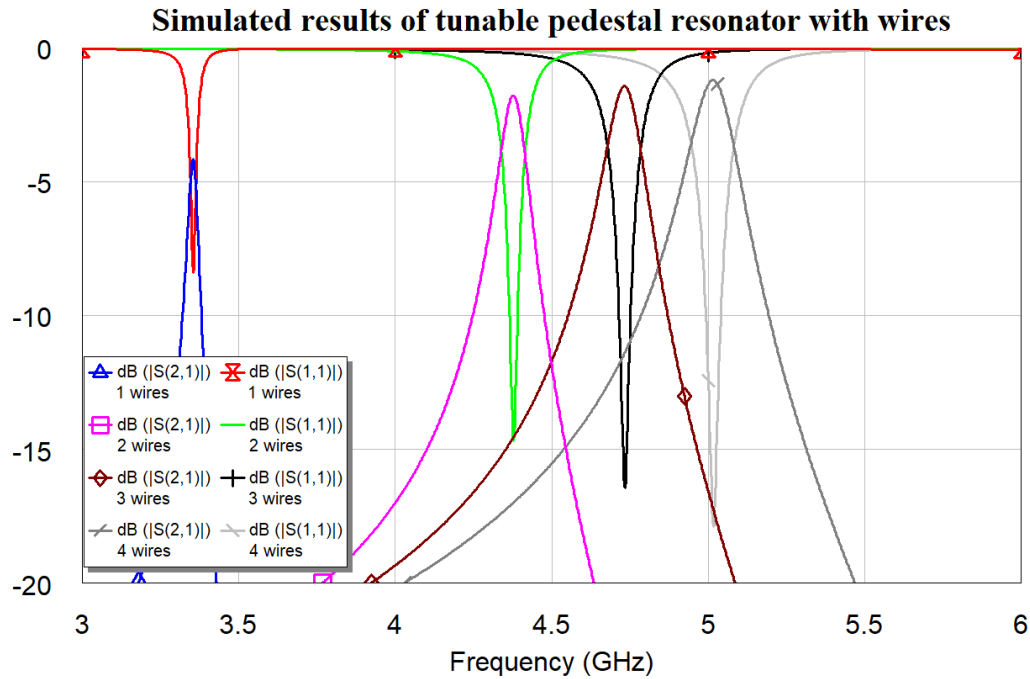
**Figure 5.7:** Simulated results for a single resonator with four different frequency states.

| State | Unloaded Q | $f_0$ (GHz) |
|-------|------------|-------------|
| State 1 | 300 | 3.4 |
| State 2 | 279 | 4.42 |
| State 3 | 260 | 4.75 |
| State 4 | 237 | 5 |

**Table 5.1:** Unloaded Q factor of the tunable pedestal resonator with wire bondings.

The $S_{21}$ degrades as the filter is tuned from having 4 wire bondings, state 4, (at 5 GHz) to having 1 wire bonding, state 1, (at 3.2 GHz). This is because the resonator is designed to operate at 5 GHz with four wire bondings and when the wire bondings are removed the resonator impedance changes causing a mismatch at the input. This is clear from the $S_{11}$ and $S_{21}$ parameters. The unloaded Q factor decreases from state 1 to state 4 as seen from Table 5.1.

## 5.3.2 Tunable pedestal resonator with etched strips

As a second approach to experimentally validate the principle of this tunable design, etched strips are used instead of wires. This was done because strips are more defined and easier to work with and simulate. Strips are used to model an on state, while the absence of the strip models an off state. The input and output coupling is achieved as for the previous case shown in Fig. 5.5. In this way magnetic coupling is achieved between the input via and pedestal post. The bottom view of the pedestal resonator can be seen in Fig.5.8 with four strips etched into the bottom wall of the resonator.
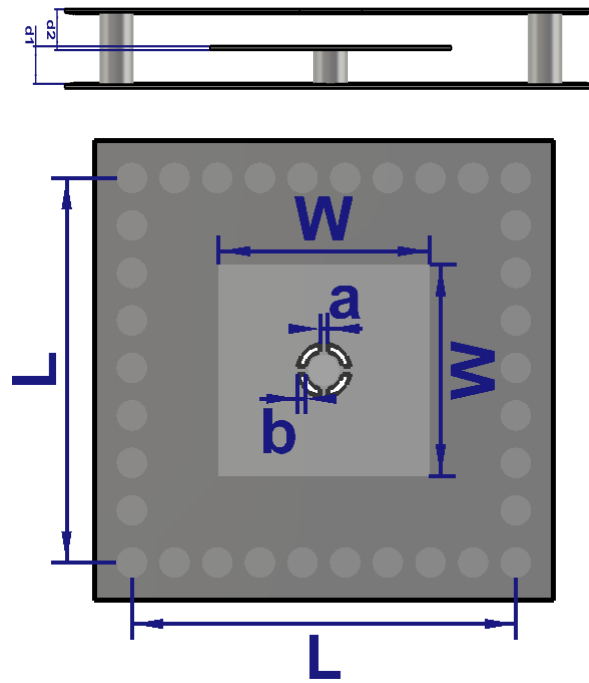
**Figure 5.8:** Side and bottom view of pedestal resonator with strips.

The dimensions of the manufactured resonator is given in Table 5.2.

| d1 (mm) | d2 (mm) | W (mm) | L (mm) | a (mm) | b (mm) |
|---------|---------|--------|--------|--------|--------|
| 0.51    | 0.51    | 5.5    | 10     | 0.2    | 0.2    |

**Table 5.2:** Dimensions of the tunable pedestal resonator with strips.

A set of four resonators were simulated, each with a different number of strips, from one to four. The simulated results can be seen in Fig. 5.9. A clear frequency shift can be seen from 4.074 GHz to 5.405 GHz resulting in a total shift of 1.331 GHz. The frequency stages are however not equally spaced for all the states.
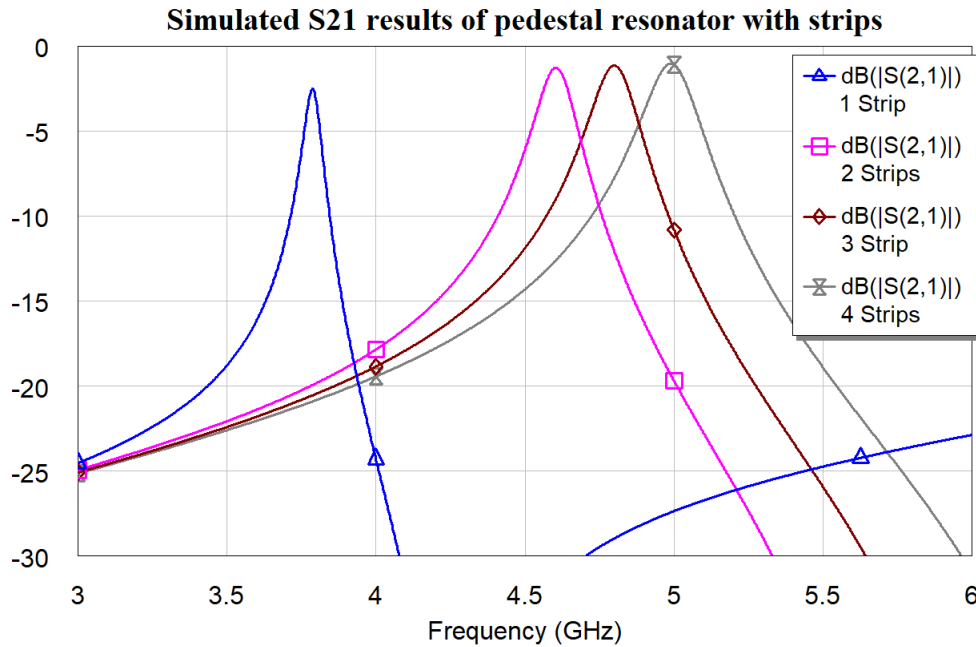
**Figure 5.9:** Simulated S21 results of pedestal resonator with strips.

The simulated unloaded Q values for each state is listed in Table 5.4. State 1 indicates when only one strip is connected and state 4 indicates when all four strips are connected. From this table it is clear that the unloaded Q factor for the simulated resonator decreases as the state is increased.

| State | Simulated $f_0$ (GHz) | Simulated Q factor |
|---|---|---|
| State 1 | 3.786 | 246 |
| State 2 | 4.6 | 247 |
| State 3 | 4.8 | 246 |
| State 4 | 5 | 234 |

**Table 5.3:** Simulated results for the four different states.

### 5.3.3  Third order filter design with etched strips

Tuning of a filter is achieved by tuning all the resonators simultaneously. In the case of the strips used, each resonator has the same number of strips distributed in a way to ensure symmetry of the filter. State 1 is when 1 strip is connected for each resonator. State 2 is when 2 strips are connected for each resonator. State 3 is when 3 strips are connected for each resonator. Finally, state 4 is when 4 strips are connected for each resonator. The filter is designed to operate at 5 GHz in state 4.

It is well known that as the frequency is tuned the response of the filter degrades, this can be seen for state 1 for the third order filter. This happens because the filter is optimally designed to operate at one specific frequency. When the frequency is changed a miss match occurs resulting in deterioration of the filter response. Thus the need arises to

tune the input coupling, which can be achieved with a standard varactor diode inserted in the input line of the filter. The simulated results, with input tuning, can be seen in Fig. 5.10.
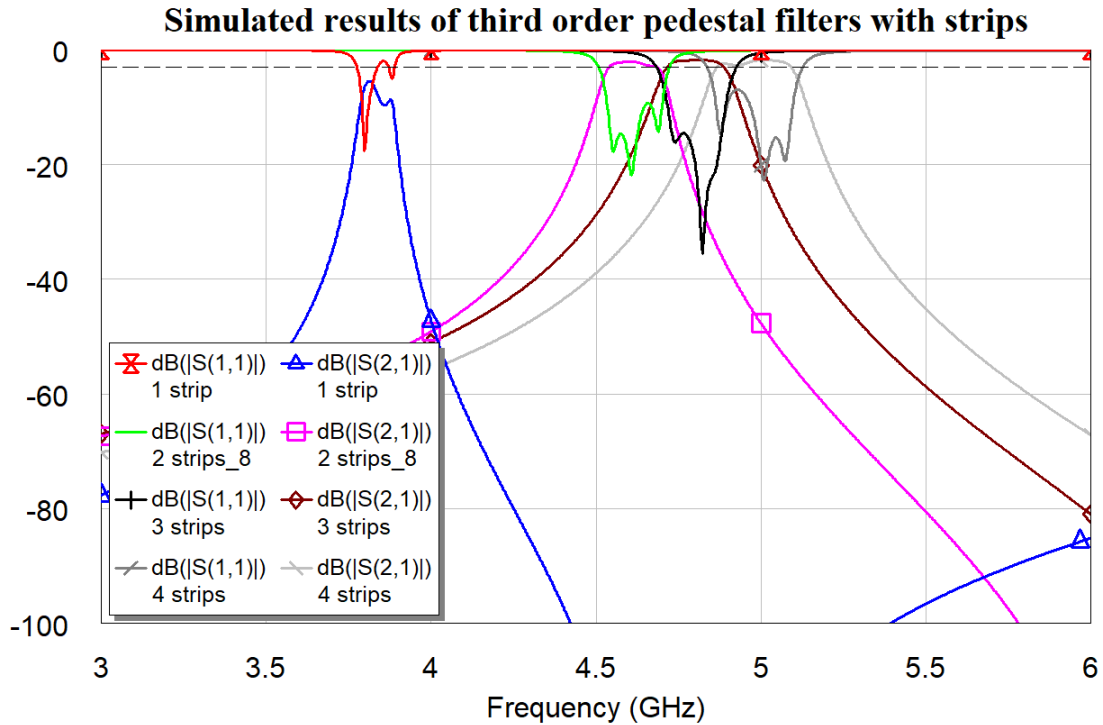


**Figure 5.10:** Simulated results of third order pedestal filters with strips.

The simulated results is summarized in Table 5.4. From Table 5.4 it is clear that the frequency steps are in the same order as for the one resonator case. There are four states resulting in an entire frequency sweep of approximately 1.5 GHz. The filter is designed to operate at 5 GHz with a bandwidth of 5 % with four strips connected, the bandwidth increases as the frequency increases. The return loss is however only less than 10 dB for states 2 to 4. The filter does not function well for state 1.

|         | Simulated       |          |          |
|---------|-----------------|----------|----------|
| State   | $f_0$ (GHz)     | BW (%)   | IL (dB)  |
| State 1 | 3.831           | 2.98     | -5.474   |
| State 2 | 4.622           | 4.65     | -2.14    |
| State 3 | 4.81            | 5.03     | -1.759   |
| State 4 | 5               | 5.76     | -1.756   |

**Table 5.4:** Simulated results for the four different states for the third order filter with strips.

## 5.3.4 Tunable pedestal resonator with PIN diodes

Given the proof of the tunability concept discussed, the strips are replaced with PIN diodes in the next phase to test electronic tunability. A pedestal resonator with PIN diodes is modelled similar to Fig.5.6. The difference is when switching occurs. For the case where a PIN diode is on, it is modelled as an inductor in series with a resistor. However for the case where the PIN diode is off, it is modelled as an inductor in series with a resistor in parallel with a capacitor as shown in Fig. 5.11.
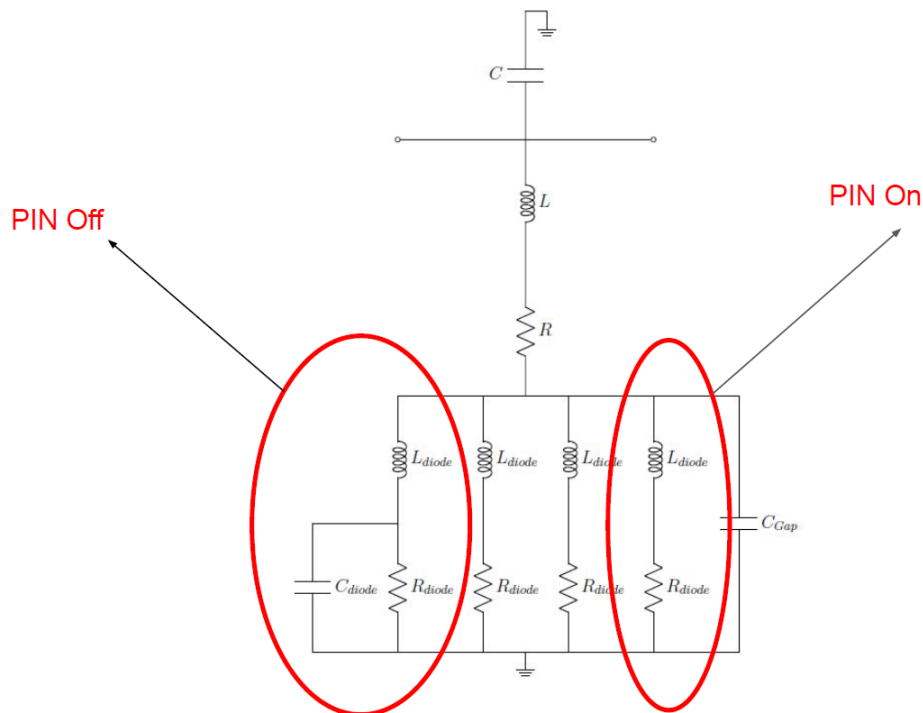


**Figure 5.11:** Circuit model of pedestal resonator with PIN diodes ($R >> Rdiode$).

To limit the effect the resistance of the PIN diodes have on the Q factor of the resonator, a lower resistance PIN diode is chosen. Thus the SMP1320-079LF PIN diode is chosen to be used in this design having a $R_s = 0.75$ $\Omega$ to 2, the $L_s = 0.7$ nH and the $C_T = 0.23$ pF. These values are used in the CST simulations and results in a Q factor of around 160.

To support the PIN diodes a biasing network is needed. A simple biasing network is implemented consisting of etched patches and wires soldered directly to the patches with capacitors connected to ground from each biasing patch, this can be seen in Fig.5.12. A 10 pF capacitor connects each path to ground to ensure no RF signal is let through to the DC power supply, thus separating the RF and DC supplies. The capacitor ensures there is a good connection to ground when the PIN diode is switched on, otherwise the PIN diode will only be connected to a floating patch. In this design a single strip is kept to ensure a good connection to ground at all frequency stages. When there is nothing connected, no PIN diode switched on, or no strip or wire, there is no resonator response seen. Therefore, the need for one connection arises. The simplest way to implement this

connection is with a strip as seen in Fig. 5.12.
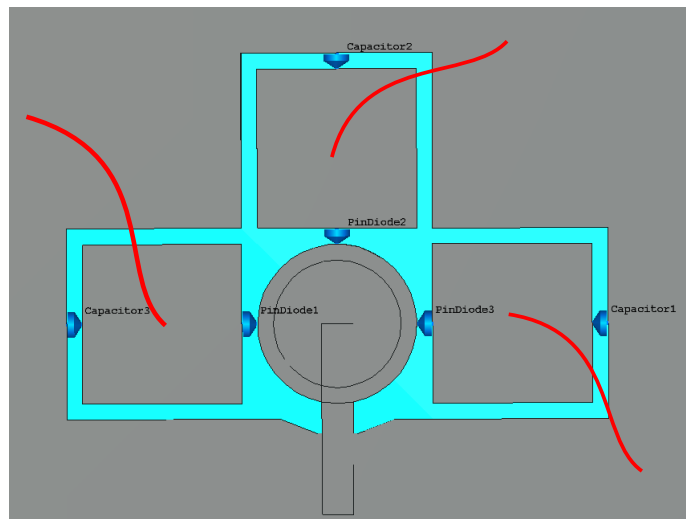


**Figure 5.12:** Biasing network for PIN diodes.

When replacing the etched strips with PIN diodes, a change in the input coupling is needed because of the limited space on the ground layer. The added patches make it more difficult to have an adequate magnetic input coupling because there is no space for a via from the top metal layer to the bottom metal layer. Thus the need for electric coupling arises. The new coupling method can be seen in Fig. 5.13. It consists of a coplanar-line etched in the top layer with a via connected to an annular ring on the same level as the pedestal plate to ensure electric coupling between the pedestal and blind via.
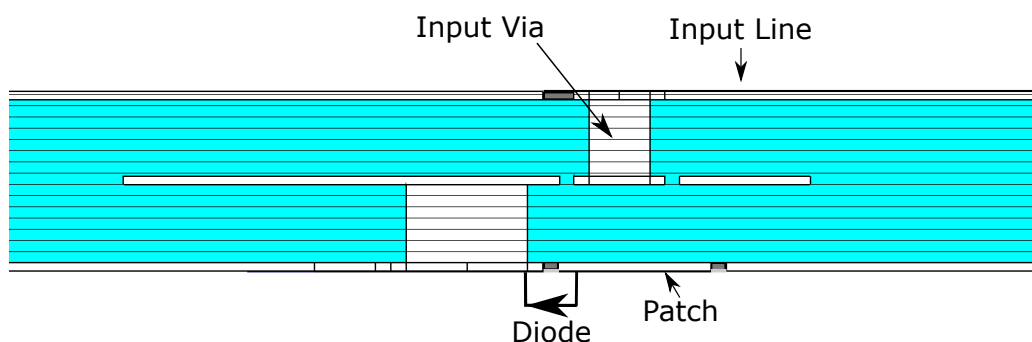


**Figure 5.13:** New input coupling structure.

A parameter study is done to better understand the effects of this biasing network on the frequency response and Q factor of the resonator. For these simulations the CST frequency domain solver with input and output coupling is used because the eigenmode solver does not support lumped elements with non zero resistance values. The input structure used for these simulations can be seen in Fig. 5.13. Three parameters are considered: the etched gap ($Gap$), the patch size ($patchW$) and the strip width ($StripW$). This is shown in Fig. 5.14.
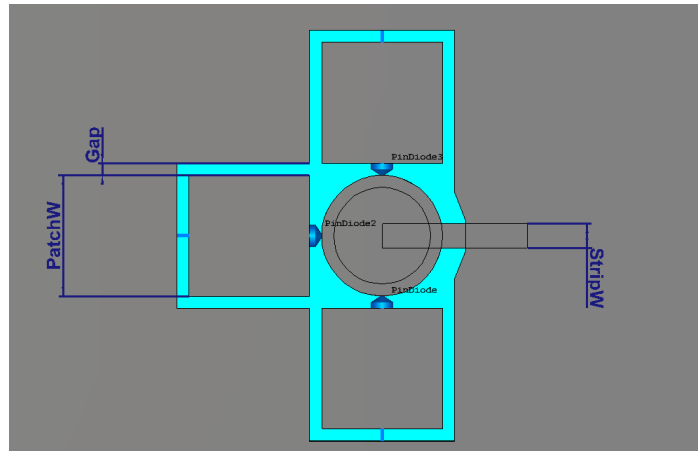
**Figure 5.14:** Bottom view of pedestal resonator with PIN diodes and biasing network.

In the first case the etched gap is considered. For this case the parameters are as follows: $StripW = 0.2$ mm and $patchW = 1$ mm, while $Gap$ is changed from 0.1 mm to 0.2 mm. As expected the $Gap$ parameter has the greatest influence on frequency tuning range. From Table 5.5 it is clear that as the gap increases the frequency tuning range increases, and from Table 5.6 it is clear that the Q factor increases. In the second case the strip width is considered. The strip width changes from 0.1 mm to 0.2 mm while the $Gap = 0.1$ mm and $PatchW = 1$ mm remains constant. The frequency range decreases as the $StripW$ increases, while the Q factor stays more or less constant. In the third case the patch width is considered, $PatchW$ is changed from 0.5 mm to 1 mm while $Gap = 0.1$ mm and $StripW = 1$ mm. As the patch size increases the frequency range decreases and the Q is mostly unaffected.

| Parameter (mm) | State 4 (GHz) | Shift (GHz) | State 3 (GHz) | Shift (GHz) | State 2 (GHz) | shift (GHz) | State 1 (GHz) | Total range (GHz) |
|---|---|---|---|---|---|---|---|---|
| $Gap$ (0.1) | 5 | 0.216 | 4.784 | 0.572 | 4.212 | 0.392 | 3.82 | 1.18 |
| $Gap$ (0.2) | 5 | 0.38 | 4.62 | 0.634 | 3.986 | 0.314 | 3.672 | 1.328 |
| $StripW$ (0.1) | 5 | 0.302 | 4.698 | 0.574 | 4.124 | 0.396 | 3.728 | 1.272 |
| $StripW$ (0.2) | 5 | 0.216 | 4.784 | 0.572 | 4.212 | 0.392 | 3.82 | 1.18 |
| $PatchW$ (0.5) | 5 | 0.216 | 4.784 | 0.572 | 4.212 | 0.392 | 3.82 | 1.18 |
| $PatchW$ (1) | 5 | 0.19 | 4.81 | 0.458 | 4.352 | 0.300 | 4.052 | 0.948 |

**Table 5.5:** Parameter study of tunable pedestal resonator

| Parameter (mm) | $Q_1$ | $Q_2$ | $Q_3$ | $Q_4$ |
|---|---|---|---|---|
| $Gap$ (0.1) | 143 | 137 | 129 | 120 |
| $Gap$ (0.2) | 152 | 144 | 140 | 134 |
| $StripW$ (0.1) | 143 | 138 | 125 | 115 |
| $StripW$ (0.2) | 143 | 137 | 129 | 120 |
| $PatchW$ (0.5) | 143 | 137 | 129 | 120 |
| $PatchW$ (1) | 150 | 137 | 127 | 124 |

**Table 5.6:** Parameter study of tunable pedestal resonator

For the simulated resonator the input length of the input line is set to 2 mm. The rest of the resonator dimensions can be seen in Table 5.7.

| Parameter name | Value (mm) |
|---|---|
| $Gap$ | 0.2 |
| $PatchW$ | 1 |
| $StripW$ | 0.2 |
| $W$ | 4.4 |
| $L$ | 10 |

**Table 5.7:** Pedestal resonator dimensions with PIN diodes.

The simulated results can be seen in Fig. 5.15 and is summarized in Table 5.8.
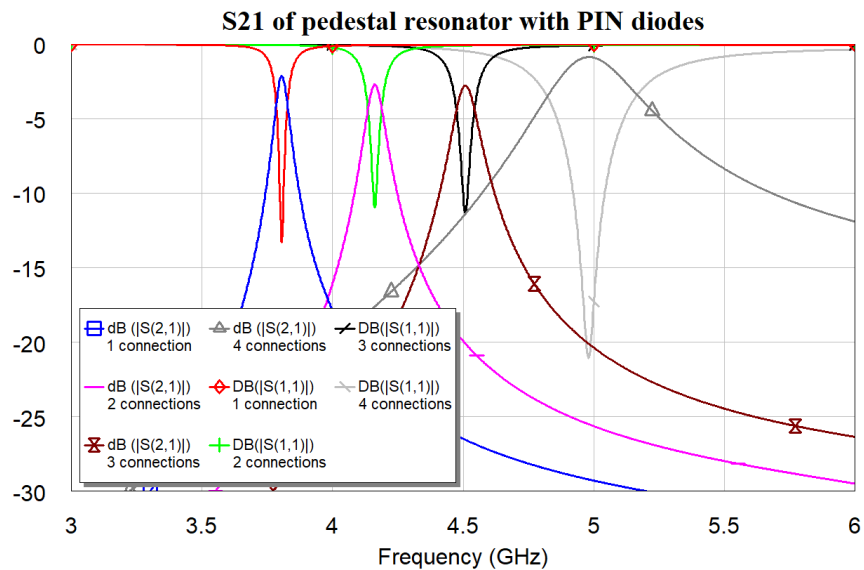


**Figure 5.15:** Simulated results of tunable pedestal resonator with $L = 2$ mm.

| State | Simulated $f_0$ (GHz) | Simulated Q factor |
|-------|-----------------------|--------------------|
| State 1 | 3.805 | 295.94 |
| State 2 | 4.157 | 188.24 |
| State 3 | 4.507 | 159.85 |
| State 4 | 4.987 | 138 |

**Table 5.8:** Simulated results for pedestal resonator with PIN diodes.

The results in Table 5.8 show good frequency shifts with four distinct stages. For the case where the PIN diodes are used the frequency shifts are spaced more equally. From the results the Q factor decreases as the states increase or frequency increases.

## 5.3.5 Third order filter design with PIN diodes

Proof of concept for a switchable SIW pedestal resonator is achieved in the previous section, where it is shown that care should be taken in choosing the components and input line length. With this in mind, a third order tunable pedestal resonator filter with PIN diodes is designed. The filter is designed to operate at 5 GHz with a bandwidth of 5 % at state 4 where all the PIN diodes are connected. The 3D pedestal filter is designed from the circuit model shown in Fig. 5.16 using the group delay method. Starting with the first pedestal resonator with four connections and the input, the group delay was matched accordingly with the circuit model, grounded after the first resonator. Then the second resonator was added and the group delay matched to the circuit model grounded after the second resonator. Lastly the third resonator and output was added.
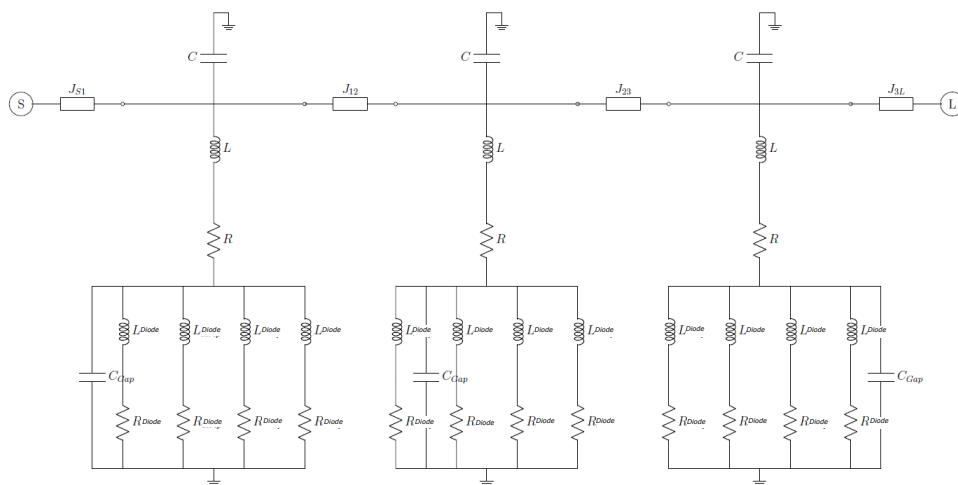


**Figure 5.16:** Circuit model of third order tunable filter with four PIN diodes on.

To ensure that $S_{11}$ and $S_{22}$ is equal to each other and the design is symmetrical, the bottom plate of the filter is designed as in Fig. 5.17 where the direction of the centre strip and biasing network is not in the same direction as for the first and last resonator. There is a 90° difference in orientation.
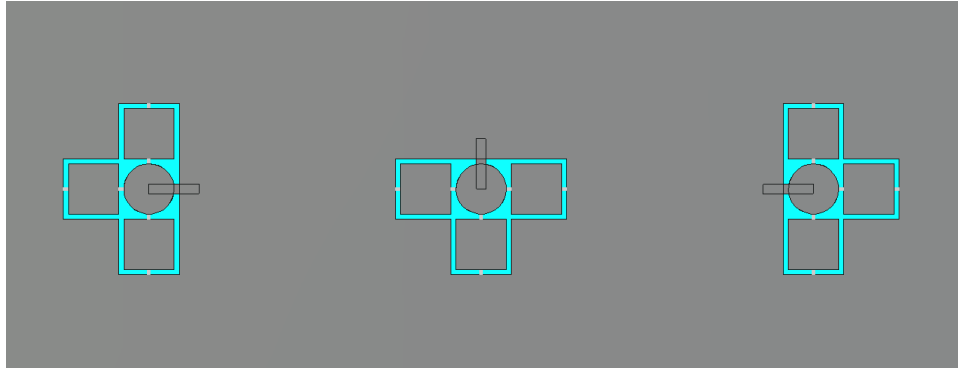
**Figure 5.17:** Bottom view of third order pedestal filter with PIN diodes.

The simulated results can be seen in Fig. 5.18 and the summarized results are shown in Table 5.9. Again a good frequency sweep is seen from 3.878 GHz to 5 GHz, resulting in a total shift of 1.122 GHz. As expected the bandwidths decrease as the frequency decreases. The insertion loss is less than 3 dB over the entire frequency range. The return loss is better than -10 dB over the entire range.
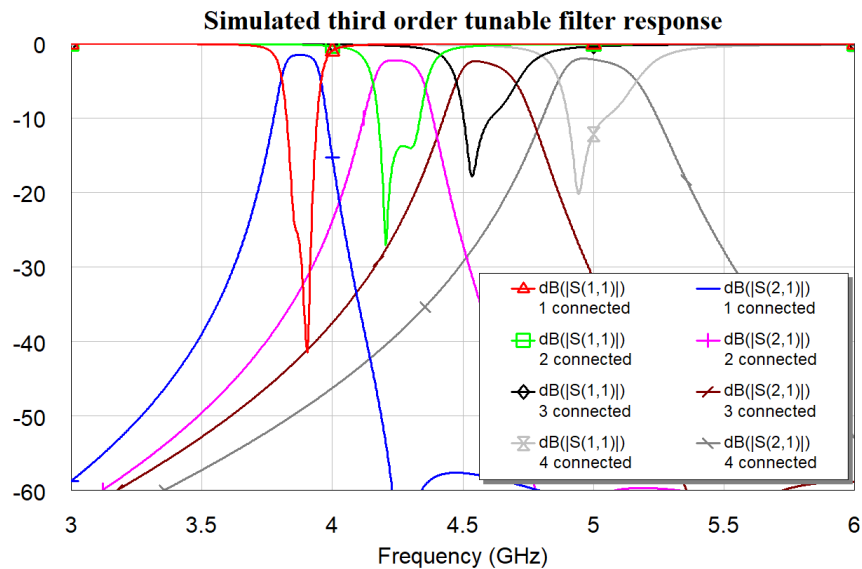


**Figure 5.18:** Simulated frequency response of tunable third order pedestal filter.

|  | Simulated | | |
|---|---|---|---|
| State | $f_0$ (GHz) | BW (%) | IL (dB) |
| State 1 | 3.878 | 3.95 | -1.527 |
| State 2 | 4.249 | 4.83 | -2.25 |
| State 3 | 4.596 | 4.97 | -2.642 |
| State 4 | 5 | 6.24 | -2.285 |

**Table 5.9:** Simulated vs measured results for the four different states for the third order filter with PIN diodes.

## 5.4   Measured results

The pedestal resonator with etched strips and PIN diodes where manufactured and tested along with the corresponding third order filters. The resonators and filters are implemented in a stack-up of two Mercurywave cores ($Er$= 3.5, $thickness$ = 0.508 mm), bonded by a single layer of Mercurywave 1080 prepreg ( $Er$= 3.5, $thickness$ = 0.076 mm). The centre frequencies of the measured results do not match the simulated centre frequencies for all the resonators and filters. This is due to the height of the resonators and filters not being the height that was designed for. The over all height of the resonators and filters are slightly lower causing a slight increase of all the centre frequencies. The measured results show the same frequency shift as the resonators because the circuits where printed on the same slab of dielectric material.

### 5.4.1   Tunable pedestal with etched strips

For the case where etched strips are used a set of four resonators were manufactured, each with a different number of strips, from one to four. The simulated vs measured results can be seen in Table 5.11. A clear frequency shift is seen in the measured results from 4.08 GHz to 5.41 GHz resulting in a total frequency shift of 1.33 GHz. This is slightly more than was simulated for. The simulated frequency range is 1.214 GHz.

| State | Simulated $f_0$ (GHz) | Measured $f_0$ (GHz) | Simulated Q factor | Measured Q factor |
|---|---|---|---|---|
| State 1 | 3.786 | 4.08 | 246 | 53 |
| State 2 | 4.6 | 4.99 | 247 | 76 |
| State 3 | 4.8 | 5.24 | 246 | 90 |
| State 4 | 5 | 5.41 | 234 | 106 |

**Table 5.10:** Simulated vs measured results for the four different states.

From Table 5.11 it is clear that the measured Q factors are much lower than the simulated Q factors. This may be due to surface roughness not being taken into account in the simulations. However, further investigation is needed to conclude where the added losses comes from.

Four individual filters were manufactured, each with a different number of strips, from one to four. Each resonator has the same number and configuration for each individual filter. A 3D model of the filter can be seen in Fig. 5.19(a) and the fabricated filters can be seen in Fig. 5.19(b). The simulated vs measured results are summarized in Table 5.11.

**(a)** 3D view of third order pedestal filter with strips.

**(b)** Photo of four pedestal third order filters with strips.
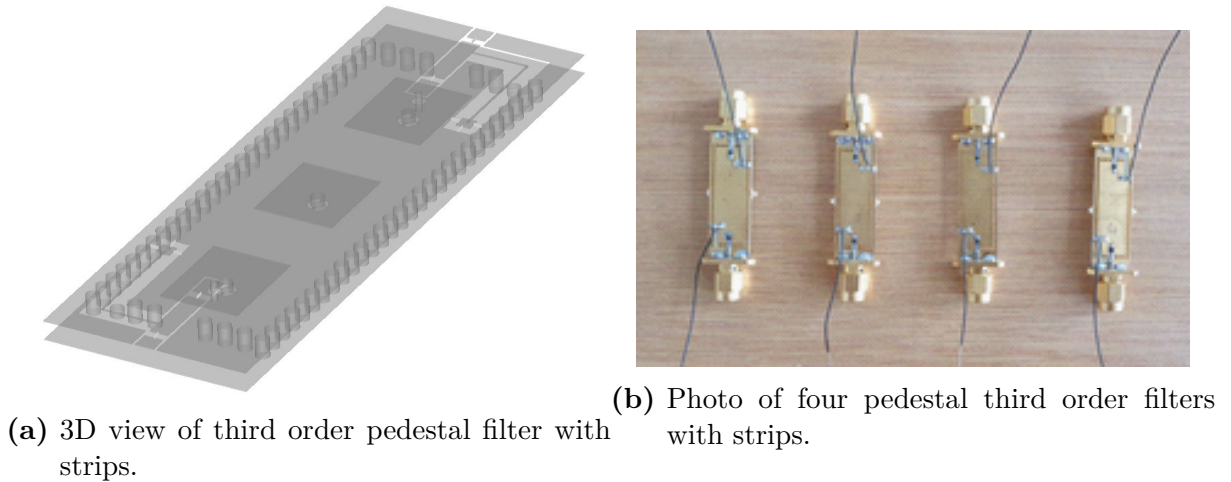
**Figure 5.19:** 3D view and photo of four pedestal third order filters with strips.

| State | Simulated | | | Measured | | |
|---|---|---|---|---|---|---|
| | $f_0$ (GHz) | BW (%) | IL (dB) | $f_0$ (GHz) | BW (%) | IL (dB) |
| State 1 | 3.831 | 2.98 | -5.474 | 4.094 | 3.47 | -16.58 |
| State 2 | 4.622 | 4.65 | -2.14 | 5 | 6.14 | -7.042 |
| State 3 | 4.81 | 5.03 | -1.759 | 5.2 | 6.2 | -5.72 |
| State 4 | 5 | 5.76 | -1.756 | 5.38 | 6.9 | -4.814 |

**Table 5.11:** Simulated vs measured results for the four different states for the third order filter with strips.

The return loss is less than 10 dB for states 2, 3 and 4 for the measured results. For state 1 the return loss and insertion loss is the poorest as expected from the simulated results. This is mostly due to an inadequate matching at the input. The manufactured insertion loss of all the states is again significantly higher than predicted. Because of manufacturing error in the height of the substrates the centre frequency of the filters is shifted up by 0.76 GHz. From the results it is clear that there is much more insertion loss in the manufactured filters than expected. It is still unclear where the added losses comes from. Further investigation is needed to determine where the added losses comes from. Due to time constraints it was decided that this investigation will not form part of the work for this dissertation.

## 5.4.2   Tunable pedestal with PIN diodes

As mentioned the next step was to replace the etched strips with PIN diodes. A resonator and third order filter was manufactured and tested. The simulated and measured results can be seen in Table 5.12.

| State | Simulated $f_0$ (GHz) | Measured $f_0$ (GHz) | Simulated Q factor | Measured Q factor |
|-------|------------------------|----------------------|---------------------|-------------------|
| State 1 | 4.987 | 5.269 | 138 | 30.89 |
| State 2 | 4.507 | 4.616 | 159.85 | 23.882 |
| State 3 | 4.157 | 4.122 | 188.24 | 26.146 |
| State 4 | 3.805 | 3.569 | 295.94 | 21.16 |

**Table 5.12:** Simulated and measured results for pedestal resonator with PIN diodes.

The measured resonator obtained a frequency shift from 3.569 GHz to 5.269 GHz, resulting in a total frequency shift of 1.7 GHz. These results are shifted in frequency due to the height of the substrate not being exactly what was designed for. The height is approximately 0.15 mm higher in the top layer of the substrate resulting in a frequency shift of approximately 0.25 GHz.

The measured Q factors of the resonators are however much lower than expected. The simulated unloaded Q factor for a tunable pedestal resonator with three PIN diodes connected and one strip connection is around 138. However, the measured unloaded Q factor is 30.89. One of the reasons for this is that the simulated unloaded Q factor is done with no surface roughness accounted for. When this is included in the simulation by lowering the conductivity of copper to 4e-7 S/m the Q factor decreases to 85. This still does not explain the much lower Q factor seen in the measurements. An extraction was done on the capacitors used for the biasing networks of the PIN diodes and it was found that the resistance of the capacitors was 5 Ω, much higher than the 0.2 Ω indicated on the data-sheet. When the resistance of the capacitor in the simulation is changed to 5 Ω the unloaded Q factor is 32. This problem was addressed by replacing the capactors with high Q capacitors, however the measured results did not show an increase in Q factor. Thus the capacitors is not the reason for the much lower Q factors. It is still unclear where the added losses comes from. Further investigation is needed to determine where the added losses comes from. Due to time constraints it was decided that this investigation will not form part of the work for this dissertation.

It is however important to note that it is not possible to obtain the exact same frequency range with a varactor diode. The maximum range that is obtained with a varactor diode is from 3.88 GHz to 5.196 GHz, resulting in a maximum range of 1.316 GHz, 0.37 GHz less than for when PIN diodes that are used. A varactor diode with a varying capacitance from 0.2 pF to 2 pF is needed to achieve this maximum range. This results in using a varactor diode with a series resistance of approximately 4.8 Ω. The simulated unloaded Q factor for a resonator with a single varactor diode with series resistance of 4.8 Ω is 7.3. This is still much lower than the case for the simulated PIN diodes. Thus using a switched scheme for frequency tunability with PIN diodes is better than continuous tuning with varactor diodes for the pedestal SIW resonator.

The measured results for the third order filter show the same frequency shift as the resonators because the circuits where printed on the same slab of dielectric material. The measured versus simulated results can be seen in Table 5.13. As expected the bandwidths decrease as the frequency decreases. The IL is also much lower in the case of the measured results, it is still unclear where the added losses comes from. Further investigation is

needed to determine where the added losses comes from. Due to time constraints it was decided that this investigation will not form part of the work for this dissertation.

| State | Simulated | | | Measured | | |
|---|---|---|---|---|---|---|
| | $f_0$ (GHz) | BW (%) | IL (dB) | $f_0$ (GHz) | BW (%) | IL (dB) |
| State 1 | 3.878 | 3.95 | -1.527 | 3.714 | 4.3 | -15.35 |
| State 2 | 4.249 | 4.83 | -2.25 | 4.152 | 4.4 | -15.17 |
| State 3 | 4.596 | 4.97 | -2.642 | 4.95 | 5.05 | -11.38 |
| State 4 | 5 | 6.24 | -2.285 | 5.253 | 5.86 | -8.832 |

**Table 5.13:** Simulated vs measured results for the four different states for the third order filter with PIN diodes.

## 5.5   Conclusion

In this chapter tunability of the pedestal resonator is investigated. Multiple resonators and low order filters are designed simulated, manufactured and measured. The simulated and measured results validates the design technique developed to achieve frequency tunalility. The results show four distinct frequency shift resulting in a total frequency range of approximately 1.7 GHZ for the resonators and 1.705 GHz for the third order filters. The measured unloaded Q factor is not as expected. This problem is observed but no further investigation is done due to time constraints of the project.

To achieve the same frequency shift with varactor diodes the unloaded Q factor is reduced to 7.3 that is lower than the case for the use of PIN diodes. Thus, it is proven that the use of a switchable scheme with PIN diodes to obtain tunability is better suited than continuous tuning with varactor diodes.

# Chapter 6

# Conclusion

When designing microwave filters a designers choice can be influenced by a number of different factors. When size and Q factor are the main factors to be looked at, the pedestal resonator is a good option to have. The pedestal resonator offers a good compromise between high Q factors and small size. The pedestal resonator especially the partially air-filled pedestal resonator gives the designer the ability to have more control over the Q factor as the total volume size is chosen for a certain frequency.

In this dissertation, the pedestal resonator is investigated and applied in three different ways. The first concept it is used for is to develop a filter with both positive and negative coupling in one structure. A proof- of-concept sixth order cross-coupled SIW bandpass filter is presented. Both positive and negative cross-coupling are found in this design using the pedestal resonator. The measured results are in good agreement with the simulation and theory. Transmission zeros at real frequencies are realized through the use of both positive and negative cross-coupling, as well as group delay equalization. It is found that the SIW pedestal resonator lends itself well to the implementation of both positive and negative cross-coupling.

The second application of the SIW pedestal resonator is in the designing of a novel partially air-filled pedestal resonator. This is done to increase the Q factor of relatively small sized cavities. A wide range of Q factors can be obtained with the partially air-filled pedestal resonator. Q factors from 240 to 1860 is achieved with simulation for the same frequency. Utilizing micro-machining a structure like the partially air-filled pedestal is possible. Making it possible to increase the Q factor while maintaining a small size. The manufacturing process resulted in good resonators and filters operating with higher Q factors in comparison to resonators and filters manufactured with dielectric material. The Q factor was increased with 34%. It is further shown that the Q factor can be increased by changing the distance between the top metal wall and the metal pedestal.

The last application of the SIW pedestal resonator is for the use of tunable resonators and filters. The SIW pedestal resonator is shown to be made tunable with the implementation of PIN diodes to the bottom of the pedestal post. The results show four distinct frequency shift resulting in a total frequency shift of approximately 1.7 GHz for the resonators and 1.6 GHz for the third order filter. The unloaded Q factors are however much lower than expected.Further investigation is needed to determine where the added losses comes from. Due to time constraints it was decided that this investigation will not form part of the work for this dissertation. It is shown theoretically that the use of PIN diodes

for tunability is better than using varactor diodes where the Q factor is concerned.

From the work done it is clear that the SIW pedestal resonator hold many benefits for the use of microwave filters. The SIW pedestal resonator can however be used for other components such as filtennas.

# Bibliography

[1]  R. K. Hoffmann and H. Howe, "Handbook of microwave integrated circuits," 1987.

[2]  E. Notes. (2020) Understanding varactor diode specifications: specs and parameters. [Online]. Available: https://www.electronics-notes.com/articles/electronic_components/diode/varactor-varicap-diode-specifications.php

[3]  E. Meyer, "Tunable narrow-band x-band bandpass filters," Ph.D. dissertation, 2018.

[4]  D. Deslandes and Ke Wu, "Single-substrate integration technique of planar circuits and waveguide filters," *IEEE Transactions on Microwave Theory and Techniques*, vol. 51, no. 2, pp. 593–596, 2003.

[5]  K. Entesari, A. P. Saghati, V. Sekar, and M. Armendariz, "Tunable siw structures: Antennas, vcos, and filters," *IEEE Microwave Magazine*, vol. 16, no. 5, pp. 34–54, 2015.

[6]  D. Deslandes and K. Wu, "Integrated microstrip and rectangular waveguide in planar form," *IEEE Microwave and Wireless Components Letters*, vol. 11, no. 2, pp. 68–70, 2001.

[7]  K. Wu, D. Deslandes, and Y. Cassivi, "The substrate integrated circuits - a new concept for high-frequency electronics and optoelectronics," in *6th International Conference on Telecommunications in Modern Satellite, Cable and Broadcasting Service, 2003. TELSIKS 2003.*, vol. 1, 2003, pp. P–III.

[8]  S. Sirci, F. Gentili, J. D. Martinez, V. E. Boria, and R. Sorrentino, "Quasi-elliptic filter based on SIW combline resonators using a coplanar line cross-coupling," *2015 IEEE MTT-S International Microwave Symposium, IMS 2015*, pp. 2–5, 2015.

[9]  H. Wang and Q. X. Chu, "An inline coaxial quasi-elliptic filter with controllable mixed electric and magnetic coupling," *IEEE Transactions on Microwave Theory and Techniques*, vol. 57, no. 3, pp. 667–673, 2009.

[10]  G. Lojewski and N. Militaru, "Design of Microwave Band-Pass Filters with Cross-Couplings based on Electromagnetic Simulation and Linear Circuit Optimization," no. 1, pp. 49–53, 2008.

[11]  N. Ranjkesh and M. Shahabadi, "Reduction of dielectric losses in substrate integrated waveguide," *Electronics Letters*, vol. 42, pp. 1230 – 1231, 11 2006.

[12]  N. Nguyen, A. Ghiotto, T. Vuong, A. Vilcot, T. Martin, and K. Wu, "Dielectric slab air-filled substrate integrated waveguide (safsiw) bandpass filters," *IEEE Microwave and Wireless Components Letters*, vol. 30, no. 4, pp. 363–366, 2020.

[13] S. Moscato, C. Tomassoni, M. Bozzi, and L. Perregrini, "Quarter-mode cavity filters in substrate integrated waveguide technology," *IEEE Transactions on Microwave Theory and Techniques*, vol. 64, no. 8, pp. 2538–2547, 2016.

[14] L. Silvestri, A. Ghiotto, C. Tomassoni, M. Boziz, and L. Perregrini, "Partially air-filled substrate integrated waveguide filters with full control of transmission zeros," *IEEE Transactions on Microwave Theory and Techniques*, vol. 67, no. 9, pp. 3673–3682, 2019.

[15] F. Parment, A. Ghiotto, T. Vuong, J. Duchamp, and K. Wu, "Broadband transition from dielectric-filled to air-filled substrate integrated waveguide for low loss and high power handling millimeter-wave substrate integrated circuits," in *2014 IEEE MTT-S International Microwave Symposium (IMS2014)*, 2014, pp. 1–3.

[16] S. Hao and Q. J. Gu, "A fourth order tunable capacitor coupled microstrip resonator band pass filter," in *2015 IEEE Radio and Wireless Symposium (RWS)*, 2015, pp. 150–152.

[17] W. Tang and J.-S. Hong, "Tunable microstrip quasi-elliptic function bandpass filters," in *2009 European Microwave Conference (EuMC)*, 2009, pp. 767–770.

[18] P. Meyer and S. Nassar, "Pedestal substrate integrated waveguide resonators and filters," *IET Microwaves, Antennas & Propagation*, pp. 1–8, 2017.

[19] L. Johnson, P. Meyer, and E. Meyer, "Pedestal substrate integrated waveguide filter with both electric and magnetic cross-couplings," *SAIEE Africa Research Journal*, vol. 111, no. 1, pp. 36–43, 2020.

[20] R. J. Cameron, C. M. Kudsia, and R. R. Mansour, *Microwave Resonators*, 2018, pp. 373–394.

[21] D. Pozar, *Microwave Engineering, 4th Edition*. Wiley, 2011. [Online]. Available: https://books.google.fr/books?id=JegbAAAAQBAJ

[22] H. V. Manjunatha Reddy, "Design and simulation of L-band coaxial ceramic resonator oscillator," *2016 IEEE Annual India Conference, INDICON 2016*, 2017.

[23] M. Hoft and F. Yousif, "Orthogonal coaxial cavity filters with distributed cross-coupling," *IEEE Microwave and Wireless Components Letters*, vol. 21, no. 10, pp. 519–521, 2011.

[24] F. van Raay, R. Quay, R. Kiefer, W. Bronner, M. Seelmann-Eggebert, M. Schlechtweg, M. Mikulla, and G. Weimann, "X-band high-power microstrip algan/gan hemt amplifier mmics," in *2006 IEEE MTT-S International Microwave Symposium Digest*, 2006, pp. 1368–1371.

[25] S. Maas, "Coaxial resonator filters," Master's thesis, Stellenbosch University. Faculty of Engineering. Dept. of Electrical and Electronic Engineering., http://hdl.handle.net/10019.1/18067, 12 2011, an optional note.

[26] Cheng-Cheh Yu and Kai Chang, "Transmission-line analysis of a capacitively coupled microstrip-ring resonator," *IEEE Transactions on Microwave Theory and Techniques*, vol. 45, no. 11, pp. 2018–2024, 1997.

[27] Zhang Xiangjun, Ma Xiaoping, and Lai Qifeng, "Compact multilayer coupled stripline ltcc filter with defected ground structure," in *2009 International Conference on Microwave Technology and Computational Electromagnetics (ICMTCE 2009)*, 2009, pp. 204–206.

[28] E. Rammos, "A new wideband, high gain suspended substrate line planar array for 12 ghz satellite t.v." in *1983 13th European Microwave Conference*, 1983, pp. 227–231.

[29] S. D. Mallanna and K. Viswanath, "Performance analysis of resonators for microwave applications," in *2018 International Conference on Electrical, Electronics, Communication, Computer, and Optimization Techniques (ICEECCOT)*, 2018, pp. 741–745.

[30] S. Malik, C. Sharma, M. Varshney, and S. Pandey, "Effect of substrate on s-parameters of microstrip ring resonator," in *2018 Second International Conference on Intelligent Computing and Control Systems (ICICCS)*, 2018, pp. 1239–1243.

[31] I. Wolff and N. Knoppik, "Microstrip ring resonator and dispersion measurement on microstrip lines," *Electronics Letters*, vol. 7, pp. 779–781, 1971.

[32] M. Schoeman, "Interpolation-based modelling of microwave ring resonators," Ph.D. dissertation, Stellenbosch University. Faculty of Engineering. Dept. of Electrical and Electronic Engineering., The address of the publisher, 12 2006, an optional note.

[33] A. Rhbanou, S. Bri, and M. Sabbane, "Analysis of Substrate Integrated Waveguide (SIW) Resonator and Design of Miniaturized SIW Bandpass Filter," *International Journal of Electronics and Telecommunications*, vol. 63, no. 3, pp. 255–260, 2017.

[34] X. Li, C. K. C. Tzuang, and H. S. Wu, "Dispersion characteristic a periodic substrate integrated waveguide of parallel metallic plates," *2014 International Conference on Numerical Electromagnetic Modeling and Optimization for RF, Microwave, and Terahertz Applications, NEMO 2014*, pp. 1–4, 2014.

[35] X. C. Zhu, W. Hong, K. Wu, K. D. Wang, L. S. Li, Z. C. Hao, H. J. Tang, and J. X. Chen, "Accurate characterization of attenuation constants of substrate integrated waveguide using resonator method," *IEEE Microwave and Wireless Components Letters*, vol. 23, no. 12, pp. 677–679, 2013.

[36] A. Atia, A. Williams, and R. Newcomb, "Narrow-band multiple-coupled cavity synthesis," *IEEE Transactions on Circuits and Systems*, vol. 21, no. 5, pp. 649–655, 1974.

[37] X. P. Chen and K. Wu, "Substrate integrated waveguide cross-coupled filter with negative coupling structure," *IEEE Transactions on Microwave Theory and Techniques*, vol. 56, no. 1, pp. 142–149, 2008.

[38] C. Tomassoni, L. Silvestri, M. Bozzi, and L. Perregrini, "Novel substrate integrated waveguide filter based on mushroom resonators," in *2015 IEEE 15th Mediterranean Microwave Symposium (MMS)*, 2015, pp. 1–4.

[39] ——, "Quasi-elliptic siw band-pass filter based on mushroom-shaped resonators," in *2015 European Microwave Conference (EuMC)*, 2015, pp. 749–752.

[40] C. Tomassoni and R. Sorrentino, "A new class of pseudo-elliptic waveguide filters using resonant posts," in *2012 IEEE/MTT-S International Microwave Symposium Digest*, 2012, pp. 1–3.

[41] M. Dong, D. Shen, C. Ma, and X. Zhang, "A cascaded six order bandpass siw filter using electric and magnetic couplings technology," in *2017 Sixth Asia-Pacific Conference on Antennas and Propagation (APCAP)*, 2017, pp. 1–3.

[42] D. Jia, Q. Feng, Q. Xiang, and K. Wu, "Multilayer Substrate Integrated Waveguide (SIW) Filters with Higher-Order Mode Suppression," *IEEE Microwave and Wireless Components Letters*, vol. 26, no. 9, pp. 678–680, 2016.

[43] L. S. Wu, X. L. Zhou, and W. Y. Yin, "A novel multilayer partial h-plane filter implemented with folded substrate integrated waveguide (FSIW)," *IEEE Microwave and Wireless Components Letters*, vol. 19, no. 8, pp. 494–496, 2009.

[44] C. Wang and K. A. Zaki, "Full-wave modeling of electric coupling probes in comb-line resonators and filters," *IEEE Transactions on Microwave Theory and Techniques*, vol. 48, no. 12, pp. 2459–2464, 2000.

[45] B. Potelon, J. F. Favennec, C. Quendo, E. Rius, C. Person, and J. C. Bohorquez, "Design of a Substrate Integrated Waveguide (SIW) filter using a novel topology of coupling," *IEEE Microwave and Wireless Components Letters*, vol. 18, no. 9, pp. 596–598, 2008.

[46] K. Gong, W. Hong, Y. Zhang, P. Chen, and C. J. You, "Substrate integrated waveguide quasi-elliptic filters with controllable electric and magnetic mixed coupling," *IEEE Transactions on Microwave Theory and Techniques*, vol. 60, no. 10, pp. 3071–3078, 2012.

[47] B. Koh, B. Lee, S. Nam, T. H. Lee, and J. Lee, "Integration of Interresonator Coupling Structures with Applications to Filter Systems with Signal Route Selectivity," *IEEE Transactions on Microwave Theory and Techniques*, vol. 64, no. 9, pp. 2790–2803, 2016.

[48] S. Sirci, M. A. Sánchez-Soriano, J. D. Martinez, V. E. Boria, F. Gentili, W. Bosch, and R. Sorrentino, "Design and multiphysics analysis of direct and cross-coupled siw combline filters using electric and magnetic couplings," *IEEE Transactions on Microwave Theory and Techniques*, vol. 63, no. 12, pp. 4341–4354, 2015.

[49] R. J. Cameron, "General coupling matrix synthesis methods for Chebyshev filtering functions," *IEEE Transactions on Microwave Theory and Techniques*, vol. 47, no. 4, pp. 433–442, 1999.

[50] R. Cameron, R. Mansour, and C. Kudsia, *Microwave Filters for Communication Systems: Fundamentals, Design and Applications.* Wiley, 2007. [Online]. Available: https://books.google.fr/books?id=GyVTAAAAMAAJ

[51] N. Nguyen, A. Ghiotto, T. Vuong, A. Vilcot, F. Parment, and K. Wu, "Slab air-filled substrate integrated waveguide," in *2018 IEEE/MTT-S International Microwave Symposium - IMS*, 2018, pp. 312–315.

[52] N. Nguyen, A. Ghiotto, T. Martin, A. Vilcot, K. Wu, and T. Vuong, "A 90° self-compensating slab air-filled substrate integrated waveguide phase shifter," in *2019 IEEE MTT-S International Microwave Symposium (IMS)*, 2019, pp. 580–583.

[53] E. Massoni, M. Bozzi, and K. Wu, "Increasing efficiency of leaky-wave antenna by using substrate integrated slab waveguide," *IEEE Antennas and Wireless Propagation Letters*, vol. 18, no. 8, pp. 1596–1600, 2019.

[54] A. Belenguer, H. Esteban, and V. E. Boria, "Novel empty substrate integrated waveguide for high-performance microwave integrated circuits," *IEEE Transactions on Microwave Theory and Techniques*, vol. 62, no. 4, pp. 832–839, 2014.

[55] F. Parment, A. Ghiotto, T. Vuong, J. Duchamp, and K. Wu, "Air-filled substrate integrated waveguide for low-loss and high power-handling millimeter-wave substrate integrated circuits," *IEEE Transactions on Microwave Theory and Techniques*, vol. 63, no. 4, pp. 1228–1238, 2015.

[56] N. H. Nguyen, F. Parment, A. Ghiotto, K. Wu, and T. P. Vuong, "A fifth-order air-filled siw filter for future 5g applications," in *2017 IEEE MTT-S International Microwave Workshop Series on Advanced Materials and Processes for RF and THz Applications (IMWS-AMP)*, 2017, pp. 1–3.

[57] T. Martin, A. Ghiotto, F. Lotz, and T. Vuong, "Air-filled siw filters for k- to e-band substrate integrated systems," in *2018 IEEE MTT-S International Conference on Numerical Electromagnetic and Multiphysics Modeling and Optimization (NEMO)*, 2018, pp. 1–3.

[58] D. Shishido and M. Tamura, "Development of an air-filled siw filter with wideband spurious suppression," in *2020 IEEE International Symposium on Radio-Frequency Integration Technology (RFIT)*, 2020, pp. 13–15.

[59] J. R. Sánchez, C. Bachiller, M. Juliá, V. Nova, H. Esteban, and V. E. Boria, "Microwave filter based on substrate integrated waveguide with alternating dielectric line sections," *IEEE Microwave and Wireless Components Letters*, vol. 28, no. 11, pp. 990–992, 2018.

[60] C. Tomassoni, L. Silvestri, A. Ghiotto, M. Bozzi, and L. Perregrini, "Substrate-integrated waveguide filters based on dual-mode air-filled resonant cavities," *IEEE Transactions on Microwave Theory and Techniques*, vol. 66, no. 2, pp. 726–736, 2018.

[61] C. Tomassoni, L. Silvestri, M. Bozzi, L. Perregrini, and A. Ghiotto, "A novel filter based on a dual-mode air-filled substrate integrated waveguide cavity resonator," in *2017 IEEE MTT-S International Conference on Numerical Electromagnetic and Multiphysics Modeling and Optimization for RF, Microwave, and Terahertz Applications (NEMO)*, 2017, pp. 290–292.

[62] S. Adhikari, Y. Ban, and K. Wu, "Magnetically tunable ferrite loaded substrate integrated waveguide cavity resonator," *IEEE Microwave and Wireless Components Letters*, vol. 21, no. 3, pp. 139–141, 2011.

[63] S. Adhikari, A. Ghiotto, and K. Wu, "Simultaneous electric and magnetic two-dimensional tuning of substrate integrated waveguide cavity resonator," in *2012 IEEE/MTT-S International Microwave Symposium Digest*, 2012, pp. 1–3.

[64] S. Sirci, J. D. Martínez, M. Taroncher, and V. E. Boria, "Varactor-loaded continuously tunable siw resonator for reconfigurable filter design," in *2011 41st European Microwave Conference*, 2011, pp. 436–439.

[65] F. Mira, J. Mateu, and C. Collado, "Mechanical tuning of substrate integrated waveguide resonators," *IEEE Microwave and Wireless Components Letters*, vol. 22, no. 9, pp. 447–449, 2012.

[66] F. Giuppi, A. Georgiadis, A. Collado, M. Bozzi, and L. Perregrini, "Tunable siw cavity backed active antenna oscillator," *Electronics Letters*, vol. 46, no. 15, pp. 1053–1055, 2010.

[67] A. Anand, J. Small, D. Peroulis, and X. Liu, "Theory and design of octave tunable filters with lumped tuning elements," *IEEE Transactions on Microwave Theory and Techniques*, vol. 61, no. 12, pp. 4353–4364, 2013.

[68] V. Sekar, M. Armendariz, and K. Entesari, "A 1.2–1.6-ghz substrate-integrated-waveguide rf mems tunable filter," *IEEE Transactions on Microwave Theory and Techniques*, vol. 59, no. 4, pp. 866–876, 2011.

[69] A. El Mostrah, A. Muller, J. F. Favennec, B. Potelon, A. Manchec, E. Rius, C. Quendo, Y. Clavet, F. Doukhan, and J. Le Nezet, "An RF-MEMS-based digitally tunable SIW filter in X-band for communication satellite applications," *Applied Sciences (Switzerland)*, vol. 9, no. 9, 2019.

[70] V. Sekar and K. Entesari, "A half-mode substrate-integrated-waveguide tunable filter using packaged rf mems switches," *IEEE Microwave and Wireless Components Letters*, vol. 22, no. 7, pp. 336–338, 2012.

[71] T. R. Jones and M. Daneshmand, "Miniaturized folded ridged quarter-mode substrate integrated waveguide rf mems tunable bandpass filter," *IEEE Access*, vol. 8, pp. 115 837–115 847, 2020.

[72] J. C. Bohorquez, B. Potelon, C. Person, E. Rius, C. Quendo, G. Tanne, and E. Fourn, "Reconfigurable planar siw cavity resonator and filter," in *2006 IEEE MTT-S International Microwave Symposium Digest*, 2006, pp. 947–950.

[73] M. Armendariz, V. Sekar, and K. Entesari, "Tunable siw bandpass filters with pin diodes," in *The 40th European Microwave Conference*, 2010, pp. 830–833.

[74] S. Sirci, J. Martinez, and V. Boria, "Low-loss 3-bit tunable SIW filter with PIN diodes and integrated bias network," *Proceedings of the 43rd European Microwave Conference*, pp. 1211–1214, 2013.